UiT The Arctic University of Norway

Faculty of Science and Technology
Department of Geosciences

Marine- and Lacustrine Deposition of Eskers

Esker morphology from water-terminating margins of the Eurasian Ice Sheet Complex

Teitur Hinrichsen

Master's thesis in Marine Geology and Geophysics GEO-3900 May 2024

“The name "esker" is that by which one kind is familiarly
known in this country; and it seems allowable that
that which has been applied to the other should be,
on the present occasion, appropriate thereto.”
–Rev. Maxwell H. Close, 1866

Abstract

The future stability of modern marine-terminating ice sheets is of great concern as an increased rate of retreat might mark the onset of their collapse. An increased rate of retreat is accompanied by an increase in meltwater and sediment discharge at the ice margin which has prompted research to focus on the drainage system of marine-terminating ice sheets. Recent discoveries of eskers at water-terminating margins of the Eurasian Ice Sheet Complex provide a premise for the study of the palaeo-drainage system during the retreat of the ice margin following the Last Glacial Maximum. This study explores two areas that were covered by water-terminating sectors of the Eurasian Ice Sheet Complex, Hopendjupet in the Barents Sea and Hoburgs Bank in the Baltic Sea, both of which exhibit palaeo-drainage landforms, tunnel valleys, and eskers. A special focus is placed on the study of eskers as they have rarely been described from marine-terminating ice sheets.

A new approach to mapping eskers on digital elevation models is presented that allows for a more detailed morphological analysis and statistical description than the traditional method of mapping eskers with lines. The new approach to mapping eskers uses polygons to map the extent of the landforms and a program written in Python is used to extract the length, height, width, and sinuosity of eskers as well as height and width changes along their length. Between Hopendjupet and Hoburgs Bank, a variety of esker types are found (beaded eskers, esker enlargements, esker corridors, complex eskers, and till eskers) representing esker deposition in subglacial and deltaic settings, time-transgressive and synchronous esker formation, and deposition in en- and subglacial channels. Eskers in Hopendjupet exclusively occur in connection to erosional Nye-channels suggestive of a generally erosive drainage system. Till eskers and crevasse-fill ridges on Hoburgs Bank form a geometric and sinuous ridge network that potentially represents the hydro-fracturing of a cold-based polythermal ice margin.

Acknowledgements

This thesis represents more than just a one-year research project but is the collection of years of studying. I would like to thank Professor Emeritus Ólafur Ingólfsson and Dr Ívar Örn Benediktsson, both at the University of Iceland, who planted the idea in my head to move to Tromsø to pursue the study of marine geology. Thanks go out to my co-workers at Landsvirkjun, The National Power Company of Iceland, Alma Stefánsdóttir, Ásgerður Sigurðardóttir, Dr Helgi Arnar Alfreðsson and Hulda Kristín Helgadóttir, who have all contributed to my professional experience in the field of geology for the past three summers. To my family, Arnór Tumi Jóhannsson, Helmut Helgi Hinrichsen, and Dr Jóhanna Arnórsdóttir, who have supported me in so many ways, financially and academically, over the past couple of years and who have contributed directly to this thesis by profreading the text, I am immensely grateful for your support.

To my team of supervisors, Associate Professor Monica Winsborrow and Dr Henry Patton at UiT The Arctic University of Norway and Dr Sarah Greenwood at Stockholm University, your constant positivity and support throughout this project is greatly appreciated. Thank you Henry and Sarah for providing me with the bathymetry data on which this whole project is based. I further appreciate your support of all my crazy ideas of wanting to do things my way which have led to the creation of IceHot2, a Python program that calculates spatial statistics of polygons.

To my Ultimate Frisbee team, The Arctic Ternovers, you have kept me in shape, physically, but more importantly, mentally, for the past two years. I am certain that I will see you again. Special thanks to Rasmus Andersen, you know why.

And lastly, a very special thanks to Mathilde Lyford Jahnsen, co-student and friend, and Iver Magnarson Nypan, co-student and room-mate (and friend). Mathilde, I know I can be insufferable and I appreciate you putting up with me as a friend for all this time. Iver, you can not fathom the appreciation I have for your cooking and kombucha brewing.

Contents

1

Introduction

We are witnessing a rapid change in the Earth's systems that adversely impacts life on this planet. One of the major concerns is the effect that anthropogenic release of greenhouse gases has on the cryosphere (Constable et al., 2022). Increased atmospheric temperatures have already impacted more vulnerable glaciers, which have greatly reduced in size, and its effect on ice sheets is starting to become apparent (Constable et al., 2022). Both the Greenland Ice Sheet and the West Antarctic Ice Sheet have started a rapid retreat. For the Greenland Ice Sheet, the current retreat is dominated by an increase in surface meltwater production (Shepherd et al., 2020), whereas the retreat of the West Antarctic Ice Sheet occurs mainly through an increase in basal mass loss and calving fluxes (Depoorter et al., 2013). Changes in the behavior of modern ice sheets are focused in concentrated ice drainage routes called ice streams (Shepherd & Wingham, 2007). Ice streams represent parts of an ice sheet that flow more rapidly than the surrounding ice mass (Swithinbank, 1954) and they account for a significant proportion of the total ice loss of ice sheets (Bamber et al., 2000). There is a concern for the future stability of modern marine-terminating ice sheets as the grounding line retreats into deeper waters thus initiating a positive feedback loop of increasing ice discharge at the margin (Schoof, 2007). In short, as the water-terminating margin retreats on a reversed slope, the ice thickness of the margin increases as the lower limit of ice thickness is controlled by floatation. An increased ice thickness of the margin promotes an increase in ice discharge thus further shrinkage of the ice sheet (Schoof, 2007). An increase in water at the base of an ice stream has been suggested to promote ice flow velocity which in turn promotes loss of ice in the ice-marginal zone (Zwally et al., 2002). A rapid collapse of ice sheets has occurred before at the termini of major glaciations (Brendryen et al., 2020) and as history repeats itself, we look to the past to understand the present and predict the future.

Predicting the timeline and processes of a modern ice sheet collapse is today mainly achieved through numerical modelling. The numerical models require input data, such as

physical parameters that control the ice sheet stability, and known outcomes for model validation. This study aims to provide both. The detailed study of meltwater landforms can reveal the process by which meltwater wasting is achieved in a collapsing ice sheet, while both meltwater landforms and adjacent glacial landforms provide potential validation points for numerical models of the ice sheet collapse. Meltwater landforms can themselves suggest processes via geological and geomorphological interpretation, and together with other landforms, constrain numerical model investigations. Eskers are the most typical meltwater landform that have been used in this way but 1) their formation is not fully understood and 2) they are rarely found in marine-terminating settings (Greenwood et al., 2016). This study aims to investigate the morphological expression of channelized meltwater routing in marine-based ice sheet settings and explore the potential to use palaeo-meltwater landforms to infer past meltwater sources, fluxes, and organization during deglaciation.

1.1 Study areas

A significant basis for this study were two separate discoveries of esker systems in marine-terminating parts of the EISC. The Geological Survey of Sweden (SGU) carried out the mapping of Hoburgs bank (Figure 1.1, left) in the Baltic Sea in the years 2016 and 2017 (Kågesten et al., 2020). The area was investigated to map benthic habitats following its designation as a Natura 2000 marine protected area. A bi-product of the high-resolution bathymetry mapping carried out by the SGU was the discovery of ridge-like landforms on the Hoburgs bank that are thought to be eskers (Greenwood et al., 2024). Although the area is shallow, between 10-63 meters water depth, it is assumed that the ice margin was water-terminating during retreat since the area has experienced constant uplift since the Last Glacial Maximum (LGM) (Uścinowicz et al., 2003). The second area of interest is Hopendjupet, which lies in the Central Barents Sea. Between the years 2020 and 2022, the Center for Arctic Gas Hydrate, Environment and Climate (CAGE) targeted Hopendjupet to investigate and map gas seepage in Hopendjupet. A total of four scientific cruises were conducted in the area and along with discovering gas seepage in the area, so too did they discover esker systems (Patton et al., 2020; Serov et al., 2022; Winsborrow & Knies, 2021; Winsborrow et al., 2021). The two areas are in many ways quite different but they do share esker systems that seemingly formed in water-terminating ice streams during the collapse of the EISC.

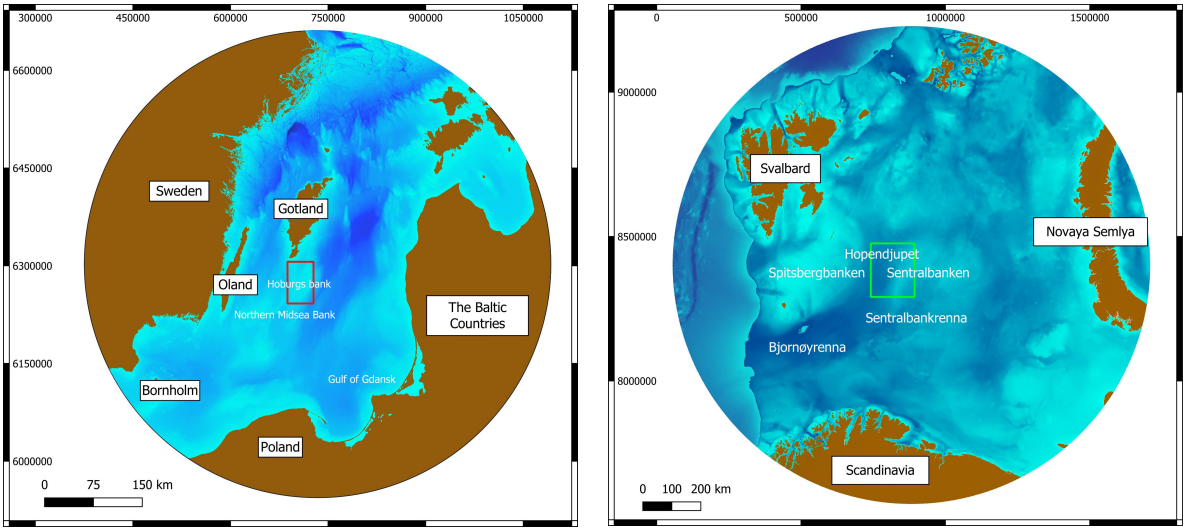

Figure 1.1: Overview figures of the two study areas. Left: Hoburgs bank in the Baltic Sea, bathymetry from the EMODnet dataset (tiles D6 and D7), coordinates are in the coordinate reference system EPSG:3006. Right: Hopendjupet in the Barents Sea, bathymetry and topography from the IBCAO version 4.2 dataset, coordinates are in the coordinate reference system EPSG:32634.

1.2 A summary of the rise and fall of the Eurasian Ice Sheet Complex

At the peak of the last ice age, aptly referred to as the Last Glacial Maximum, a massive ice sheet covered the northernmost landmasses and shallow seas of Eurasia. The EISC formed and coalesced from three distinct ice sheet nuclei. These were the Celtic Ice Sheet (CIS) over the British Isles, the Fennoscandian Ice Sheet (FIS) over Scandinavia, and the Barents Sea Ice Sheet (BSIS) on the Barents Sea and the Kara Sea. During the build-up of the ice sheets in the Weichselian, the three nuclei remained mostly detached from one another (Patton et al., 2016).

The following paragraph is in its entirety based on Patton et al. (2016).

The build-up of the EISC started when the climate deteriorated in the Late Weichselian. Icecap remnants from the Mid-Weichselian glaciation started to accumulate ice and advanced. The FIS formed via the convergence of independent ice caps in northern and southern Scandinavia. The BSIS grew over the landmasses surrounding the Barents Sea, reaching the shelf break to the north and west. The CIS formed as mountain glaciers grew and coalesced over the British Isles. The growth of the three ice sheets continued until a maximum was reached during the LGM, by which point all ice sheets had merged. The FIS and BSIS merged around 24.5 ka BP and the FIS and CIS merged around 23 ka BP, into one uninterrupted ice mass. The FIS and CIS remained mostly terrestrial-based, though whereas the eastern part of the FIS drained onto land, the CIS almost exclusively drained

into marine environments. The BSIS had formed a largely marine-based ice sheet as the terrestrial-based ice caps converged and the central ice divide shifted onto the Central Barents Sea (Patton et al., 2016).

The following paragraph is in its entirety based on Patton et al. (2017).

The period where all three ice sheets were merged was relatively short with the FIS and CIS splitting around 22.4 ka BP. The FIS and the BSIS remained coalesced until 15.5 ka BP. Although retreat of the EISC had commenced already immediately following the LGM, it was asynchronous with parts of the FIS not reaching its maximum extent until ca. 18 - 16 ka BP. The most intense retreat of the EISC coincides with the Bølling-Allrød warming at 14.9 ka BP. By the start of the Younger-Dryas the CIS was limited to scattered ice caps and the BSIS had completely retreated to the landmasses surrounding the Barents Sea. The FIS was arguably the least affected by the Bølling-Allrød interstadial, as it still covered most of Scandinavia and the Gulf of Bothnia by the onset of the Younger-Dryas. The onset of the Younger-Dryas saw a readvance of the FIS and the reappearance of glaciers in the Scottish uplands. The BSIS experienced little to no advance during this period. Any remnants of the EISC were completely gone by 8.7 ka BP as its final position in northern Scandinavia disappeared (Patton et al., 2017).

A major contributor to the rapid collapse of the EISC were streams of fast-flowing ice that moved large masses of ice from the central parts of the ice sheets towards the margins. Our study areas are located in or near two of these ice streams, the Bjørnøyrenna and the Baltic Sea ice streams. Troughs carved out by these ice streams channeled meltwater into drainage pathways, further increasing the streaming velocity and accompanying loss of ice at the margins (Winsborrow et al., 2010).

1.3 On the channelised flow of meltwater in a body of ice

The inherent nature of water to flow down hydraulic gradients while concentrating into flow arteries (Röthlisberger, 1972) allows for some basic assumptions on the nature of channelised meltwater flow in bodies of ice. There are four potential modes by which a meltwater tunnel or channel can exist on, in, or under a body of ice (Figure 1.2).

Meltwater formed from surface melting of ice will initially flow in a supraglacial stream (e.g., Pitcher & Smith, 2019, Figure 1.2A). The water surface is in contact with the atmosphere so the hydraulic pressure of the drainage system is equal to atmospheric pressure. Sediment transport in supraglacial streams is typically low and dependent on the sediment

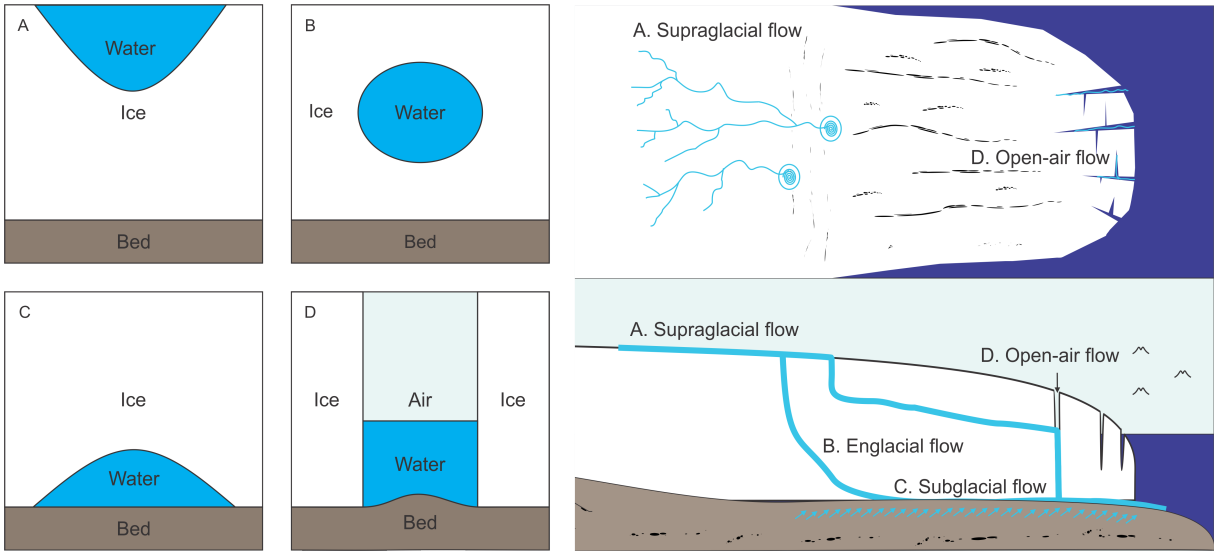

Figure 1.2: A sketch of various potential esker forming glacial meltwater channels. A: A supraglacial channel, water flows on top of the ice. B: An englacial channel, the water flow is suspended within the glacier. C: A subglacial channel, the water flows along the base of the ice. D: An open-air channel, glacio-static pressure does not affect the water flow as the channel is open towards the atmosphere. Top right: Top-view of an ice margin. Bottom right: Cross-section of an ice margin.

concentrations of the ice surface (Pitcher & Smith, 2019). Supraglacial streams are often highly sinuous (observed sinuosity as high as 2.0) and they meander (Germain & Moorman, 2019). Surface melt availability is seasonally dependent and supraglacial streams are rarely active for more than one melt season (Pitcher & Smith, 2019).

Once the flow reaches openings (cracks, crevasses, moulins, etc.) in the ice it will follow said openings and flow englacially (Shreve, 1972, Figure 1.2B). Now the water is no longer in contact with the atmosphere and the hydraulic pressure becomes dependent on the height of a water column reaching from the point where water was in contact with the atmosphere down to the englacial water flow. As the ice in itself will internally deform, the hydraulic pressure inside the englacial tunnel has to overcome that of the overburden pressure exerted by the overlying ice column to maintain the tunnel (Röthlisberger, 1972). As such, if the hydraulic pressure does not exceed that of the overburden, the tunnel will close and the water will need to find another path in a process termed cut-and-closure (Vatne & Irvine-Fynn, 2016). Flowing water in contact with ice will create heat via frictional forces, which contribute to the melting of adjacent ice (Röthlisberger, 1972). Sediment supply in englacial channels is still controlled entirely by the sediment contents of the ice body. However, as the flow path lengthens, sediments are sourced from a larger catchment.

Water flowing between the base of the ice body and the bed is said to flow subglacially (Röthlisberger, 1972, Figure 1.2C). Here the water is sourced not only from surface melt but also by drawing in water from saturated sediments underneath the ice. The channelised

flow is now in direct contact with a fresh supply of sediments and depending on the characteristics of the bed, can either erode the bed, forming an erosional channel termed a Nye-channel (N-channel, Weertman, 1972) or the flow can cut into the ice forming a Röthlisberger-channel (R-channel, Röthlisberger, 1972). Eskers are typically considered to represent former R-channels (Brennand, 2000). Note that the characteristics of en- and subglacial channels assume a filled tunnel. If the tunnel were to be partially empty, the same principles would apply as to a supraglacial channel.

Lastly, water can concentrate in open-air cracks and crevasses in the ice, termed H-channels, where water flow is in contact with the bed and the atmosphere, but is limited in its ability to meander by walls of ice (Hooke, 1984, Figure 1.2D). In an open-air channel, overburden pressure does not affect the flow of water, and sediments are abundant. Furthermore, the pressure exerted by the surrounding ice on the bed can cause the sediments to be pushed into the crevasse, adding to the height of sediments deposited from the meltwater.

1.4 An introduction to eskers

At its most basic, an esker is a positive depositional landform, where sediment deposition occurs in a channel that was confined by ice on at least two sides (they can be enclosed on all four sides). Eskers form straight- to sinuous ridges that may be composed of esker ridge segments or esker beads that align to form esker systems.

The term "esker", derived from the Irish word *eiscir* or the Welsh word *escair* (both of which translate to the English word *ridge*), was first used in its current meaning by Rev. Maxwell H. Close in 1866. Close (1867) described esker ridges in comparison to “parallel ridges which consist of drift... whereas esker ridges are usually irregular, often very sinuous, and without any general direction.” (Close, 1867). Since the first rudimentary description of eskers in the 19th century, the importance of studying eskers has become abundantly clear as they reflect meltwater drainage beneath ice sheets (Storrar et al., 2014). Many of the fundamental discoveries on esker dynamics were published in the 1970s, when Röthlisberger (1972) proved that meltwater within glaciers flows down pressure gradients and accumulates in flow arteries and that the size of a meltwater conduit within a glacier rapidly responds to fluctuations in meltwater discharge. Shreve (1972) showed that meltwater within a glacier preferentially moves in tunnels and that esker formation is more likely in low glacier-surface gradient during high meltwater discharge.

Recently, a significant effort has been made to compile mapped eskers in the northern hemisphere into large datasets (e.g. Clark et al., 2004; Hättestrand & Clark, 2006; Storrar

et al., 2014). The large number of eskers mapped has allowed for statistical descriptions of esker length, sinuosity, and lateral spacing, among others, between regions (Storrar et al., 2014). These large datasets have so far only focussed on terrestrial eskers, this is most likely due to available digital elevation model (DEM) coverage.

One of the most common points of debate when it comes to eskers is regarding the timing of their formation, that is whether an esker forms synchronously along its entire length or that its formation is time-transgressive, meaning that the esker forms continuously at or near the ice-margin as the margin retreats (e.g., Greenwood et al., 2016). Storrar et al. (2014) noted that the longer eskers, more than a few 10s of kilometers, formed during the retreat of the Laurentide Ice Sheet could not have formed synchronously. It is therefore likely that, at least, longer eskers are formed time-transgressively and changes along its length reflect changes in the ice-margin dynamics during retreat.

When researching eskers, one is quick to notice that they are often, if not always, described as being sinuous. In his description of eskers, Storrar et al. (2014) found that, for a large dataset, eskers are more straight than they are sinuous. It is also interesting to note that the sinuosity of the eskers decreases with length, suggesting that longer conduits are controlled by hydrostatic pressure. Highly sinuous eskers are thought to form under atmospheric pressure near the ice margin (Storrar et al., 2014).

Recently, on Hørbybreen in Svalbard, a ground-penetrating radar (GPR) was used to unequivocally prove that meltwater flows in all of the channel modes mentioned in Figure 1.2, even at the same time (Storrar et al., 2020). Eskers have been found to form from any channel mode (e.g., Price, 1969). Variations in the esker crest shape have been attributed to differing formational channel modes (Perkins et al., 2016).

Although this study lacks any investigation into sediment features, a short overview of esker sediment characteristics follows. Banerjee and McDonald (1975) provided the first models for esker sedimentation, based on their study of the Windsor and Peterborough eskers in the District of Keewatin in Canada. Their work largely holds to this date and provides a good basis for describing esker sediment characteristics. Eskers contain grain sizes ranging from clay to gravel, with the finest fraction (very fine sands, silts, and clays) being absent in eskers formed in en- or subglacial tunnels. Sedimentary structures are reflective of the uni-directional transportation flow and include structures such as; parallel beds, cross-bedding, cross-lamination, and antidunes. Graded bedding of very fine sands and silts and rhythmic laminae of silts and clays is indicative of esker formation in a standing body of water (deltaic sedimentation). Eskers of an open-air channel origin can form antidunal backset beds whereas planar or tabular parallel beds are more likely a

product of a tunnel channel (Banerjee & McDonald, 1975).

1.5 Types of eskers

Eskers take on various morphological expressions which allows for their classification into types. The different types of eskers are indicative of their depositional setting and the nature of the drainage system that they represent. The following summary is not conclusive of all esker types but focuses on esker types discussed in this study.

Esker enlargements are parts of esker ridges that are more than 5 times wider than the trunk esker (main esker) (Lindström, 1993). In the original description of esker enlargements, the term was used to describe, single-crested, flat-topped, esker sections that were both wider and higher than the trunk esker (Lindström, 1993). Since then the type has been adopted to refer to a variety of enlarged forms such as complex esker enlargements that exhibit ridge divergence and convergence (Dewald et al., 2021). In short, there are two competing theories on the formation of esker enlargements. Firstly, Stoker et al. (2021) suggest a deltaic deposition model where the esker enlargement forms at the mouth of a subglacial drainage conduit in a sub-aqueous setting. Secondly, Dewald et al. (2021) suggest that esker enlargements are formed by flattening of a subglacially deposited esker via a collapse of the conduit roof.

Complex eskers is used as a term to describe eskers that have multiple distributaries and/or tributaries (Storrar et al., 2015). The primary control on complex esker formation, in contrast to simpler forms containing less branching, has been suggested to be heightened meltwater and sediment flux. During high meltwater and sediment fluxes the drainage conduit could be overwhelmed by sediments forcing the formation of new drainage routes (Storrar et al., 2015).

Beaded eskers are a succession of circular to slightly elongated mounds (beads) that align to form a sinuous esker system (Banerjee & McDonald, 1975). Individual beads are formed time-transgressively at or near the water-terminating ice margins as the flow velocity of water decreases (Banerjee & McDonald, 1975). It has been suggested that the timing of their formation is limited to one or a few melt seasons and that they represent a quasi-annual record of esker deposition (Banerjee & McDonald, 1975; Livingstone et al., 2020; Mäkinen, 2003).

Esker corridors are eskers that form inside of erosional corridors (N-channels) and often terminate in a deltaic outwash fan deposit (Cummings et al., 2011). The eskers are either

formed time-transgressively as repeated sections of eskers and fans where each section is formed synchronously or as one long synchronous deposit of esker and fan (Cummings et al., 2011). A similar esker planform has been described for N- and R-channel eskers where the high continuity of synchronously deposited esker corridors has been attributed to low hydraulic pressure (water pressure) inside of the N-channel (Frydrych, 2022). The change from an erosional N-channel to a smaller depositing R-channel has been explained by a variable pressure model where decreasing meltwater fluxes cause the subglacial conduit to narrow and lose the capacity to erode into the substrate, thus switching to deposition along the entire length of the subglacial conduit (Lewington et al., 2020; Sharpe et al., 2021).

Till eskers, also called sediment supply limited eskers, are not composed of glaciofluvial sediments like other eskers but instead are made up of basal till (Christoffersen et al., 2005). They are considered eskers based on their sinuosity resembling that of other esker types and are thought to have formed by basal squeezing of sediments into subglacial sediment-deprived meltwater conduits (Evans et al., 2010).

Geometric and Sinuous Ridge Network (GSRN) is a term recently adopted to describe complex networks of cross-cutting linear and sinuous ridges (Evans et al., 2022). The terminology builds on previously described geometric-ridge network (GRN) that are composed of crevasse-infill and crevasse squeeze ridges (subglacial sediment fill of basal crevasses) forming rectilinear patterns reflecting the stress field of an ice margin (Bennett et al., 1996; Evans et al., 2016) to include sinuous ridges (Evans et al., 2022). In addition to the crevasse-fill ridges, the sinuous ridges are interpreted as till eskers (Evans et al., 2022).

Long, dendritic eskers form in extensive R-channels, tens to hundreds of kilometers long (Brennand, 2000), that often include tributary eskers of up to the fourth stream order (Storrar et al., 2014). Stream order refers to the number of times channels converge, for example, a tributary to a tributary is of the second stream order. Brennand (2000) favours a synchronous mode of deposition along the entire length of the R-channel, Storrar et al. (2014) note that longer eskers (several tens of kilometers) are more likely formed time-transgressively at or near the margin.

The various esker types described above represent a continuous spectrum where an esker system (a collection of individual esker ridges and/or beads) often gradually changes from one type to another. For example, esker enlargements are usually connected to a trunk esker and often change from single-crested enlarged features to complex enlargements (Dewald et al., 2021). Beaded esker systems have been noted to exhibit a gradual change from a highly fragmented network of beads to a continuous ridge (Livingstone et al., 2020).

2

Project aim

This study aims to investigate the morphological expression of channelised meltwater routing in marine- and lacustrine-terminating ice streams with a special focus on esker systems. The morphometry and distribution of eskers will be used to infer drainage pathway characteristics and controls on esker sedimentation in non-terrestrial settings.

Research questions:

1. What characterises eskers in marine- and lacustrine-terminating ice sheet margins and how do they differ from their terrestrial counterparts?

2. What do the size, distribution, and spatial arrangement of eskers tell us about the palaeo-drainage of a retreating ice sheet?

3. How well do current ideas for esker formation and morphological expression correlate to the eskers observed in the Central Barents Sea and Baltic Sea which span a diverse range of depositional settings?

To answer these questions a detailed geomorphological investigation is carried out of the two study areas as well as simple numerical modelling of drainage pathways in modelled palaeo-ice sheets.

3

Data and methods

The main basis for this study is two discoveries of potential esker systems in the Barents Sea and the Baltic Sea found with the aid of high-resolution multibeam swath bathymetry (HMSB). This study aims to show that eskers are present in both study areas, Hoburgs Bank and Hopendjupet, and that they were formed in water-terminating ice streams. The presence of eskers will be confirmed by comparing morphological features of visually identified landforms with previously described eskers. Visual mapping was conducted in the program QGIS (version 3.34.4). As the bathymetry does not reveal the internal structure of the landforms, it was not possible to perform a sedimentary facies analysis. Landforms other than potential eskers were mapped to investigate the relationship of eskers with other landforms. Statistical attributes of esker ridges were calculated with the aid of a program written in Python (version 3.12.0). In the case of the Hoburgs bank dataset, the distinction between esker ridges and other ridge- or mound-like landforms proved difficult by visual mapping. As such, ridges and mounds mapped on the Hoburgs bank were categorized into groups by statistical attributes and the strength of backscatter reflection.

3.1 Data sources

HMSB and acoustic backscatter data were provided by Dr Henry Patton and Dr Sarah Greenwood. The Hoburgs bank dataset is freely available, although at a lower resolution (5 by 5 meters), while the Hopendjupet dataset is not available online. As such, the references in Table 3.1 for Hopendjupet HMSB are for the four cruise reports and not for an open dataset, in contrast to the Hoburgs bank reference. Lower resolution large-scale bathymetry (LLSB) was used to extrapolate features that extend outside of areas covered by HMSB and to visualise large-scale bathymetry in overview figures.

Table 3.1: Data sources and cruise reports.

Data type	References
Hoburgs bank	
HMSB and backscatter	SGU[a]
LLSB	EMODnet (tiles D6 and D7)[b]
Hopendjupet	
HMSB	CAGE 20-2 (Patton et al., 2020)
	CAGE 21-4 (Winsborrow et al., 2021)
	CAGE 21-6 (Winsborrow & Knies, 2021)
	CAGE 22-6 (Serov et al., 2022)
LLSB	IBCAO version 4.2 [c] (Jakobsson et al., 2020)
Numerical modelling	
LLSB	GEBCO 2023 Grid[d] (GEBCO Compilation Group, 2023)

a. https://www.sgu.se/produkter-och-tjanster/geologiska-data/oppna-data/maringeologi-oppna-data/habitatkartering-hoburgs-bank-oppna-data/
b. https://emodnet.ec.europa.eu/geoviewer/
c. https://www.gebco.net/data_and_products/gridded_bathymetry_data/arctic_ocean/#terms
d. https://www.gebco.net/data_and_products/gridded_bathymetry_data/#global

The Hopendjupet and Hoburgs bank datasets vary not only in morphological features but also with regard to their spatial extent and resolution. Table 3.2 summarises the main differences between the two datasets.

Table 3.2: Dataset information

	Hopendjupet	Hoburgs bank
DEM resolution	8 m by 8 m	1 m by 1 m
Study area[a]	28,089 km^2	2561 km^2
DEM covered area	3144 km^2	1347 km^2
DEM percentage coverage	11%	53%
DEM file size	208 MB	4.78 GB
Water depth ranges	147 to 400 m.b.sl.	14 to 61 m.b.sl.

a. The area of a rectangle that encapsulates all HMSB data in the area

The differences between the two datasets provide challenges for comparing their mapping interpretations (Figure 3.1). For Hopendjupet, the main challenge is the lack of coverage, which leads to gaps in interpretation. The Hoburgs bank has a much better coverage but the landforms themselves are smaller and more fragmented which results in a higher complexity of their mapping.

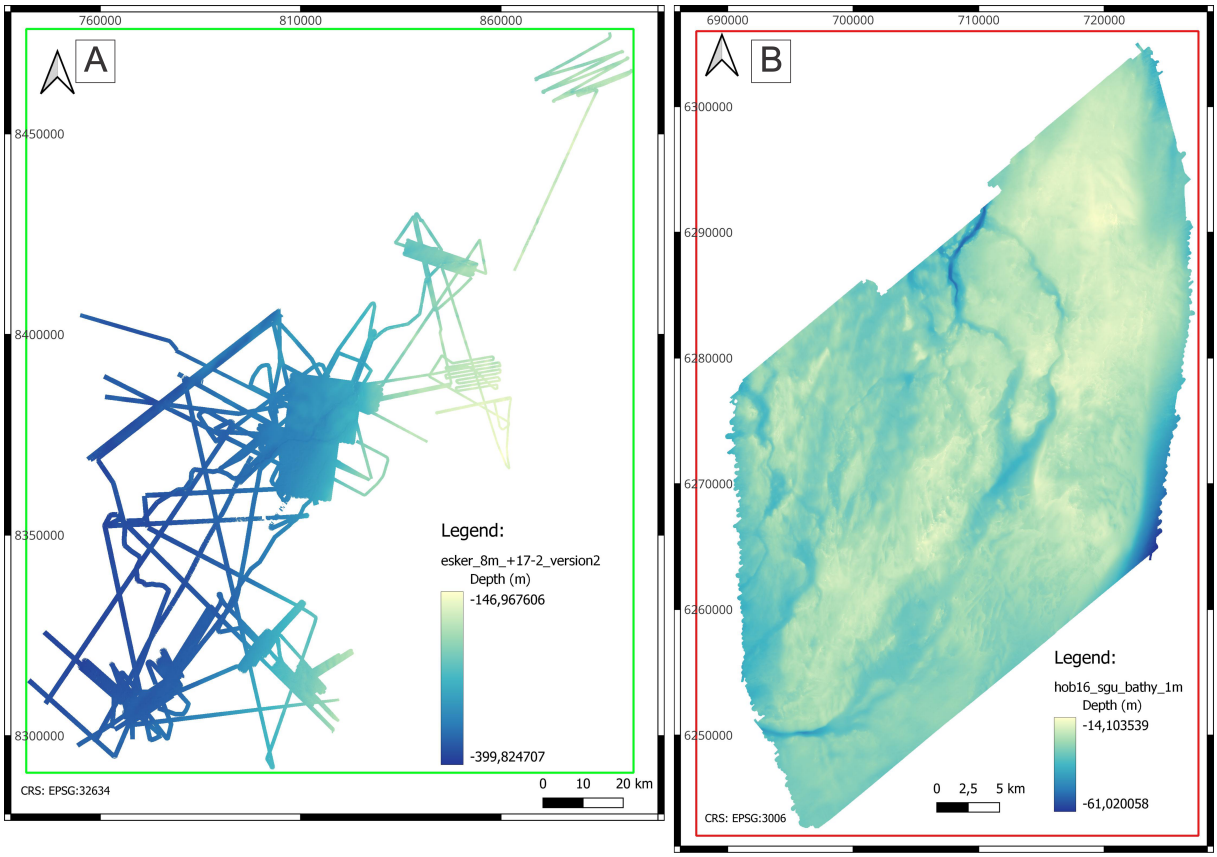

Figure 3.1: Overview of the available HMSB. A: Hopendjupet, B: Hoburgs bank.

3.2 Bathymetry

Multibeam swath bathymetry

The HMSB (1 by 1 meters in Hoburgs bank and 8 by 8 meters in Hopendjupet) was acquired via the use of a multibeam echosounder (MBES). MBES systems rely on the same principle as any other echosounder system whereby an acoustic signal is transmitted with a known frequency. A receiver measures the time it takes the signal to travel to the seafloor and back, and this time is denoted the two-way travel time (twt). MBES systems differ from single beam echosounder (SBES) systems in that they emit a signal in a fan, as opposed to the single-beam emitted from a SBES thus measuring the depth of multiple points along a line that is perpendicular to the ship track. In contrast, SBES systems only measure the depth directly underneath the transmitter.

Uncertainties in measured depth from MBES systems can originate from multiple sources. The depth is converted from the measured twt in the time domain to the depth domain. Conversion from the time domain to the depth domain is achieved with the aid of sound velocity profiles. Sound velocity profiles are calculated from data gathered by a Conductivity, Temperature, and Depth (CTD) instrument at regular intervals. Inaccuracies in the sound

velocity profile will be reflected in systematic errors which often present as smiles or frowns in MBES data. The measured depth is aligned so that the zero-depth lies at sea level, for that purpose corrections have to be made for tides. Incorrect tidal corrections will present themselves as misaligned survey lines. Other factors that need to be corrected are e.g. roll, pitch, yaw, and latency, all of which can be minimised by performing a patch test, whereby a distinct feature is crossed at different speeds, back and forth, and at each set of outer beams of the MBES (Sandwell et al., 2002, mbes).

Table 3.3: Configuration of MBES systems for the various cruises from which the bathymetric data in this study was compiled. In the table, KS stands for Kongsberg Simrad. *The sampling rate exceeded 5 Hz in shallow waters around the island of Hopen.

	SGU Hoburgs bank surveys	CAGE surveys
Years of survey	2016 -2017	2020 -2022
MBES system	KS EM2040	KS EM302
Nominal sonar frequency	300 kHz	30 kHz
Sampling frequency	50 Hz (max.)	0.5 - 2 Hz*
Nominal sound frequency	300 kHz	30 kHz
Beams per ping	256 (515?)	432
Maximum angular coverage	200°	150°
Opening angle		60°/60°

LLSB

The collection of high-resolution bathymetric data is limited by the coverage extent of the multibeam swath. To get an idea of the large-scale bathymetry extending beyond the available high-resolution bathymetric data, and in the case of the Hopendjupet data, to fill in the gaps between swaths, lower-resolution bathymetric datasets were layered beneath the high-resolution bathymetric data.

3.3 Backscatter

In addition to depth information, the MBES also collects data on the strength of the returning signal, known as acoustic backscatter (Kågesten et al., 2020). The strength of the acoustic backscatter at frequencies used in seafloor mapping, in the order of tens to hundreds of kHz, is determined by two main contributing factors; the roughness of the seafloor and heterogeneities included in the sediment volume. These heterogeneities may have various origins, e.g. gas bubbles, shells, mineral inclusions, bioturbation, and more (Lurton, 2002). Other factors that affect the strength of the acoustic backscatter, such as wave attenuation in the water column, are well understood and can be corrected for.

The many possible causes for variations in acoustic backscatter make the interpretation of such data difficult. Therefore, in the case of the Hoburgs bank survey, acoustic backscatter was used alongside ground truthing (sediment samples and underwater imagery) methods as predictors in the modelling of seafloor characteristics (Kågesten et al., 2020). In this study, backscatter information is only available in the Hoburgs Bank study area SGU analysed backscatter data to produce sediment hardness and grain size maps, which proved useful in determining the extent of the channel system on Hoburgs Bank.

3.4 Visual mapping

The first step in mapping eskers on Hoburgs Bank and in Hopendjupet was taken by visually mapping the extent of esker-like ridges and mounds. This method involved visualising the data in QGIS and creating polygons that encapsulate potential esker ridges and mounds. Assessing the extent of the esker ridges was aided by creating bathymetry-derived maps utilising gdaldem packages which are a part of the GDAL software. Two gdaldem packages were used to create bathymetry-derived maps: firstly a gdaldem hillshade map was created to shade the bathymetric data, and secondly, a gdaldem slope map was created to visualise slope breaks. Hillshade maps were layered over bathymetric data and their transparency was reduced to 80% and utilised to identify potential eskers (Figure 3.2B). Once a potential esker had been identified a slope map was layered on top of the bathymetry and hillshade maps with a filter set so that only slopes above a set degree value were coloured (Figure 3.2C). A value of 5 degrees was chosen for the Hopendjupet study area and a value of 10 degrees was chosen for Hoburgs Bank, the difference was due to a higher "roughness" of Hoburgs Bank which meant that individual features became lost to noise at lower than 10-degree slope filter. The outer edge of the visible slope map was traced to create a polygon that expressed the extent of the potential esker (Figure 3.2D).

3.4.1 Landforms other than eskers

Non-esker-type landforms were mapped to gain a complete understanding of the study areas. The juxtaposition and spatial distribution of non-esker-type landforms were compared to that of the identified esker ridges and esker beads which can be used to identify the order of processes forming said landforms.

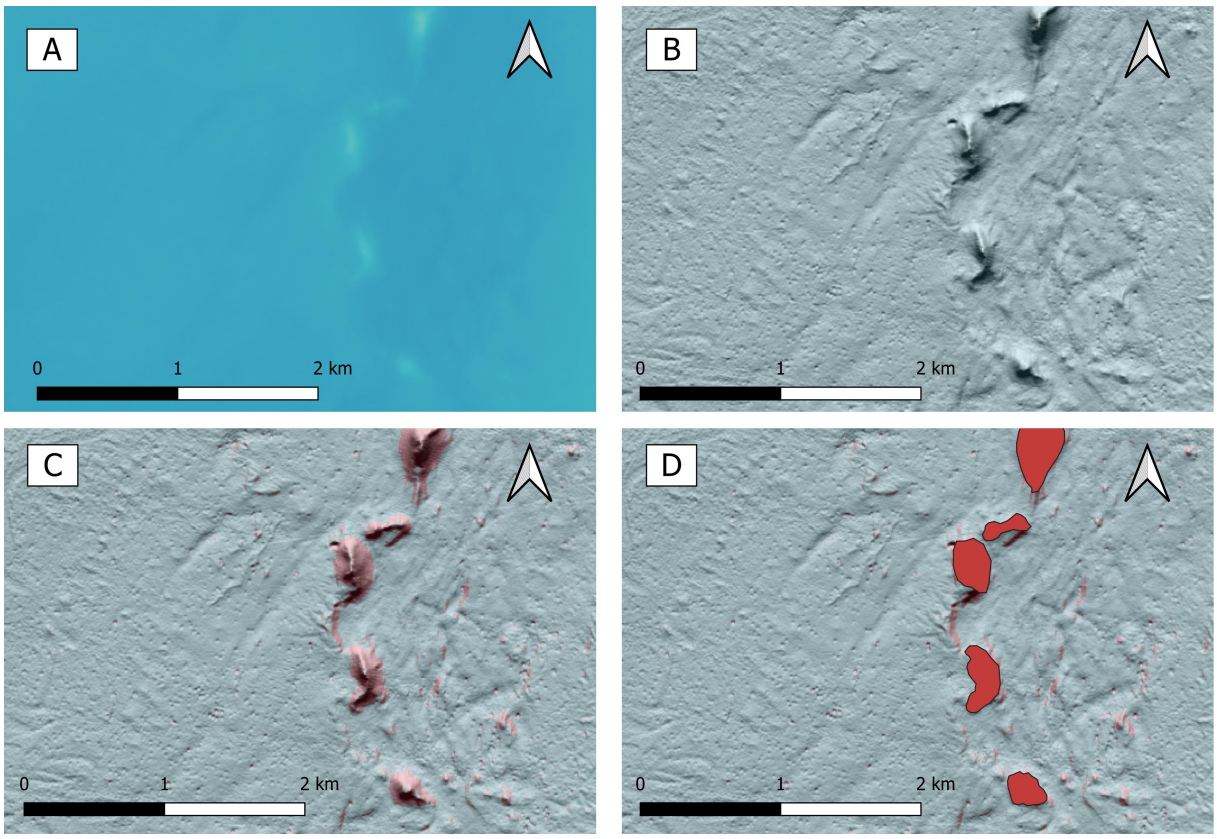

Figure 3.2: Procedure for visually mapping eskers, an example of esker beads from Hopendjupet. A: Bathymetry. B: Hillshade map layered over the bathymetry. C: Slopes above 10 degrees visualised. D: Polygons mapped encapsulating slopes above 10 degrees.

3.5 Automated statistical analysis

Extracting polygon statistics was done with a program I wrote for this project which is called IceHot2. IceHot2 will be published as an open-source Python package on GitHub[1]. The function of the program is to take in polygons and a DEM to calculate spatial attributes of features within the polygons. As is known to readers who are familiar with Geographic Information System (GIS) software, many of the attributes that I have chosen to calculate in IceHot2 can easily be calculated in GIS. What motivated me to write my own program was the fact that QGIS has a tendency to create new layers for every step of the calculation, and with the size of my data files, these layers quickly filled up the disk space on my computer. I, therefore, wrote IceHot2 to automate the calculation of polygon attributes and skip unnecessary disk space usage.

A range of attributes was calculated to statistically describe potential eskers. Below is a description of each of these attributes. Names of geometries follow the Shapely o Python package as it was used in IceHot2 and adequately differentiates between vector geometry types.

Length

The length of a polygon was defined to be the length of a linestring that follows the centerline of a polygon. The centerline linestring was derived from a Voronoi skeleton (Ogniewicz & Ilg, 1992), where the two vertices that are furthest apart from one another define the endpoints of the centerline, and the shortest path along the Voronoi skeleton between the two endpoints defines the centerline (Figure 3.3).

Sinuosity

The sinuosity of a polygon was defined as the length of a polygon divided by the distance between its edge vertices, or endpoints. Problems arise when comparing the sinuosity of esker ridge segments and esker beads with similar lengths and widths, and thus the edge vertices are nondescriptive for the polygon. A solution to this problem would be to infer a straight path between ridge segments or beads, thus assuming a much longer continuous esker.

1. https://github.com/teiturh97/polygon-statistics

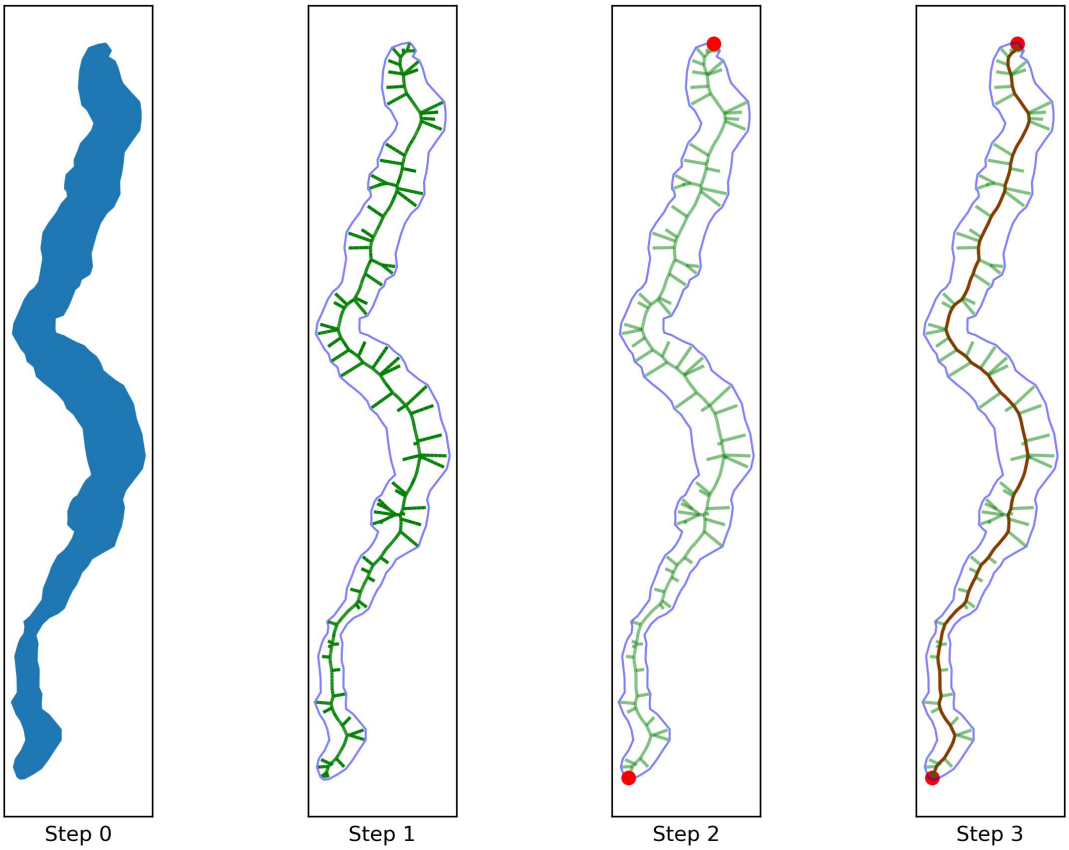

Figure 3.3: Step-by-step approach to finding the centerline of a polygon. Step 0: Shows the input polygon (blue), feature identification number (fid): 1548, from the Hoburgs bank dataset. Step 1: Create a Voronoi skeleton of the polygon (green). Step 2: Find the two extremities of the skeleton (red points). Step 3: Find the shortest path between the two extremities (red line) marking the centerline, the length of which is used as the length of the polygon.

Width

The width of a polygon was estimated as the width of linestrings that are perpendicular to the centerline and their extent is limited to be within the polygon. To create linestrings perpendicular to the centerline, points were created along the centerline at a defined interval. The angle of the linestring segments on which the points lie is used to define an angle that is rotated 90 degrees and corresponds to a point along the centerline. From there, a new linestring is created for each point along the centerline that has a length that is no less than the widest polygon in the dataset. Finally, the perpendicular linestrings are cropped to fit within the polygons and their length defines the width at a given point along the centerline. The **maximum width** of a polygon corresponds to the longest perpendicular linestring to the centerline. Having calculated multiple widths for each polygon, statistics such as **average width** and **width standard deviation** can be extracted (Figure 3.4).

Height

Similarly to width calculations, the height of a polygon was defined for linestrings perpendicular to the centerline of a polygon. Note that every point on a linestring is not defined in three-dimensional space, but linestring vertices can include an elevation variable. This is not useful for defining the height of a polygon as the linestrings perpendicular to the centerline are straight and thus only have two vertices, the endpoints. Therefore, once again points are created at a defined interval, preferably close to the resolution of the DEM for most accurate height estimations, along linestrings perpendicular to the centerline. Each point is given an elevation value from the DEM, and finally, the height for each linestring perpendicular to the centerline is calculated by subtracting the maximum elevation value from the minimum elevation value for a group of points that belong to the same linestring. From this, we can extract the **maximum height** of a polygon as the linestring perpendicular to the centerline that has the largest height difference. And, as per the width calculations, we can extract **mean height** and **height standard deviation**. A simpler method would be to subtract the maximum elevation value from the minimum elevation value for a group containing every point within the same polygon, however, this method ignores any height changes along the length of a ridge (Figure 3.5).

Derived values

Having calculated the various statistically descriptive attributes mentioned above, the maximum height cross-section was chosen to represent a polygon. Hence, each polygon was described as having a length, an area (simply applying the area of a polygon function

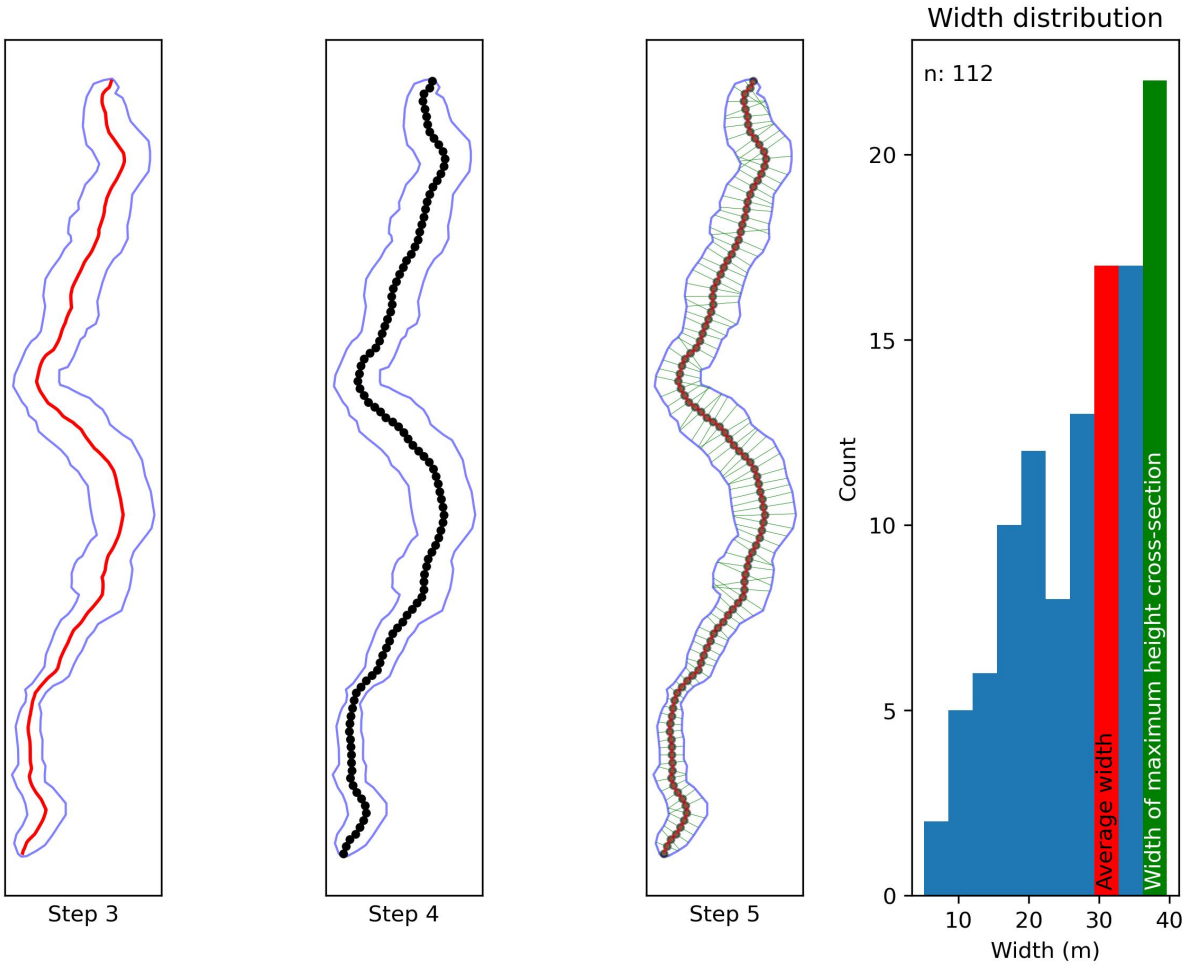

Figure 3.4: Continuing from Figure 3.3, we can create cross-sections along the centerline (Step 3). Step 4: Create points along the centerline at a given interval. Step 5: Draw cross-sections through each point along the centerline and perpendicular to it, and clip their extent to the extent of the polygon. The histogram shows the width distribution of this particular polygon, highlighting two potential metrics that can be used to represent the polygon width: average width (red), and the width of the cross-section which has the largest height difference (green), height is discussed in the next section.

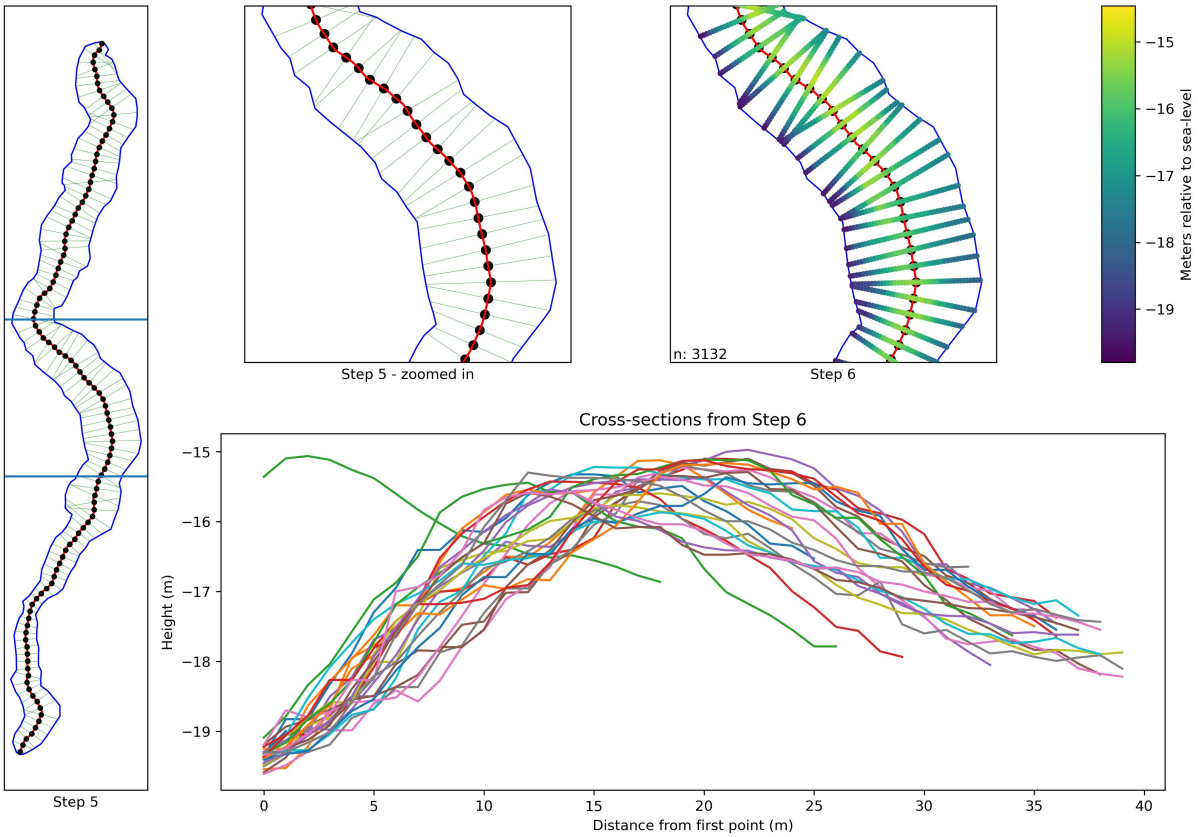

Figure 3.5: Having created cross-sections in Step 5 (Figure 3.4), we can start calculating the height of each cross-section. Here we zoom in on a part of polygon 1548, so as not to overcrowd the figure. Step 6: Create points along each cross-section at an interval preferably close to the DEM resolution and assign depth values from the DEM to each point. In the plot at the bottom of the figure we visualize the cross-sectional height of the polygon, this is not strictly important to any calculations, but properties of the cross-section, such as kurtosis and skewness, are related to this figure.

included in Geopandas), a maximum height, an average height, a standard deviation of height, a width (the width of the maximum height cross-section), an average width and a standard deviation of width. The **elongation ratio** of each polygon feature was calculated by dividing the length of the width of the maximum height cross-section. Although the sinuosity was calculated for all features, it was only included in the statistical description of features that had an elongation ratio greater than two and were defined as ridges. In contrast, features that had an elongation ratio less than or equal to two were classified as mounds (Table 3.4). Ridges were further classified as straight, slightly sinuous, or highly sinuous based on their sinuosity (Table 3.4).

Table 3.4: Nomenclature and chosen limits for describing potential eskers.

Elongation ratio	
Mound	< 2
Ridge	≥ 2
Sinuosity	
Straight	< 1.10
Slightly sinuous	≥ 1.10 & < 1.20
Highly sinuous	≥ 1.20

3.6 Numerical modelling approach

Using model outputs of the EISC reconstruction by ice sheet (Patton et al., 2017) a model of the subglacial hydrology was created for a range of time slices. The output of the model was used to assess the hydraulic pressure conditions that correlate to mapped meltwater features.

All modelling was carried out in QGIS (version 3.34.4). The primary inspiration for this modelling approach was a YouTube video on stream and catchment delineation in QGIS by Hans van der Kwast (2021) where he uses the PCRaster tools package (Karssenberg et al., 2010) to derive the Ruhr river catchment. Hans van der Kwast created a local drain direction network (LDD) from a DEM of the Ruhr valley. The LDD was subsequently used to derive a map of Strahler orders to filter out superfluous tributaries, resulting in a map of channels. The channel map was then used to determine the location of the Ruhr River outlet. The Ruhr River catchment was determined by taking all pixels of the LDD that drain into the pre-determined outlet.

My approach was in essence the same, although a simple DEM is not sufficient to determine the local drainage direction in a subglacial system. Instead, subglacial meltwater flows down hydraulic potential gradients. Hydraulic potential is a measure of the tendency of

water to flow, whereby the direction of flow goes towards the negative, much as water tends to flow towards lower elevation (Shreve, 1972). For determining hydraulic potential (ϕ), I used Equation 3.1 as, in addition to accounting for elevation potential and ice overburden pressure (Shreve, 1972), it takes into account the floatation factor (F) the ratio between subglacial water pressure and ice overburden pressure, when calculating the ice overburden pressure (Patton et al., 2017).

$$\phi = \rho_w g z_b + F \rho_i g (z_s - z_b) \tag{3.1}$$

where ρ_w and ρ_i are the density of water (1000 kg m^{-3}) and the density of ice (917 kgm^{-3}) respectively, g is the gravitational acceleration (9.81 m s^{-2}), z_b and z_s are the elevations of the bed and ice surface respectively, and F is the floatation factor. Elevation potential corresponds to $\rho_w g z_b$ and water pressure to $F \rho_i g (z_s - z_b)$.

For hydraulic potential modelling it was assumed that spatial and temporal variations in water and ice densities were negligible. It is well known that the floatation factor does vary both spatially and temporally depending on meltwater inputs, drainage system characteristics, basal ice temperatures, and substrate characteristics (Andrews et al., 2014; Kirkham et al., 2024). Modelling spatial variations in the floatation factor was deemed out of the scope of this study, instead, the model was tested against a range, of spatially constant floatation factors for each modelled time slice. This range included a purely topographic model where F = 0 and the ice thickness was completely ignored and, a model where the only variable was the ice surface elevation (z_s), thus completely ignoring any bed topography and simulating englacial or supraglacial flow. Note that a lower floatation factor results in a decreased influence of ice thickness on the location of drainage pathways beneath an ice sheet. However, subglacial channels are unlikely to form and be maintained in a subglacial hydraulic system where ice overburden pressure exceeds that of the hydrostatic pressure (as discussed in Section 1.3).

As for elevations of the bed and ice thickness that were used in Equation 3.1 model outputs for isostatic adjustment and ice thickness at different timeslices were used from Patton et al. (2017). The elevation of the bed was adjusted by using modern topographic and bathymetric maps (a mosaic of IBCAO version 4.2, Jakobsson et al. (2020), and the GEBCO 2023 Grid, GEBCO Compilation Group (2023)) and adding isostatic adjustment values from relevant timeslices resulting in the bed elevation at the desired timeslice. An ice surface elevation was directly inserted for $z_s - z_b$ in Equation 3.1. In all cases, input maps were resampled to a 500 m^2 resolution using bicubic interpolation with the GRASS7 algorithm r.resamp.interp. Note that the resampling of topography resulted in a lower resolution than the original (200 m^2 to 500 m^2) whereas resampling of the ice thickness and isostatic

adjustment maps resulted in a higher resolution than the original (10000 m^2 to 500 m^2). Increasing the resolution of model outputs (from Patton et al., 2017) was deemed to be valid due to the general "smoothness" of the isostatic footprint and ice surface topography.

The hydraulic potential map was simply substituted for a classic DEM while creating a LDD using the PCRaster tools algorithm `lddcreate`. The algorithm assigns a directional value to each pixel (from 1 to 9) towards the direction of the steepest downhill slope in neighbouring pixels, where 5 represents a flat pixel and other numbers represent directions (Figure 3.6). This method assigns a drain direction value to each pixel in the input hydraulic potential map, while ignoring any pixels that are not surrounded by valid hydraulic potential pixel values, as such any pixels touching the edge of the hydraulic potential map were ignored. The `lddcreate` algorithm also deals with pits, that is, a pixel where all neighbouring values have higher values than itself. In reality, pits would eventually be filled by accumulation of water which then would allow for overflow through an outlet. Thus, it is assumed that all flow in a catchment accumulates in a single outlet, and all pits in the catchment are filled.

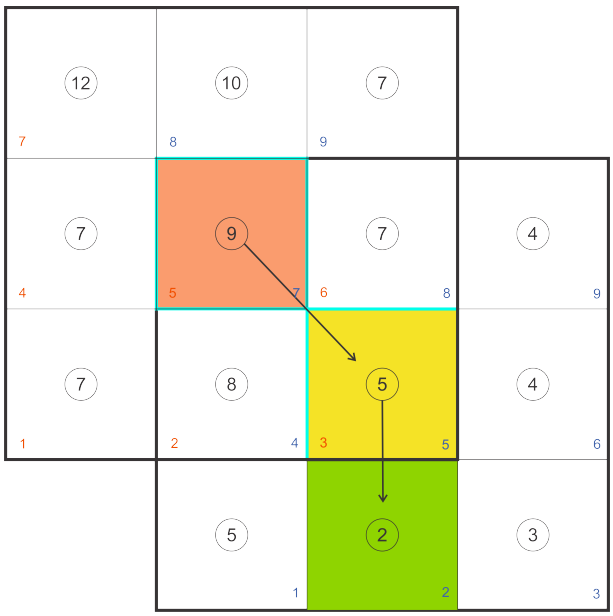

Figure 3.6: A sketch of how a LDD is created. Two 3 by 3 cells are shown with relative hydraulic potential values (circled numbers). The centre pixels are assigned a flow direction, e.g., the orange pixel flows towards the yellow pixel which flows towards the green pixel. The orange pixel gets assigned a direction value of 3 and the yellow pixel a direction value of 2.

With a valid LDD map our modelling approach deviates from that of its inspiration. Instead of mapping channels and including a Strahler order, as Hans van der Kwast did, the model uses the PCRaster tool algorithm `accuflux`, which creates a map of accumulated flow using the LDD. The algorithm input requires a LDD map along with a "Material" map, which defines the additional input of material that each cell receives that is not drainage from

neighbouring pixels.

The final product, the accumulated flow map was simply used to assess the location of concentrated flow but no further thought was given to discharge rates or catchment size.

4

Results and interpretation

4.1 Hopendjupet

Hopendjupet is an approximately 200-kilometer-wide, north-northeast-southsouth-west (NNE-SSW) orientated, trough that marks the northern part of Bjørnøyrenna between two banks, Spitzbergbanken and Sentralbanken. Modern water depth values (elevation) range from 150 m.b.sl. down to more than 500 m.b.sl. at the shelf break in Bjørnøyrenna to the south (Figure 4.1). The available HMSB of Hopendjupet lies at a depth range between 142 m.b.sl. and 438 m.b.sl. (Figure 4.2) and is limited to the eastern flank of Hopendjupet.

The study area has an areal extent of 28100 square kilometers, of which only 11.15%, or 3100 square kilometers, are covered by the HMSB. The HMSB has a resolution of 8 by 8 meters and as such all values relating to the length of landforms are rounded to the nearest ten and the area of landforms is rounded to the nearest hundred. Height values are rounded to the nearest decimal place as the range resolution of the MBES exceeds 1 centimeter.

4.1.1 Negative landforms in Hopendjupet

A 179-kilometer (139 kilometers in a straight line) channel system[1] extends from shallow (169.0 m.b.sl.) seafloor in the northeastern quadrant towards deeper seafloor (397.8 m.b.sl.) in the southeastern quadrant of the study area (Figure 4.2). The depth of the negative channel imprint varies between 5 and 15 meters. The channel anabranches[2] (The Central Channel Anabranch, Figure 4.4, C and D) in the centre of the study area. South of the Central Channel Anabranch the channel system splits in twain into the Eastern Channel

1. "Channel system" is used to describe an elongate negative imprint on the seafloor, delimited by distinct slope breaks from flat to a steep (more than 10 degrees) decrease in elevation. Where a distinct slope break is not visible the extent of the channel is roughly interpolated between segments where said slope break is visible.
2. Segments, termed "branches", of the channel system diverge and converge.

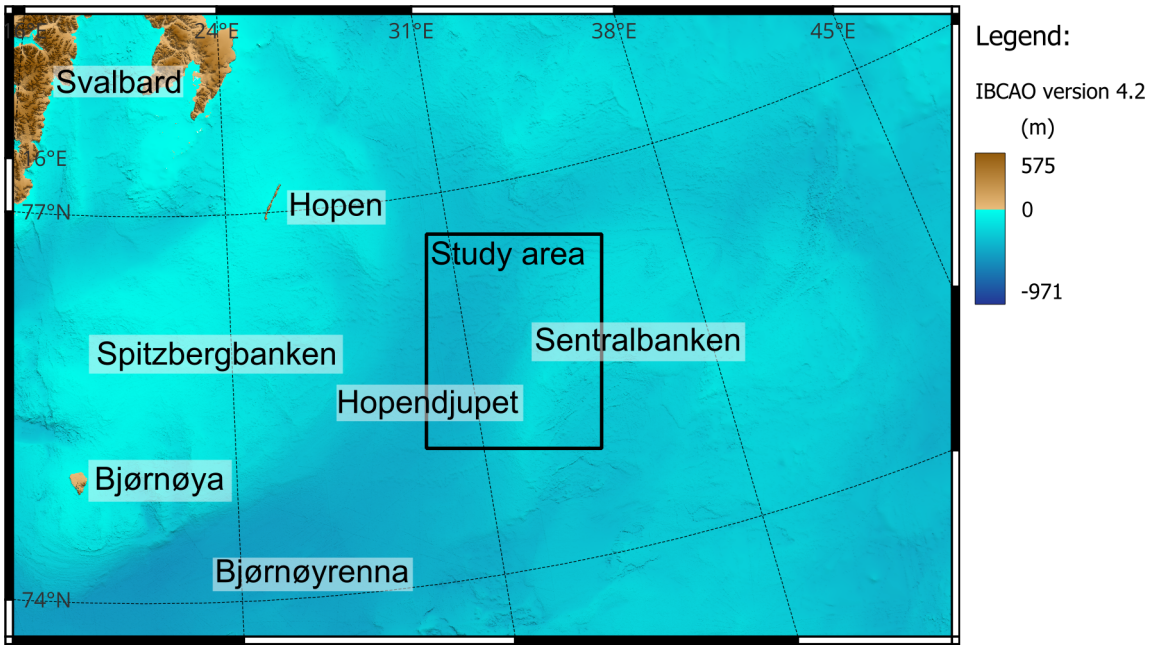

Figure 4.1: Overview of the location of the Hopendjupet study area (black rectangle) on the western flank of Sentralbanken and into Hopendjupet. Note that the color legend is in meters above sea level. Coordinates are shown in coordinate reference system (CRS) WGS 84 (EPSG:4326).

Branch and the Western Channel Branch.

North of the Central Channel Anabranch, the channel extends over a length of 84 kilometers (70 kilometers in a straight line). The width of the channel reaches as much as 2.5 kilometers although much of the lateral extent is lost due to lack of HMSB coverage (Figure 4.4, A and B). Elevation of the channel ranges from 183.0 m.b.sl. and 308.1 m.b.sl., shallowest in the north and deepening toward the south. The bed of this part of the channel system is marked by multiple positive mound-like features discussed later in this section (Figure 4.4, A1 and B1).

The Western Channel Branch is 26 kilometers long (23 kilometers in a straight line and between 150 and 1500 meters wide (Figure 4.5, A and B) and covers an elevation range of 327.8 m.b.sl. and 361.3 m.b.sl., shallowest in the north and decreasing toward the south. The southern end of the channel gradually switches to a positive landform (Figure 4.5, A1 and B1). The channel reappears 25 kilometers southwest in a 3-kilometer segment (Figure 4.5, A2 and B2) and again 15 kilometers south as a 5-kilometer segment.

The Eastern Channel Branch is 25 kilometers long (24 kilometers in a straight line) and approximately 50 to 1000 meters[3] wide (Figure 4.5, C and D) and covers a range of elevation between 282.3 m.b.sl. and 328.1 m.b.sl. (**??**). The shallowest elevation is found

3. The width of the eastern channel branch includes the space between two branches as it was not deemed feasible to find a distinct slope break between the two branches.

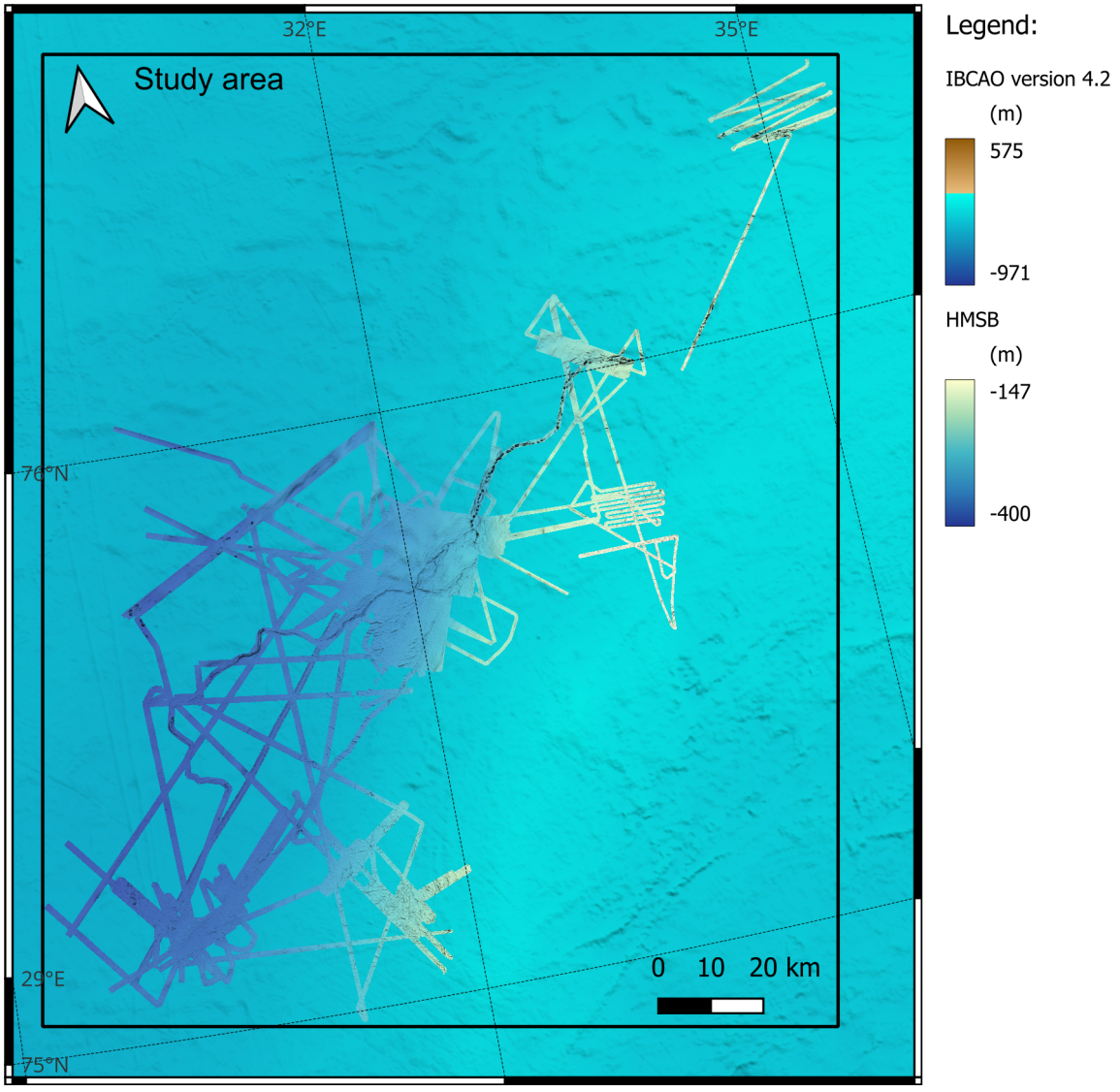

Figure 4.2: Overview of the available HMSB in the Hopendjupet study area. The HMSB color scale of the HMSB is modified by a multiplicative hillshade map set at an azimuth of 360 degrees with a Z factor (vertical exaggeration) of 25.

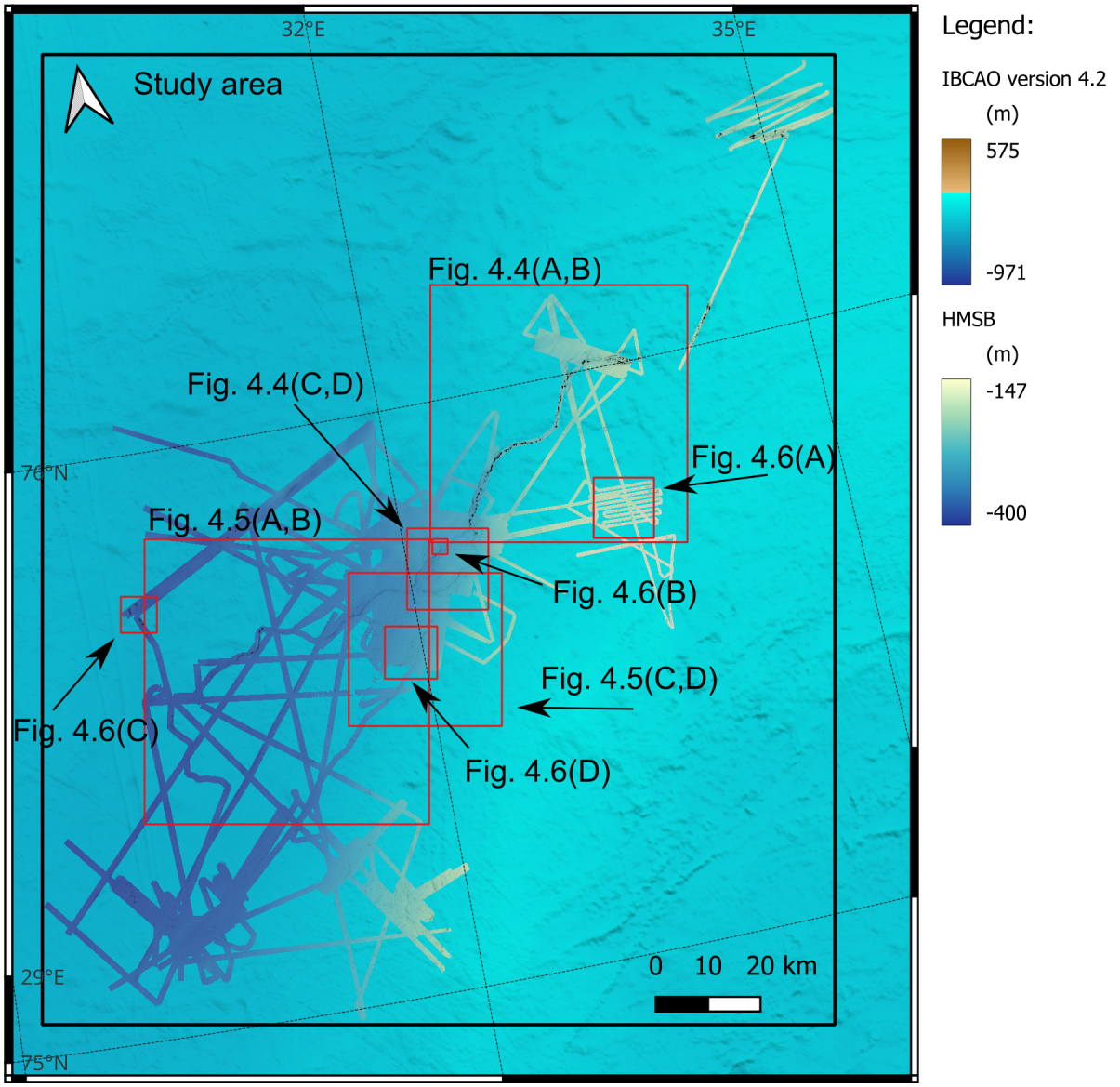

Figure 4.3: Overview of the location of figures relating to negative landforms in Hopendjupet.

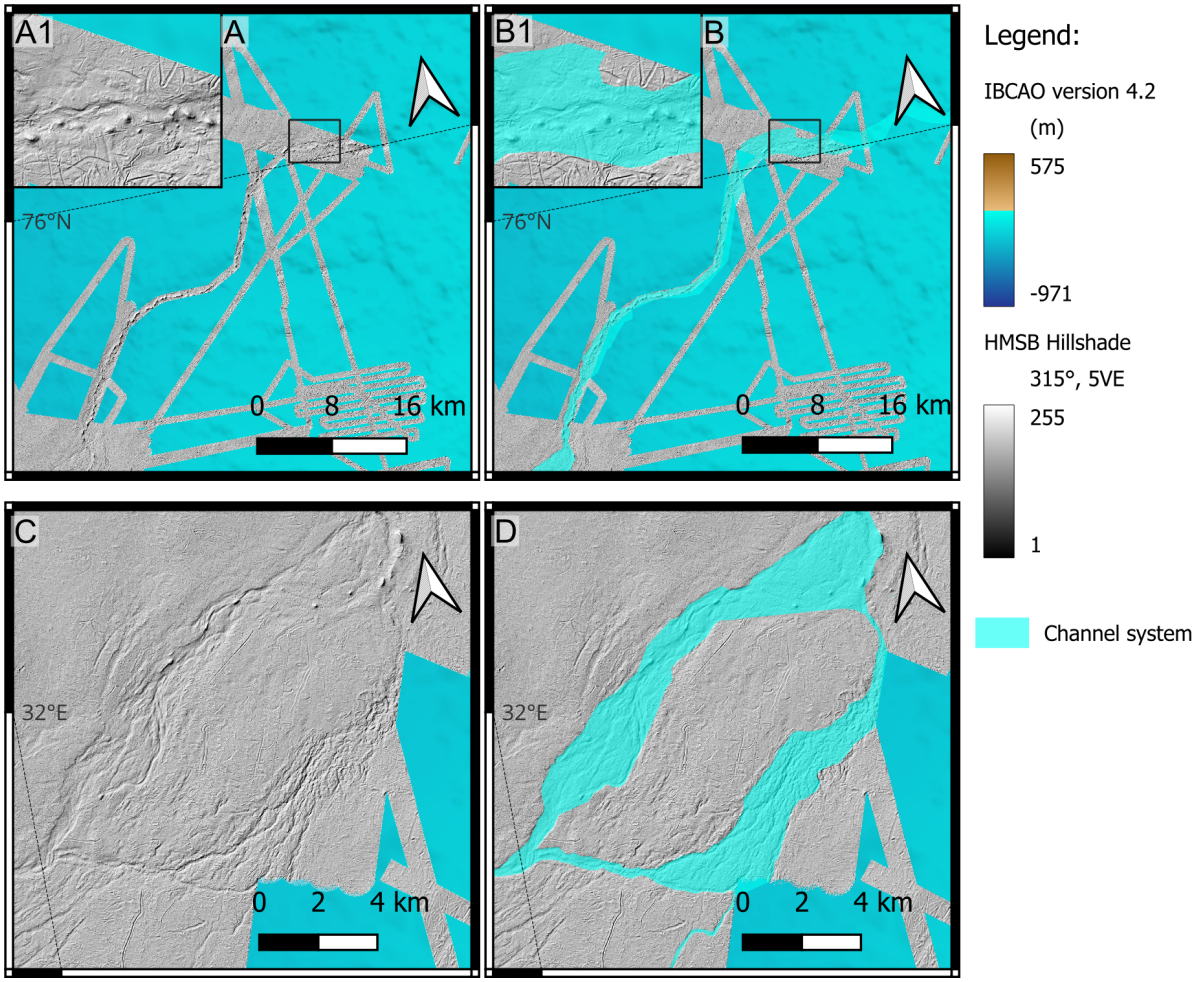

Figure 4.4: The Northern Channel Branch in the northeastern quadrant of the study area (A and B) and the Central Channel Anabranch in the centre of the study area (C and D). Figures on the left (A and C) show an uninterpreted hillshade map and figures on the right (B and D) include the mapped extent of the channels. A1 and B1 zoom in on the Northern Channel Branch to show positive features in the otherwise negative channel. The location of the figures can be found in Figure 4.3.

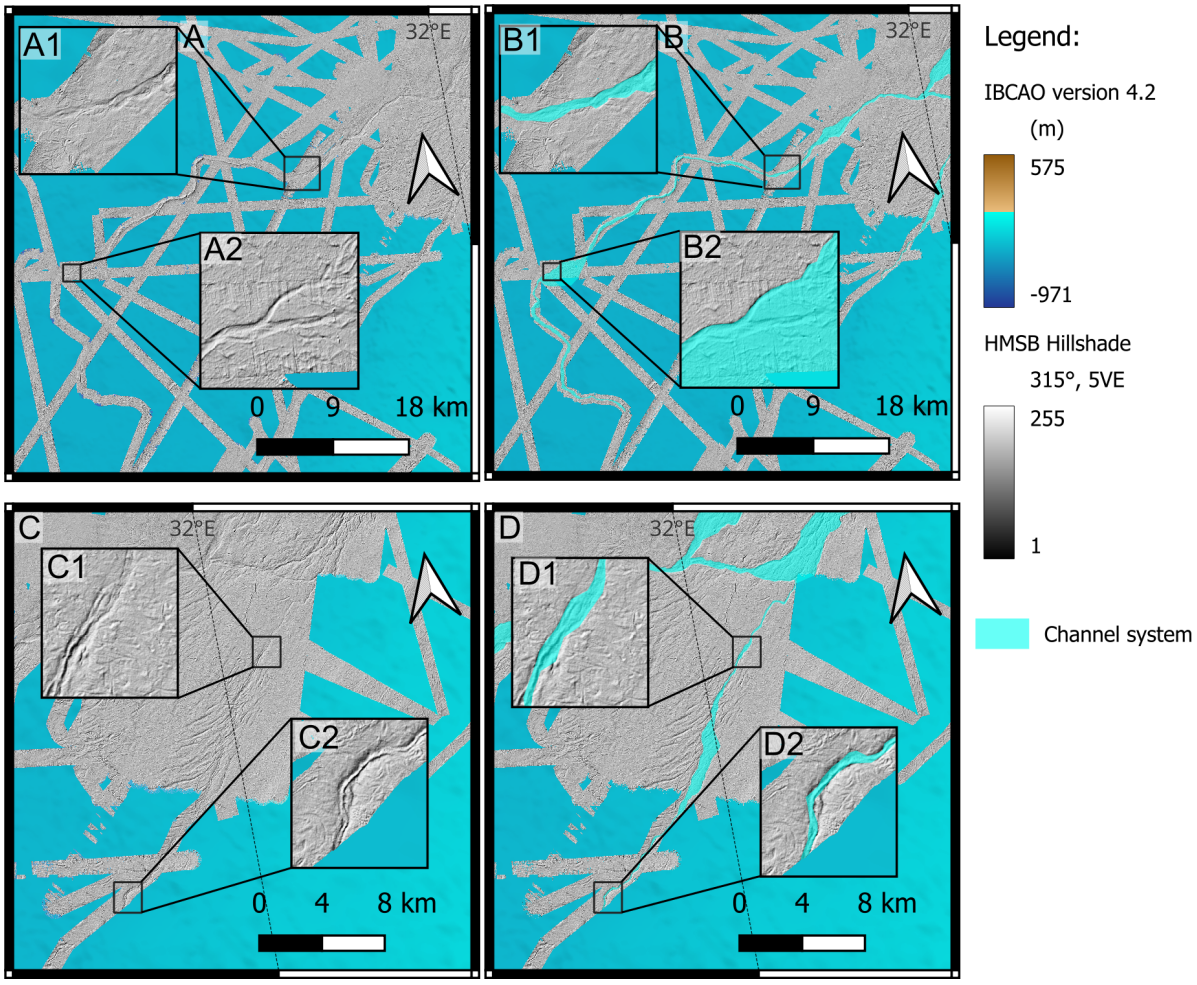

Figure 4.5: Overview of the two channel branches south of the Central Channel Anabranch, the Western Channel Branch (A and B) and the Eastern Channel Branch (C and D). Figures on the left (A and C) show an uninterpreted hillshade map and figures on the right (B and D) include the mapped extent of the channels. A1 and B1 zoom in on the gradual change from a negative to a positive expression on the seafloor. A2 and B2 show the reappearance of the negative channel to the south. C1 and D1 zoom in on the appearance of a positive ridge within the Eastern Channel Branch. C2 and D2 show the termination of the channel at the edge of the HMSB. The location of the figures can be found in Figure 4.3.

at the divergence from the Central Channel Anabranch in the north and the elevation is generally decreasing (increasing the depth) toward the south. Between 10 and 15 kilometers from the Central Channel Anabranch the channel anabranches into two segments. Roughly 5 kilometers south of the Central Channel Anabranch, the bed of the channel is characterised by a positive ridge-like landform, which will be further discussed later in this section. The southern end of the Eastern Channel Branch is lost due to lack of HMSB coverage.

East of the channel system, on depths shallower than ca. 250 m.b.sl., the seafloor is so marked by scours that no other landforms are visible (Figure 4.6, A). The scours are found throughout the study area but their intensity decreases with increasing elevation. On and west of the Central Channel Anabranch the seafloor is marked by small, meter-scale depressions that stretch north along the northeastern channel section (Figure 4.6, B).

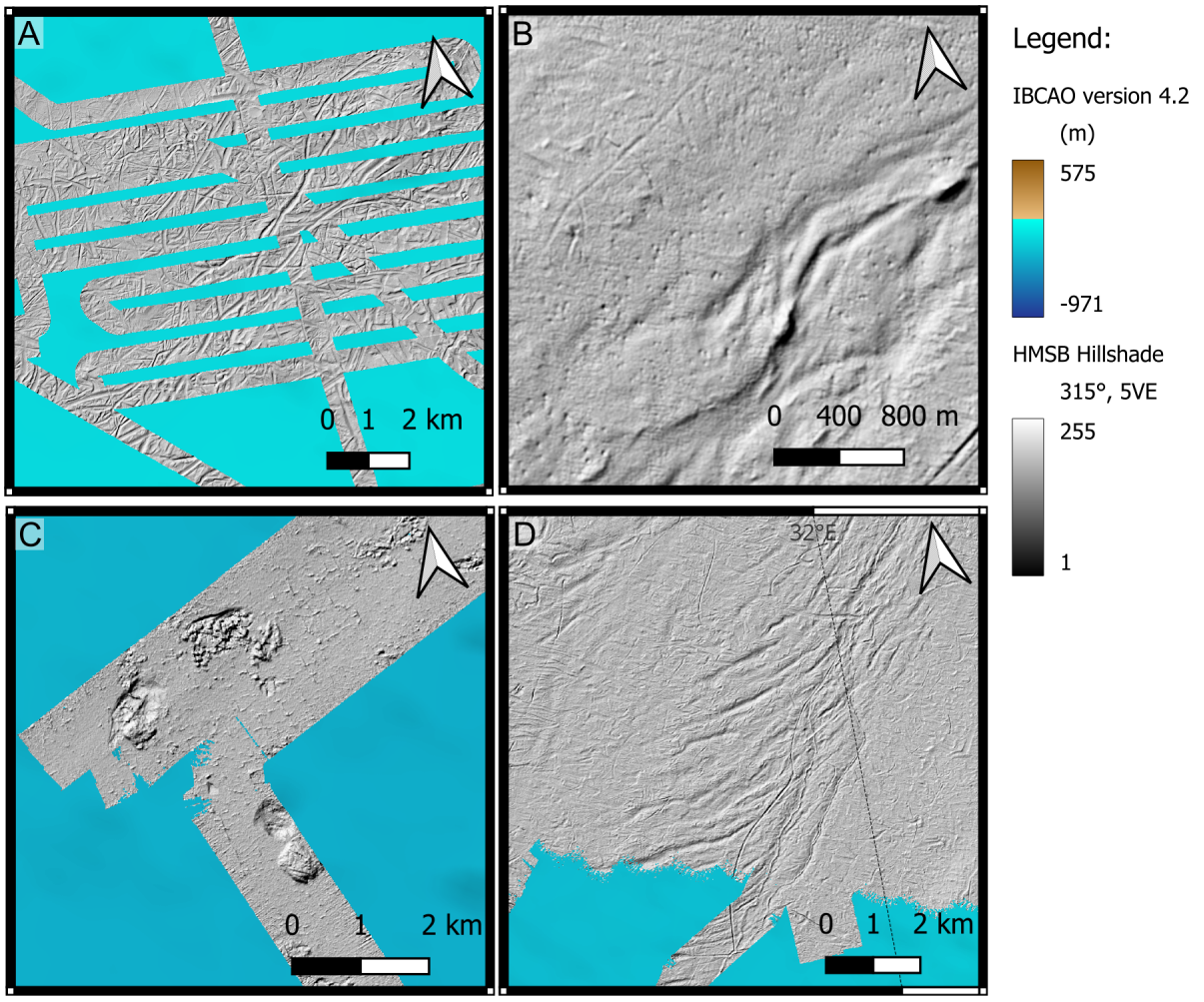

Figure 4.6: Examples of various negative landforms in Hopendjupet. A) Scour marks. B) Meter-scale circular depressions in and around a channel. C) Large circular depressions associated with a mound of similar dimensions. D) Curved parallel scours overprinted by the Eastern Channel Branch. The location of the figures can be found in Figure 4.3.

On the very western margin of the HMSB hills and holes occur in pairs or as isolated holes

(Figure 4.6, C) at water depths of 350 o 370 m.b.sl.. In the pairs, the depth of the holes roughly equals the height of the hills, and between the four mapped pairs depth and height values range between 8 and 15 meters.

South of the Central Channel Anabranch, a series of curved parallel scours mark the seafloor. The imprints are up to 6 meters deep, between 100 and 250 meters wide, and as much as 8 kilometers long (Figure 4.6, D). The depressions occur at water depths between 294 m.b.sl. and 312 m.b.sl.. The depressions all abruptly terminate at a relatively constant water depth of 312 m.b.sl.. The shape of the curved parallel scours reflects the eastern channel branch of the Central Channel Anabranch to the north. In contrast to other scours which are not overlain by any other landforms, the curved parallel scours are overprinted by the Eastern Channel Branch and the ridge within it.

4.1.2 Interpretation of negative landforms in Hopendjupet

Based on the undulating and anabranching expression of channel segments they are interpreted as erosional channels. Positive landforms found on the bed of the erosional channels (next subsection) allow for a further interpretation of the channels as subglacial drainage routes as a tunnel valley.

Scour marks found east of the tunnel valley are interpreted as iceberg scours based on their chaotic directionality and distribution limited to shallow parts of the study area.

Meter-scale depressions found around the northeastern channel section are likely unit pockmarks due to their size, shape, and distribution. For pockmarks to occur, fluids in the substrate must have been mobilised, removing sediments from the seafloor as they escape the substrate. Unit pockmarks are also limited by the sediment grain size as coarser grains require more energy to be moved. Therefore, the distribution of pockmarks is either controlled by mobile fluid distribution in the substrate or by sediment grain size.

The pairs of hills and holes on the western margin of the study area are interpreted as hill-hole pairs. In an ideal setting, the spatial orientation of hills and holes is indicative of the ice-flow direction, from the hole to the hill. Out of four mapped hill-hole pairs, the northern two are orientated from north-east to south-west, while the two southern hill-hole pairs are orientated from north-west to south-east.

Curved parallel scours are interpreted as glacial curvilineations, which are typically described as a series of parallel sinuous ridges and troughs (Clark & Livingstone, 2018). The interpretation is primarily based on the curved and parallel shape of the landform and

their reflection of the Central Channel Anabranch. While ridges have not been noted as part of the landform, it is not inconceivable that the space between negative scours is slightly elevated. The overprinting of the Eastern Channel Branch reveals that the area was covered by ice after their formation which might contribute to the lack of clear ridges in the landform.

4.1.3 Positive landforms other than potential eskers in Hopendjupet

West and south of the Central Channel Anabranch linear ridges dominate the landscape. In the case of the more prominent ridges in Figure 4.8, A, the spacing between the ridges is relatively constant between 500 and 700 meters. The relatively constant spacing holds true for line ridges throughout the study area although the spacing between parallel features slightly decreases towards the south. In the northern part of the study area, spacing between prominent ridges is between 600 and 1000 meters, whereas south of the Central Channel Anabranch, the spacing ranges from 200 to 400 meters. Around the Western Channel Branch linear ridges exhibit a staircase geometry, where smaller perpendicular ridges connect two parallel features (Figure 4.8, B). Typically, linear ridges are absent in the tunnel valley and on more prominent straight to sinuous ridges (Figure 4.8, C). In a complex multicrested section of straight to sinuous ridges the typical spatial relation is broken and linear ridges cross and are crossed by the more prominent straight to sinuous ridges (Figure 4.8, D).

The height of the linear ridges is roughly estimated (it was not measured for every mapped feature) between less than one meter and up to seven meters. The length of continuous ridge segments reaches up to 2.8 kilometers. The linear ridges are parallel to sub-parallel, orientated mostly northwest-southeast (Figure 4.9, B).

4.1.4 Interpretation positive landforms other than potential eskers in Hopendjupet

Line ridges in Hopendjupet form a geometric ridge network GRN. The relatively well-defined orientation of the GRN and primarily parallel nature (Figure 4.8) suggests that their formation is related to the retreat of an ice margin. Whether they are recessional moraines such as annual retreat moraines, crevasse-squeeze ridges, or some other ice-marginal ridge-like structure will not be determined in this study although it is thought likely that the relatively equal spacing of prominent ridges is related to variations in ice-margin retreat velocities.

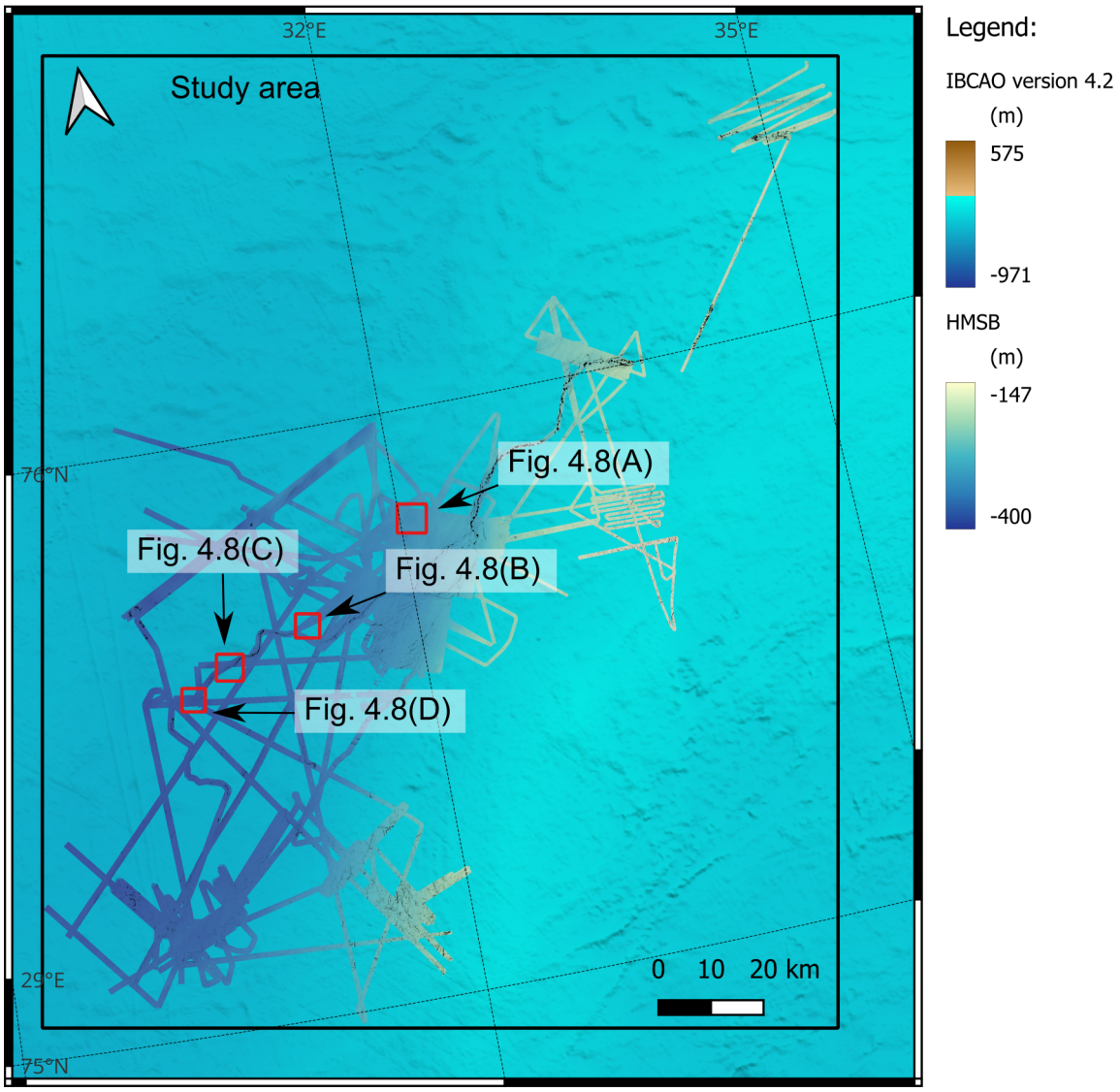

Figure 4.7: Overview of the location of figures of non-esker type positive landforms

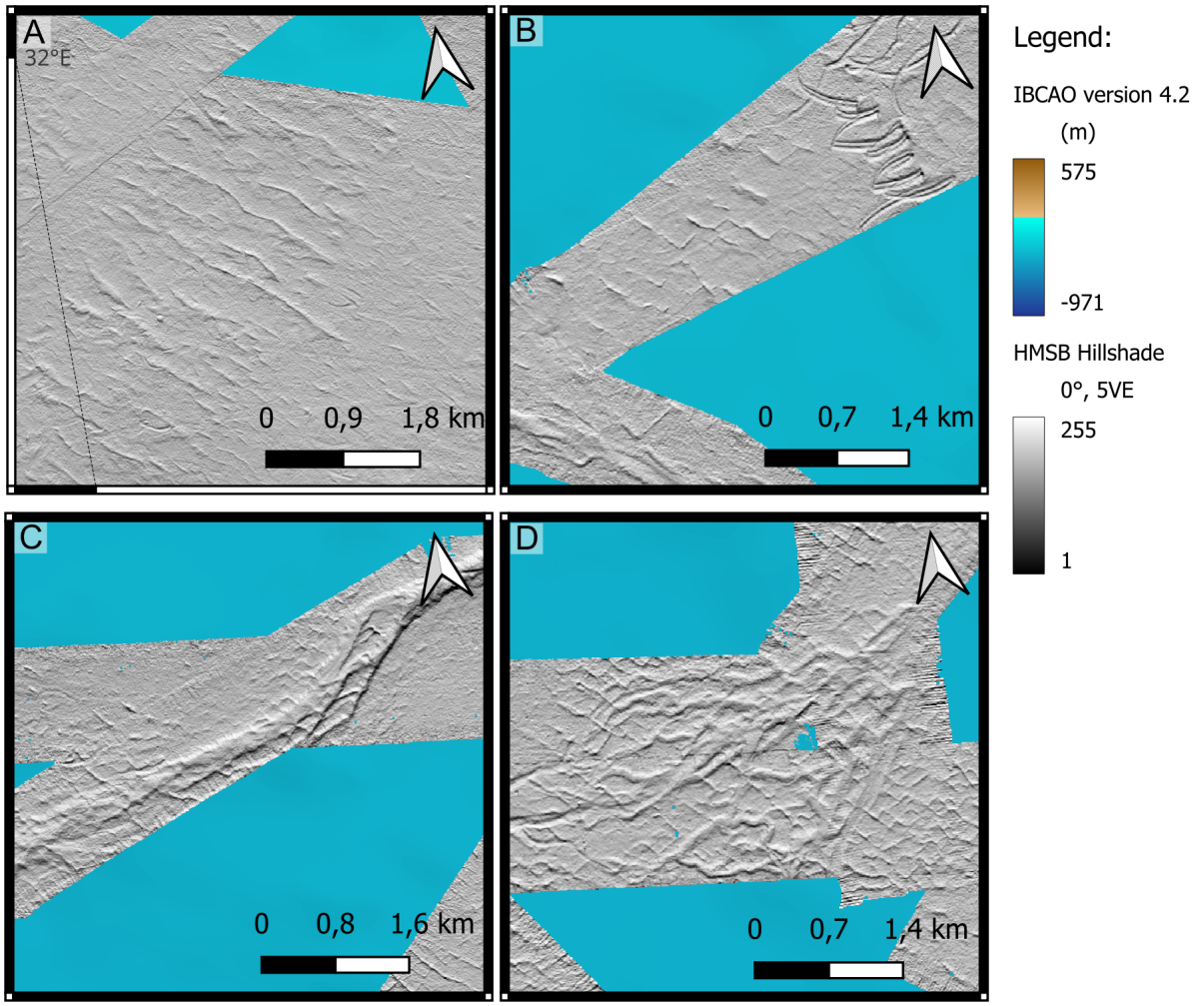

Figure 4.8: Examples of linear ridges in Hopendjupet. A) Typical parallel ridges of semi-regular spacing. B) Linear ridges exhibiting staircase geometry. C) Typical spatial relation of linear ridges and straight to sinuous ridges, where linear ridges are absent on the larger straight to sinuous ridge. D) Atypical overprinting of linear ridges on a complex multicrested straight to sinuous ridge segment. The location of the figures can be seen in Figure 4.7.

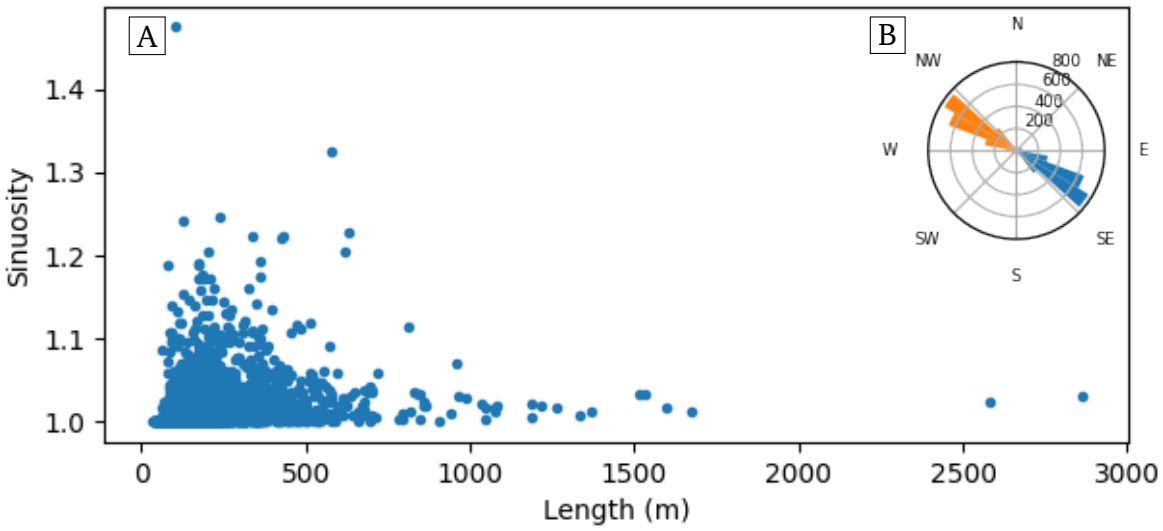

Figure 4.9: A) Length vs. sinuosity of linear ridges in Hopendjupet. B) Frequency distribution of the orientation of linear ridges.

4.1.5 The Hopendjupet ridge and mound chain

A series of ridges and mounds characterise the channel bed of the Northern Channel Branch and into the Central Channel Anabranch (Figure 4.4, A1). Water depth in this section of the study area is between 315 m.b.sl. and 200 m.b.sl., increasing in depth toward the south. The ridges and mounds appear as round to slightly elongated (elongation ratio of up to 6.1) segments that are aligned to form a continuous system over a distance of 72 kilometers. Unfortunately, the lateral extent of both the mounds and the channel in which they are found is not clear in this area as HMSB coverage is lacking. At least one mound is found on a nearby swath line (to the east) that could be related to a channel branch, however, the area is heavily scoured.

The distribution of mounds coincides with unit pockmarks on the seafloor although the pockmarks are not found on the mounds. In cross-section, the crest of the mounds is either flat-crested, round-crested or sharp-crested. The mounds are mostly isolated from each other although two adjacent mounds can be connected by slightly elevated seafloor.

A total of 158 features were mapped as the ridge and mound chain in Hopendjupet, of which 29 have an elongation of more than two, and are thus classified as ridge segments, while the remaining 129 have an elongation ratio of less than or equal to two, and are thus classified as mounds. The cumulative length of all features that comprise the mound chain is 46 kilometer (km) or around 64% of the total length it covers. Table 4.1 summarises general attribute statistics of ridges and mounds in the mound chain in Hopendjupet.

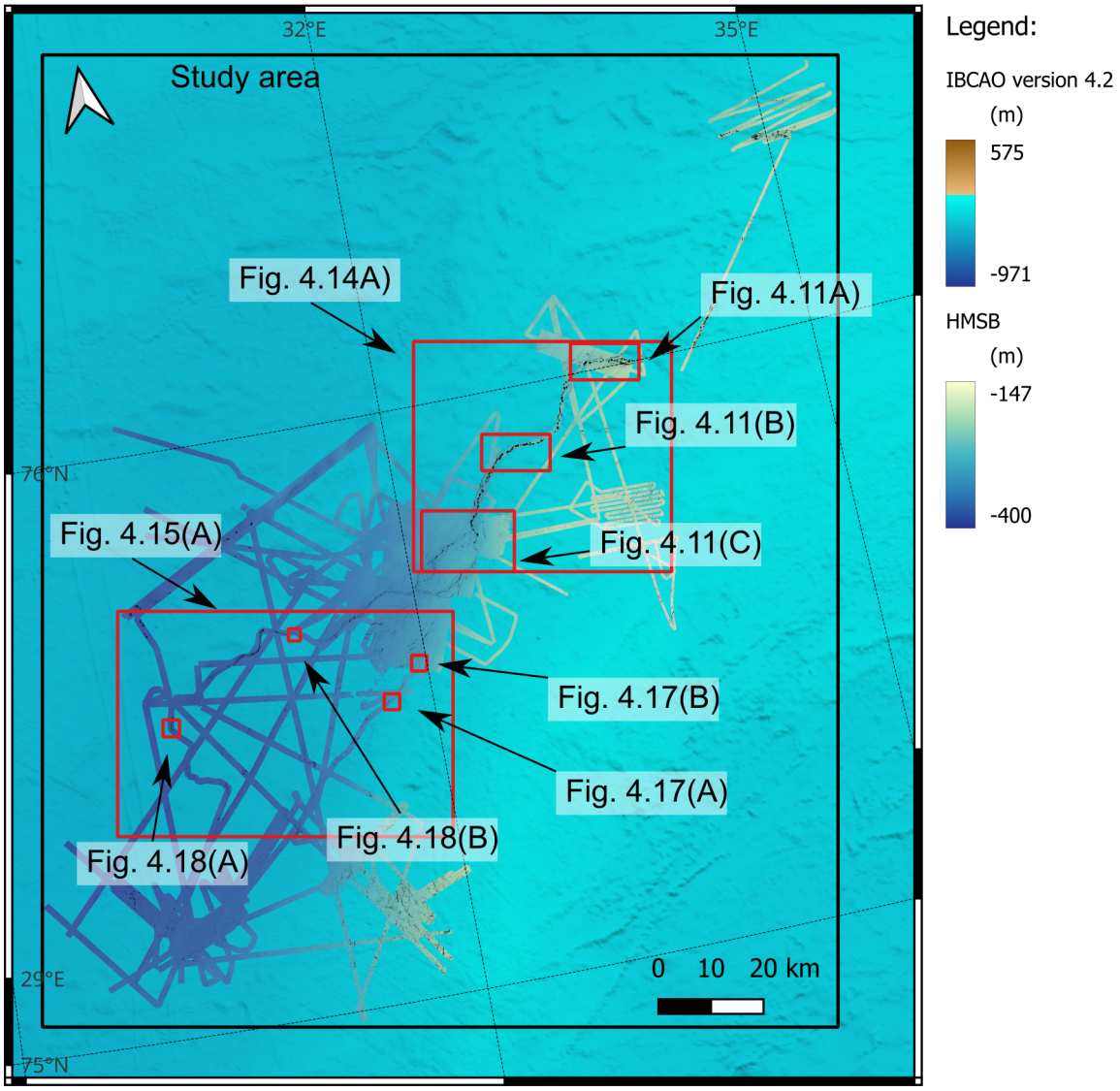

Figure 4.10: Overview of the location of figures of potential esker-type positive landforms.

Table 4.1: General attribute statistics of 158 ridges and mounds in the Hopendjupet mound chain.

Attribute	Minimum	Maximum	Average	Standard deviation
Length (m)	60	740	290	140
Area (m^2)	2,700	167,900	45,600	37,800
Height (max.)	2.7	50.6	18.3	10.1
Height (avg.)	1.7	26.4	10.6	6.0
Height (std.)	0.5	16.2	5.9	3.1
Width (max. height)	40	340	180	80
Width (avg.)	30	290	130	60
Width (std.)	0	110	50	30
Sinuosity (only ridges)	1.01	1.15	1.04	0.03

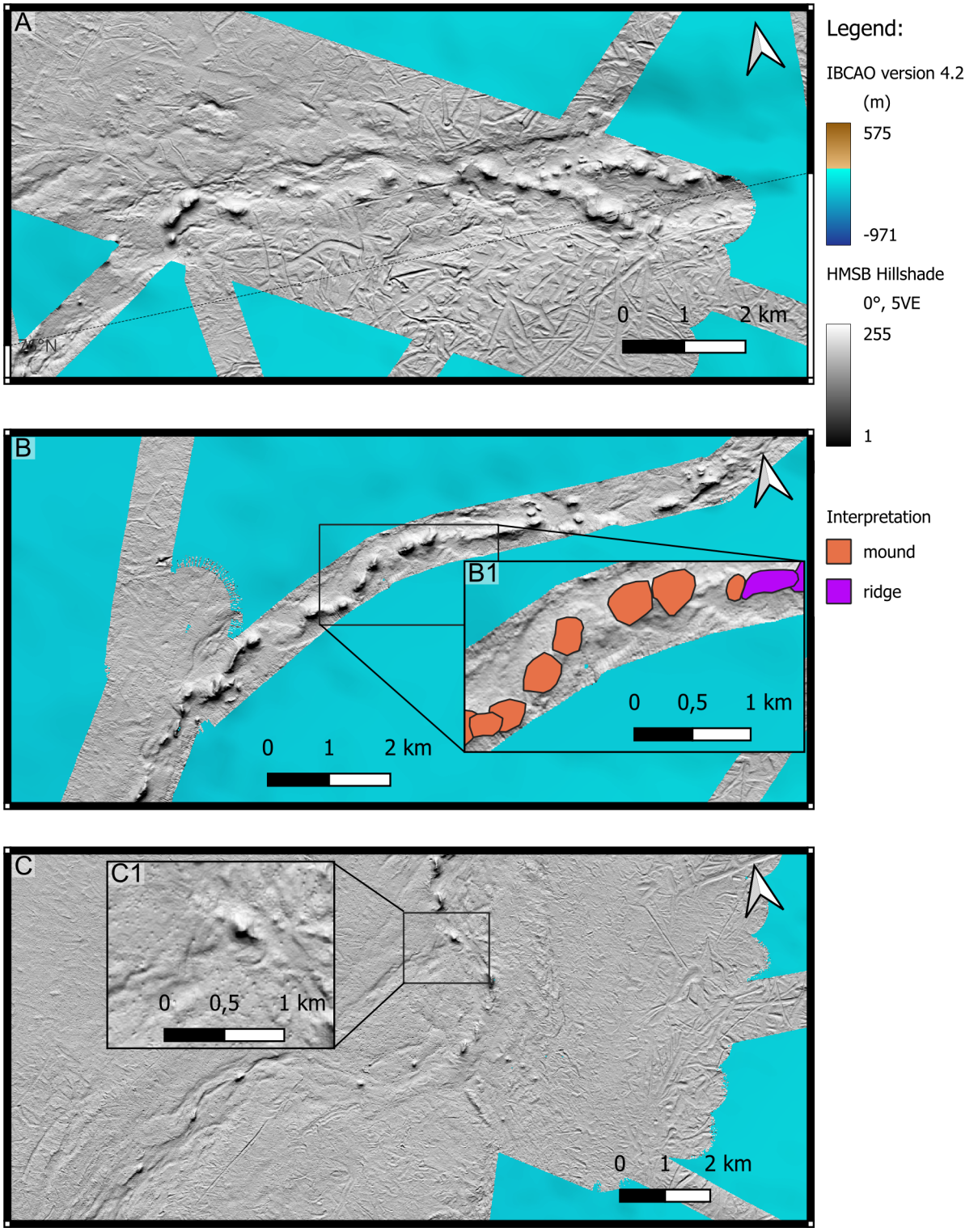

Figure 4.11: The Hopendjupet ridge and mound chain. A: The northern part of the chain. B: The central part of the chain and an example of the visual mapping (B1). C: The southern part of the chain extends into the Central Channel Anabranch. C1: Example of pockmarks found around the ridge and mound chain. The location of the figures can be seen in Figure 4.10.

The width of both ridges and mounds is consistently in the region of 10 times greater than the height, varying from 22 down to 5 times wider than their height. (Figure 4.12). The volume of sediments within mounds and ridges is roughly estimated to be between four thousand cubic meters and four million cubic meters of individual features and a total of 100 million cubic meters for the entire chain.

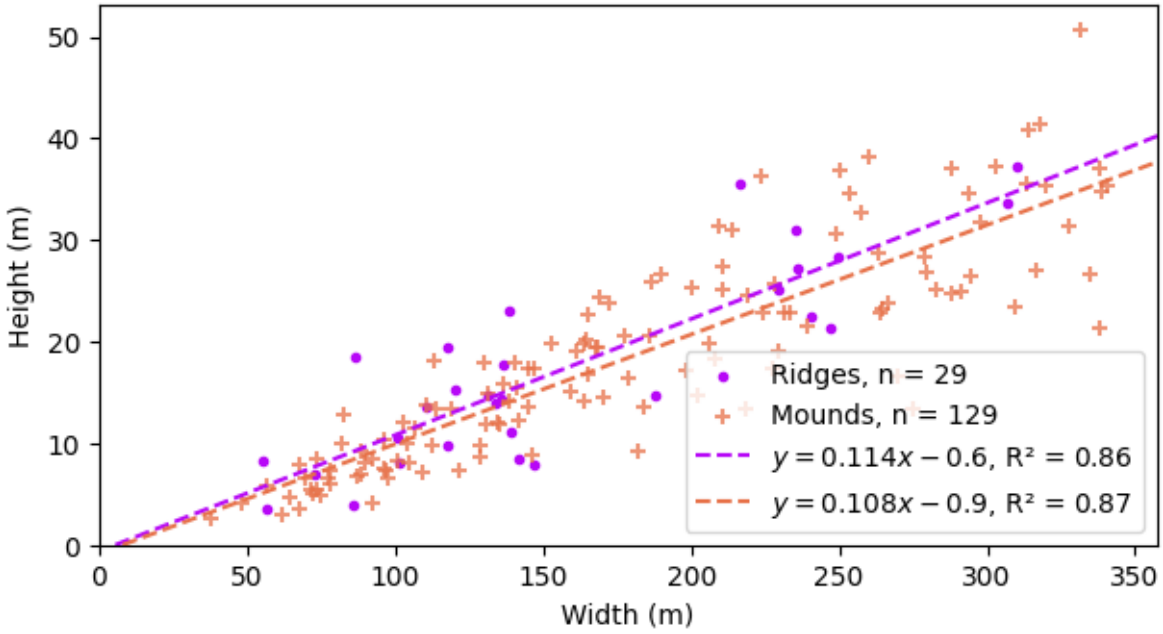

Figure 4.12: Height vs. width of ridges and mounds in the Hopendjupet ridge and mound chain.

Out of 29 ridges in the Hopendjupet ridge and mound chain, 27 are straight and 2 are slightly sinuous. The length of the ridges does not seem to affect the sinuosity (Figure 4.13, A). The orientation of ridges in the ridge and mound chain is grouped into two primary orientations, NNE-SSW and east-northeast-west-southwest (ENE-WSW) while the main angle of orientation of the combined centerlines over the entire chain is northeast-southwest (Figure 4.13, B).

Connecting the gaps between ridges and mounds reveals a highly sinuous (sinuosity of 1.31) system (Figure 4.14, A) where positive landforms occur at a semi-regular interval. Features occur at intervals of 138 meters to 2760 meters where closely spaced features tend to overlap. A rolling average of the interval shows a rapid decrease in spacing (from 1600 meters down to 560 meters) from the southwest to the northeast over the first 28 kilometers (Figure 4.14, B). The initial decrease in spacing is followed by a gradual increase (from 560 to 972 meters) between 28 and 47 kilometers, although a 5-kilometer section exhibits tight spacing (430 meters rolling average) of low relief features (less than 10 meters high). From 47 kilometers from the start in the southwest, the spacing decreases from 972 meters and down to a minimum of 417 meters.

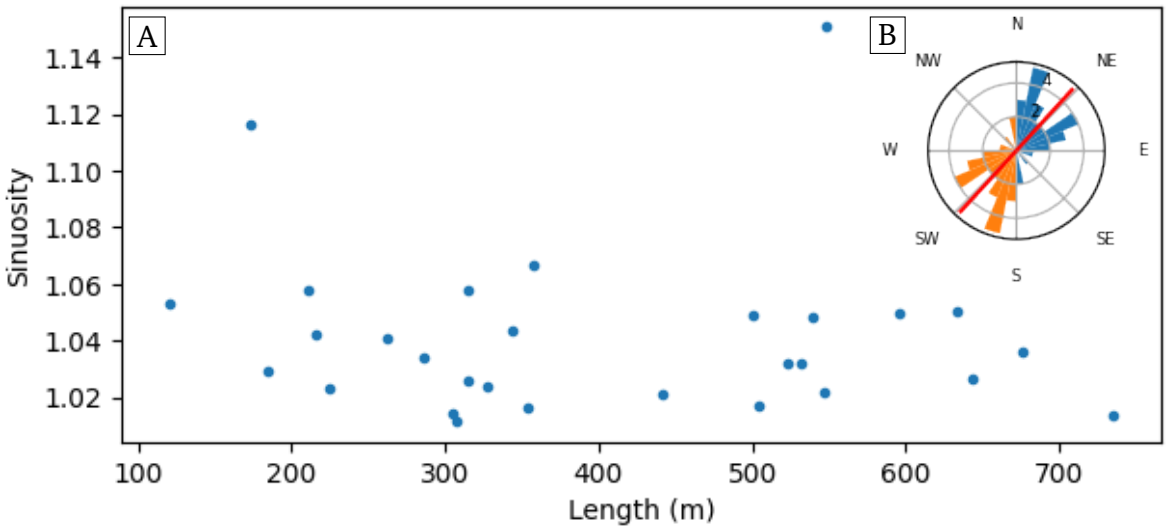

Figure 4.13: A: Length vs. sinuosity of ridges in the Hopendjupet ridge and mound chain. B: Frequency distribution of the orientation of ridges in the Hopendjupet ridge and mound chain, blue and orange bins are mirrored around the center of the plot, and the red line shows the main angle of orientation of the interpolated centerline for the entire chain.

4.1.6 Interpretation of the Hopendjupet ridge and mound chain

There are clear indicators for a glaciofluvial origin of the Hopendjupet ridge and mound chain, the primary of which is the consistent distribution in a subglacial meltwater channel incision. Numerous ridges and mounds are aligned into a highly sinuous collection that is interpreted as a beaded esker system, hereafter referred to as the EB. The system occurs in the shallower part of the study area, however, the true extent of the system is unknown due to lack of HMSB coverage and abundant iceberg scouring. Unit pockmarks occur around the esker bead system hinting at soft sediments characterising the area.

4.1.7 Hopendjupet straight to sinuous ridges

Straight to sinuous positive ridges are found overprinting or as continuations of both branches of the tunnel valley south of the Central Channel Anabranch. Ridges that occur in connection to the Eastern Channel Branch are hereafter referred to as the Eastern Ridge Segments (ERS). Ridges that occur in connection to the Western Channel Branch are referred to as the Western Ridge Segments (WRS) (Figure 4.15). The two straight to sinuous ridge systems vary in size. The ERS is much smaller, mainly in width but also in height, compared to the WRS. The ERS shows a good correlation of height vs. width where the ridges are approximately 17 times wider than they are high. The WRS exhibits greater variations in height vs. width (R-squared of 0.37 compared to 0.62 for the ERS), but a best

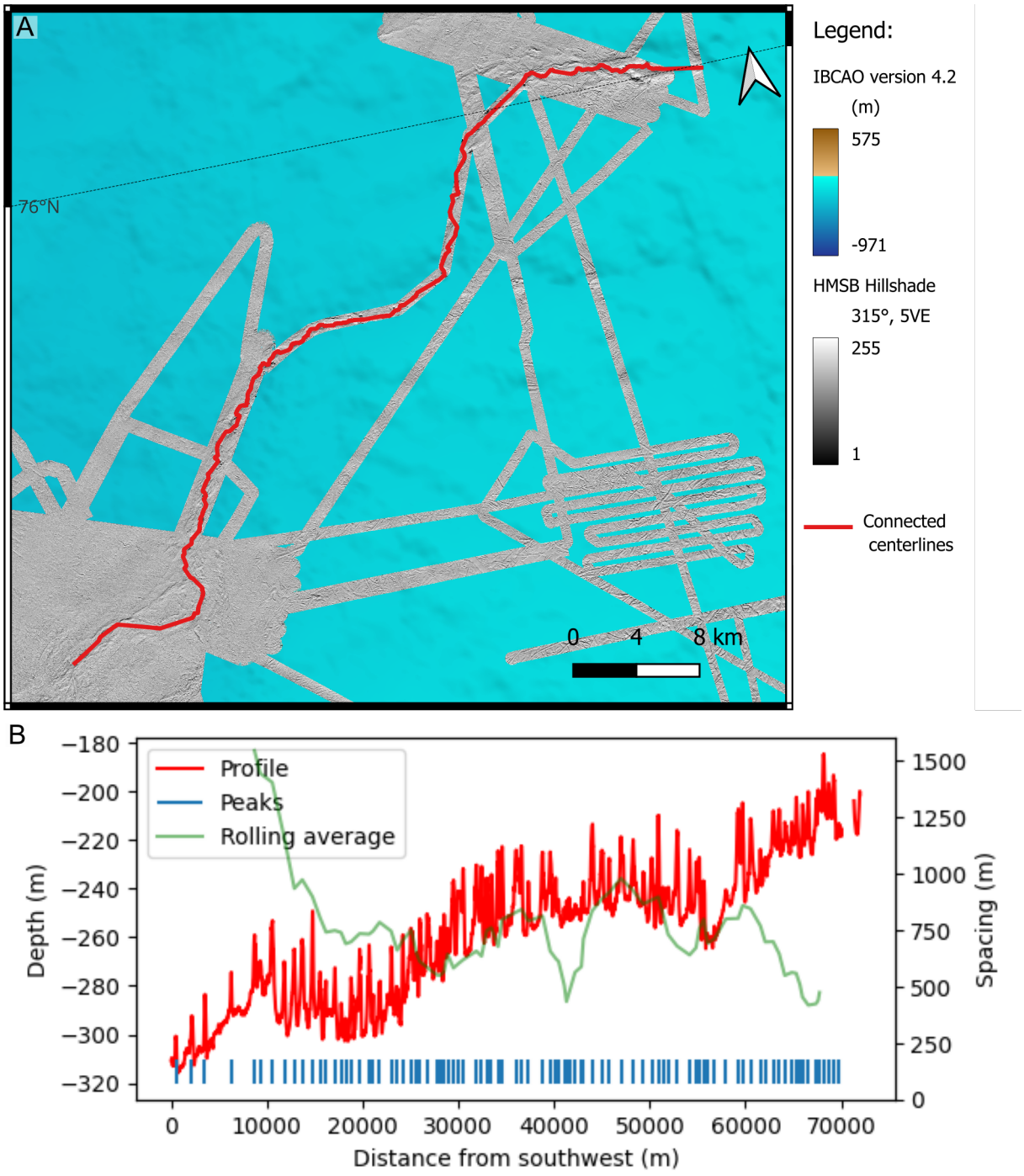

Figure 4.14: A: The alignment of ridges and mounds in the Hopendjupet ridge and mound chain. B: An elevation profile (on the depth axis) across the entire length of the Hopendjupet ridge and mound chain from the southwest (at 0 meters) toward the northeast. Peaks in the profile indicate ridges or mounds and a blue vertical line is placed at the bottom of the plot for each peak. The rolling average spacing of 9 features is shown in green (on the spacing axis) The location of the figure can be seen in Figure 4.10..

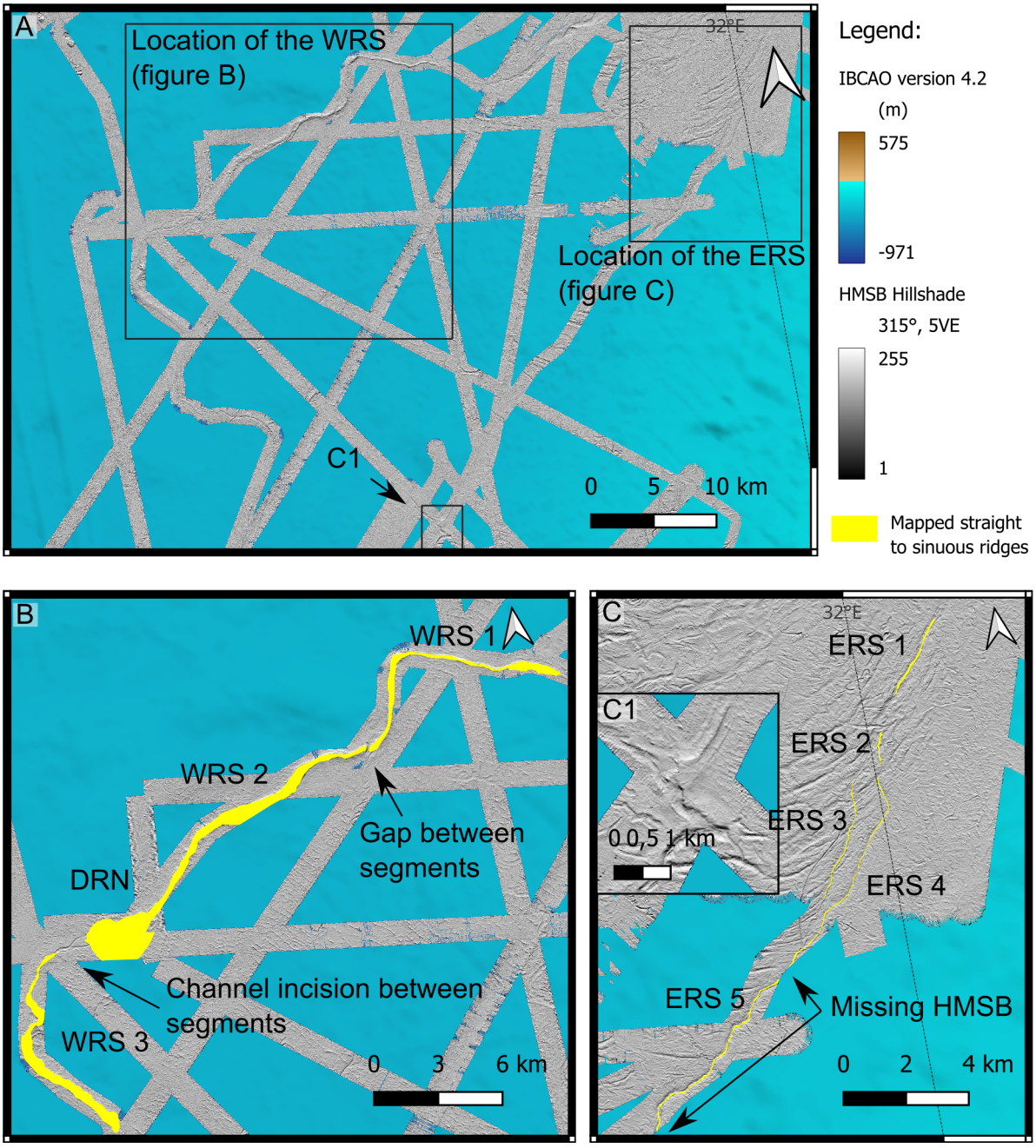

Figure 4.15: A: Location of mapped straight to sinuous ridges south of the Central Channel Anabranch. B: Features comprising the WRS, WRS 1-3 and the DRN. C: Features comprising the Eastern Ridge Segments (ERS), ERS 1-5 and a feature potentially connected to the system 28 kilometers southwest. The location of the figures can be seen in Figure 4.10.

linear fit results in a width 125 times that of the height (Figure 4.16).

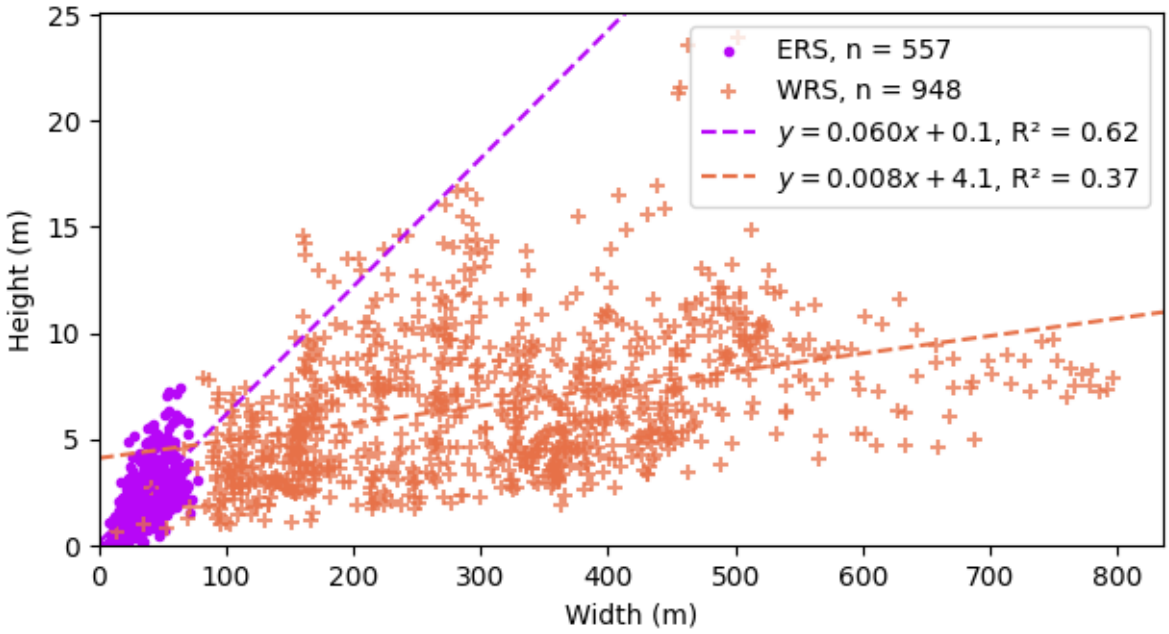

Figure 4.16: Height vs. width of straight to sinuous ridges in Hopendjupet.

The ERS is composed of five mapped segments, marked ERS 1 through 5 (Figure 4.15, C), that vary in length between 1170 meters and 7190 meters (Table 4.2). The true continuity of the system is underrepresented as the two longest ridge segments, ERS 4 and 5, are separated by a lack of HMSB coverage and so is the southern end of the system. Shorter segments of the ERS are found in shallower water depths to the north (ERS 1-3), where iceberg scouring is more abundant. The height and width of the segments are close to being undetectable due to limited resolution, with the average width being between 30 and 50 meters (3 and 6 pixels respectively) and the average height of between 1.7 and 3.2 meters. Segments of the ERS appear sharp- to round-crested in cross-section but this might be caused by low resolution (Figure 4.17).

The segments are all straight except for ERS 5, which just falls under the category of slightly sinuous. 28 kilometers south-southwest of the ERS there is potentially an 8-kilometer long ridge segment that could belong to the same system which ends, to the south, in a 10-meter high flat-topped mound-like structure (Figure 4.15, C1).

Around 24 kilometers southwest of the central convergence, the channel gradually switches from a negative channel imprint to a positive ridge (Figure 4.18, B), the WRS, over a distance of ca. two kilometers. The WRS is composed of three distinct positive ridges and one distributary network of ridges Distributary Ridge Network (DRN) (not included in Table 4.2). The WRS exceeds the ERS in all possible metrics, segments are longer, more

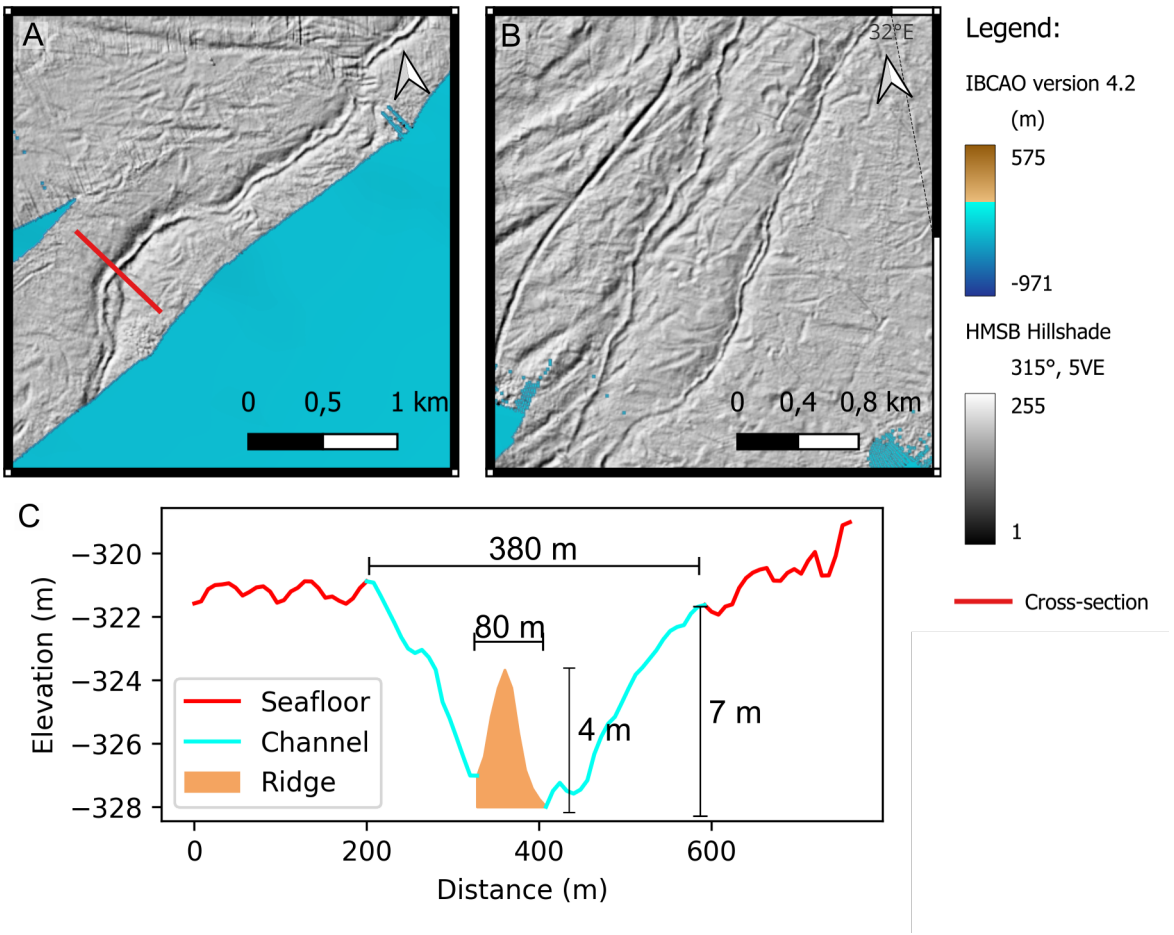

Figure 4.17: Two handpicked examples of the ERS. A: ERS 5 at the southern extent of the system. B: ERS 3 and 4 in two parallel branches of the Eastern Channel Branch overprinting glacial curvilineations. C: Typical cross-section of the ERS on ERS 5. The crest of the ridge appears to be sharp-crested but due to the limited resolution, it is represented by only three elevation points. Note that both the ridge and the channel are wider in cross-section than based on visual mapping on a slope map filtered to 5 degrees. The location of the figures can be seen in Figure 4.10.

Table 4.2: Statistical attributes of positive ridges in the ERS and the WRS.

Ridge	Length	Sinuosity	Height (m)			Width (m)			Area
	(m)		max.	avg.	std.	max. height	avg.	std.	(km^2)
ERS 1	2,810	1.01	7.2	3.2	1.6	50	50	10	0.15
ERS 2	1,170	1.06	6.3	2.3	1.5	50	40	20	0.05
ERS 3	5,890	1.05	5.5	1.8	1.0	40	30	20	0.19
ERS 4	7,190	1.09	4.9	1.7	1.0	60	30	10	0.21
ERS 5	6,880	1.10	7.4	2.8	1.4	60	40	10	0.27
WRS 1	12,710	1.31	16.8	6.5	3.2	290	220	100	2.77
WRS 2	13,750	1.07	15.5	7.2	3.1	290	360	160	5.02
WRS 3	11,460	1.29	23.9	6.1	3.7	500	350	150	4.02

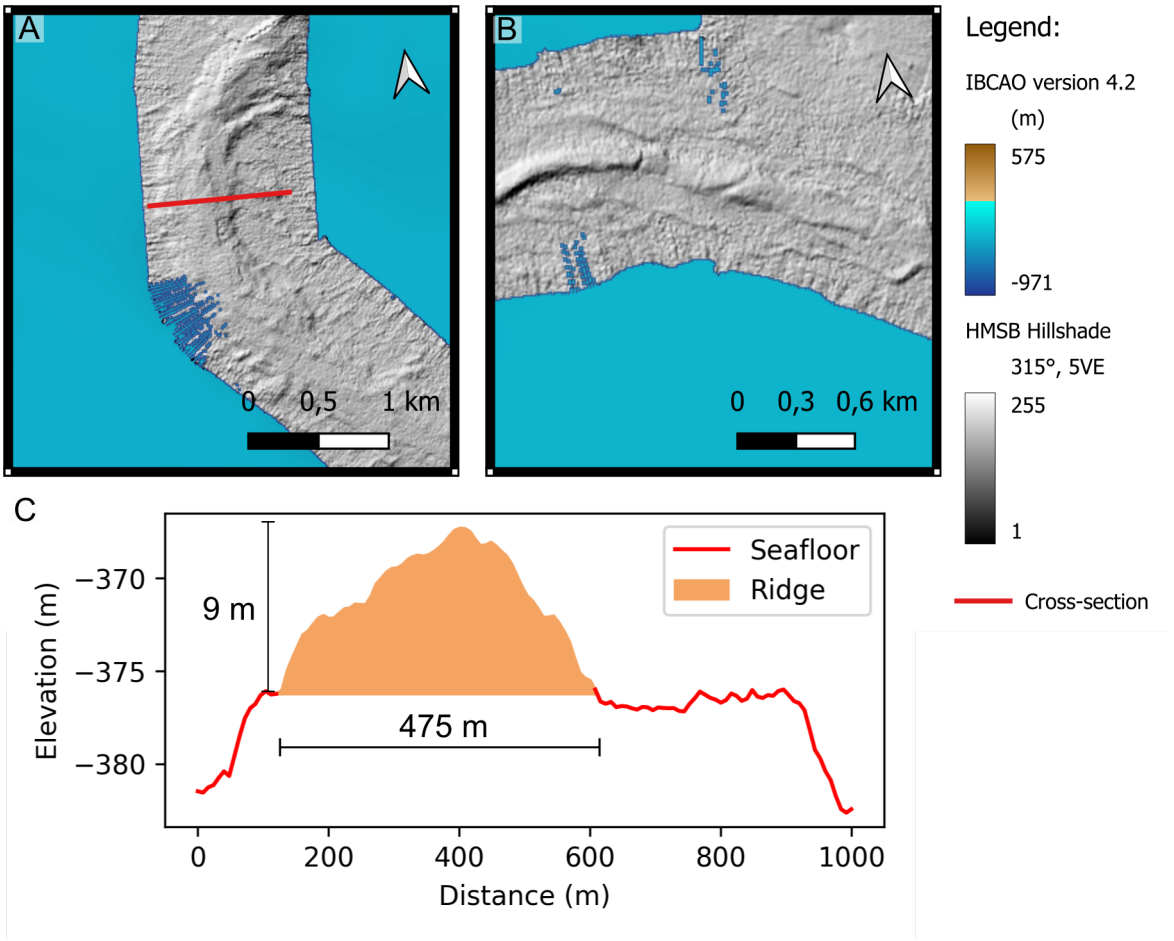

Figure 4.18: Two handpicked examples of the WRS. A: WRS 3 at the southern end of the system. B: WRS 1 at the northern end of the system showing a gradual change from the negative channel to a positive ridge. C: Cross-section of WRS 3. The cross-section is said to exhibit a flat top due to the large vertical exaggeration of 45. The edges of the cross-section trend downward but they occur at the edges of the HMSB. The location of the figures can be seen in Figure 4.10.

sinuous, higher, and wider (Figure 4.18, C and Table 4.2). The two northernmost segments of the WRS, WRS 1 and 2, are separated by a small offset, which could potentially be an iceberg scour. WRS 2 gradually lowers towards the south before switching to a diverging or distributary multi-crested network of ridges, DRN. The DRN abruptly changes into a converging channel network at its southern end which gradually switches back to a ridge (WRS 3).

From north to south, ridges in the WRS widen, a fact that is somewhat misrepresented in Table 4.2 as WRS 3 includes the relatively narrow change from channel to ridge, while the average height remains roughly the same, give or take one meter.

4.1.8 Interpretation of Hopendjupet straight to sinuous ridges

The location of straight to sinuous ridges inside and as direct continuations of tunnel channels in Hopendjupet suggests that they are esker ridges. The ERS are relatively continuous in height and width along their lengths, which indicates steady flow conditions during their formation or, potentially, synchronous formation along the entire length of the ERS. Assuming that the flat-topped mound south of the ERS does belong to the same drainage system, it might represent an esker delta where the drainage system exited the ice margin. As the esker system is fully distributed within an erosional channel, it is interpreted as an esker conduit.

The WRS vary greatly along their length, going as far as changing from a single crested ridge to a distributary multi-crested segment, which, along with the gradual change from an erosional channel to a ridge suggests that they are formed time-transgressively under changing flow conditions. The width of the esker exceeds that of the erosional channel which it stems from, as such, coupled with the high width-to-height ratio, it is interpreted as an esker enlargement formed time-transgressively by deltaic deposition at the ice margin.

4.1.9 Hopendjupet interpretation (Figure 4.19)

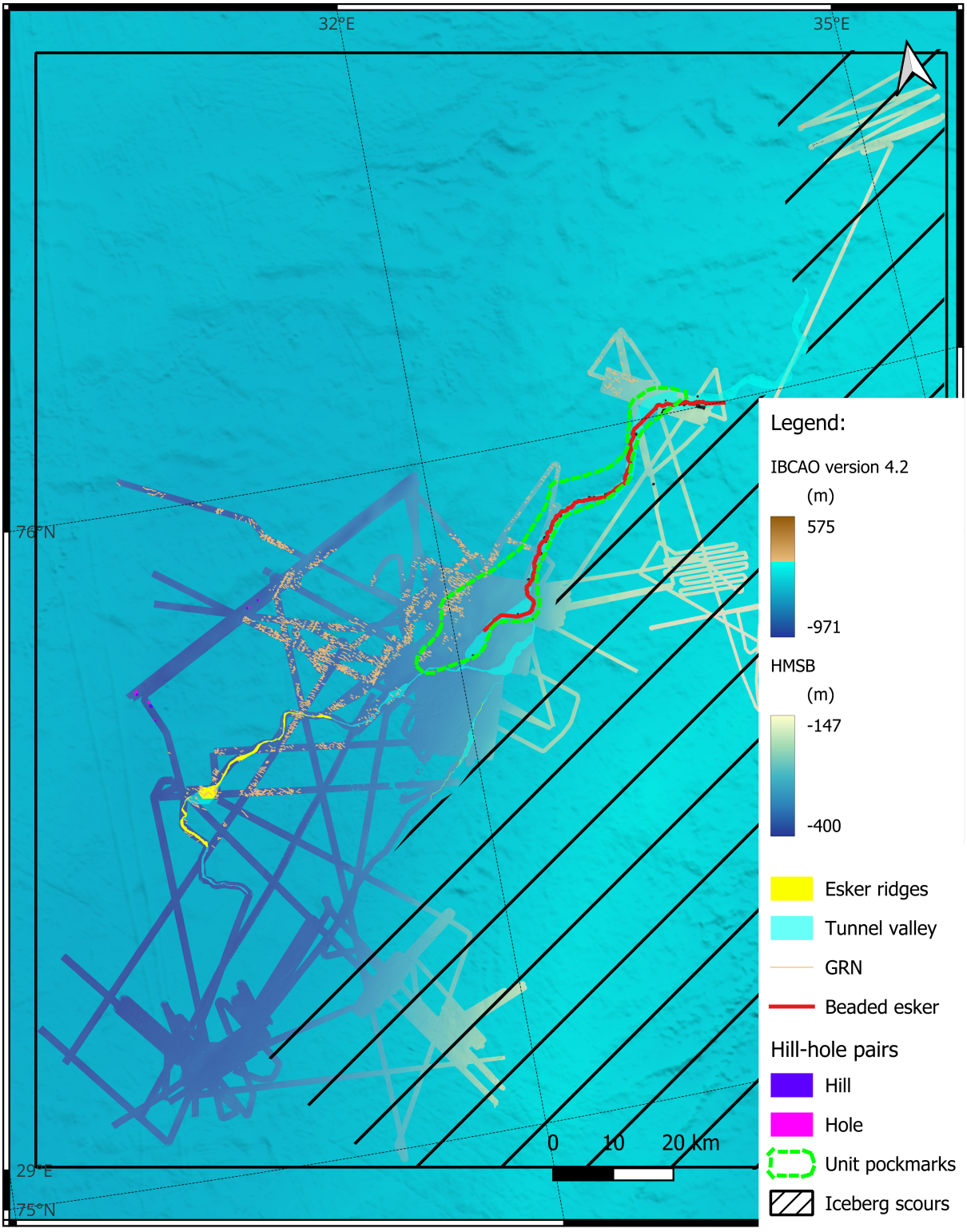

Figure 4.19: All mapped features in Hopendjupet and their interpretation.

4.2 Hoburgs Bank

Hoburgs Bank is a broad, approximately 470 kilometers wide and 700 kilometers long, shallow bank area with water depths ranging from 63 to 10 m.b.sl. (depth values are derived from the HMSB). The bank is flanked by two NNE-SSW orientated troughs, the East Gotland Basin and the West Gotland Basin, to the east and the west respectively. The West Gotland Basin is significantly deeper, up to 240 m.b.sl. compared to 110 m.b.sl. in East Gotland Basin. Both troughs are deepest toward the north (Figure 4.20.)

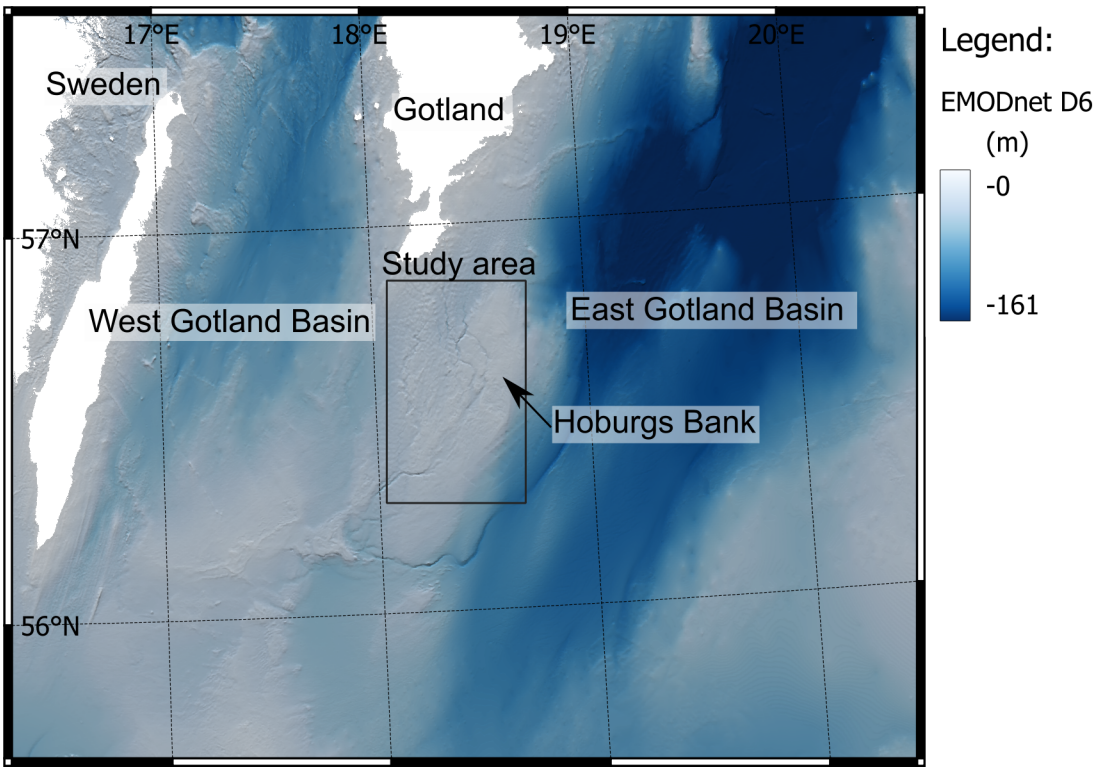

Figure 4.20: overview of the location of the Hoburgs Bank study area (black rectangle) south of the island of Gotland in the Baltic Sea. Coordinates are shown in CRS WGS 84 (EPSG:4326).

The study area has an areal extent of 2561 square kilometers, of which 52.74% are covered by the HMSB, or 1351 square kilometers (Figure 4.21). The HMSB has a resolution of 1 by 1 meter and as such the length and area of landforms are rounded to the nearest full number. Height values are rounded to the nearest decimal place as the range resolution of the MBES exceeds 26 millimeters.

4.2.1 Negative landforms on Hoburgs Bank

The general bathymetry of Hoburgs Bank is characterised by an extensive channel network that extends beyond the available HMSB. The channel network originates north of the Hoburgs Bank HMSB, with at least five channel branches, four of which enter the HMSB

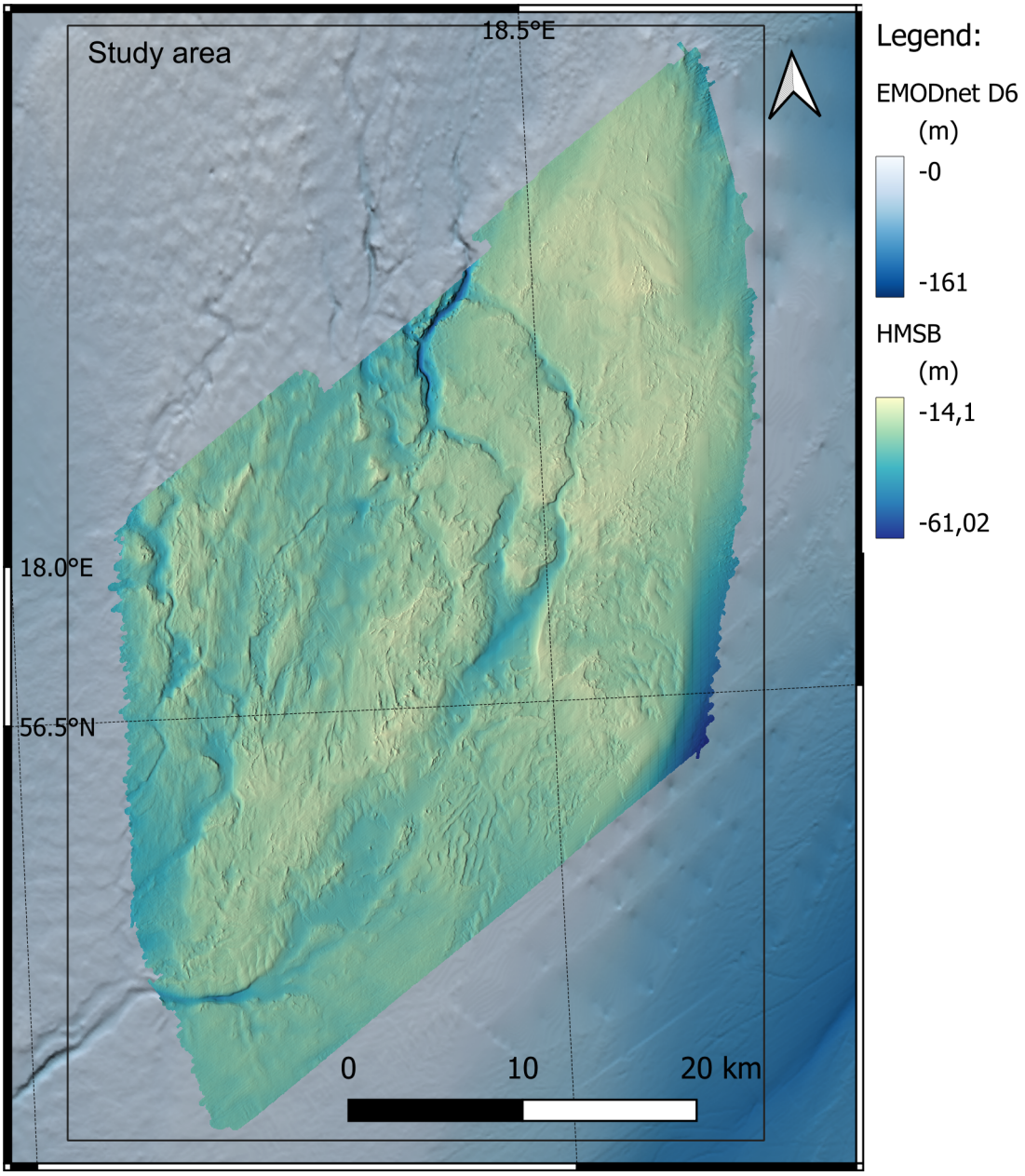

Figure 4.21: Overview of the available HMSB in the Hoburgs Bank study area. A hillshade map is overlain over the raw bathymetry data set to a vertical exaggeration of 10 with a light azimuth of 270 degrees.

whereas the fifth bypasses Hoburgs Bank entirely to the east and south. The fifth (easternmost) branch is not included in any further description of the channel network.

North of the HMSB, channel branches are elongated in a north-south fashion, deviating toward a northeast-southwest elongation on the bank (**??**). On a backscatter map, the channels are characterised by a low amplitude reflectivity, in the order of -30 ± 5 dB. The channels anabranch, that is channel segments diverge and converge, on the bank as the flow shifts towards a northeast-southwest (NE-SW) orientation. Individual channel segments reach a width of 3700 meters and depth values range between 5 and 22 meters (range of depth values in cross-section). Profiles of the channel bed show that the shallowest part of the channel network is toward the central area of the HMSB and thereby near the crest of Hoburgs Bank. The widest sections appear in the south-easternmost branch on Hoburgs Bank and the deepest parts are located on the entry of the easternmost branch onto the HMSB from the north. At the deepest part, a channel segment exhibits terracing, that is the channel bed does not slope smoothly towards the deepest part, instead, there is a distinct steepening marking a secondary channel within the encompassing channel (Figure 4.23).

Finger-like negative imprints, hereafter referred to as "fingers", extend from the slope of the channels toward the central part of channel segments. The fingers also occur on the eastern flank of Hoburgs Bank extending toward the trough east of the Hoburgs Bank. On a backscatter map, the fingers stand out as high-amplitude intensity features, in the order of -15 ± 5 dB (Figure 4.24).

4.2.2 Interpretation of negative landforms on Hoburgs Bank

The channel network is interpreted as a network of erosional meltwater channels. Due to an ascending profile from either point of origin, in the north or the southwest of the study area, the erosional channels are interpreted as being subglacially formed tunnel valleys. Low-amplitude backscatter of the channel beds is interpreted as relatively homogeneous glaciofluvial material. based on the shape and distribution of the fingers, they are interpreted as gravity flows originating on sloped channel banks and the sloped flank of Hoburgs Bank. A complete lack of sediment accumulation at the lower end of the gravity flows poses a question that will not be answered in this study, but left as an exercise to the reader.

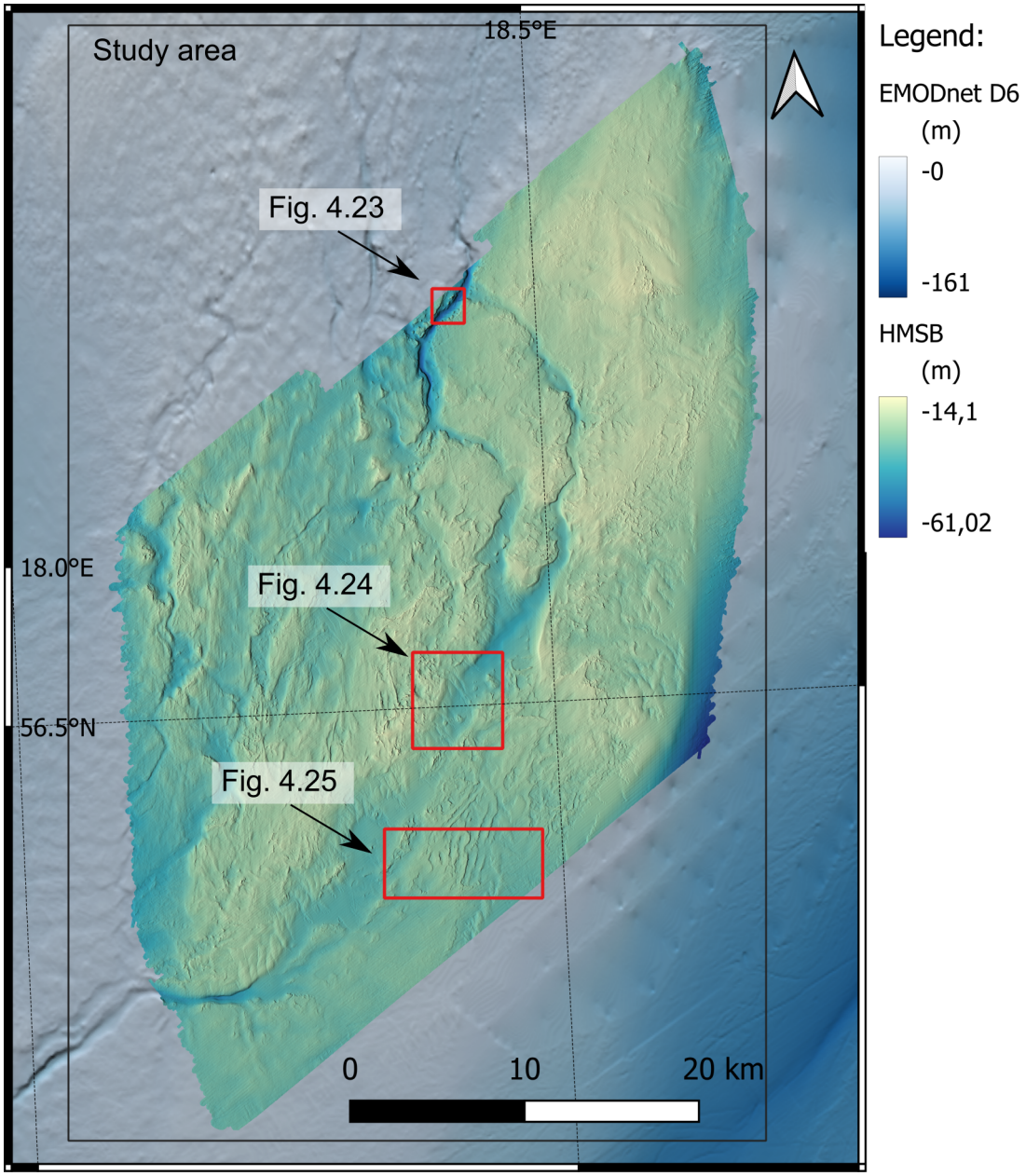

Figure 4.22: Overview of figures relating to negative and non-potential esker type landforms on Hoburgs Bank.

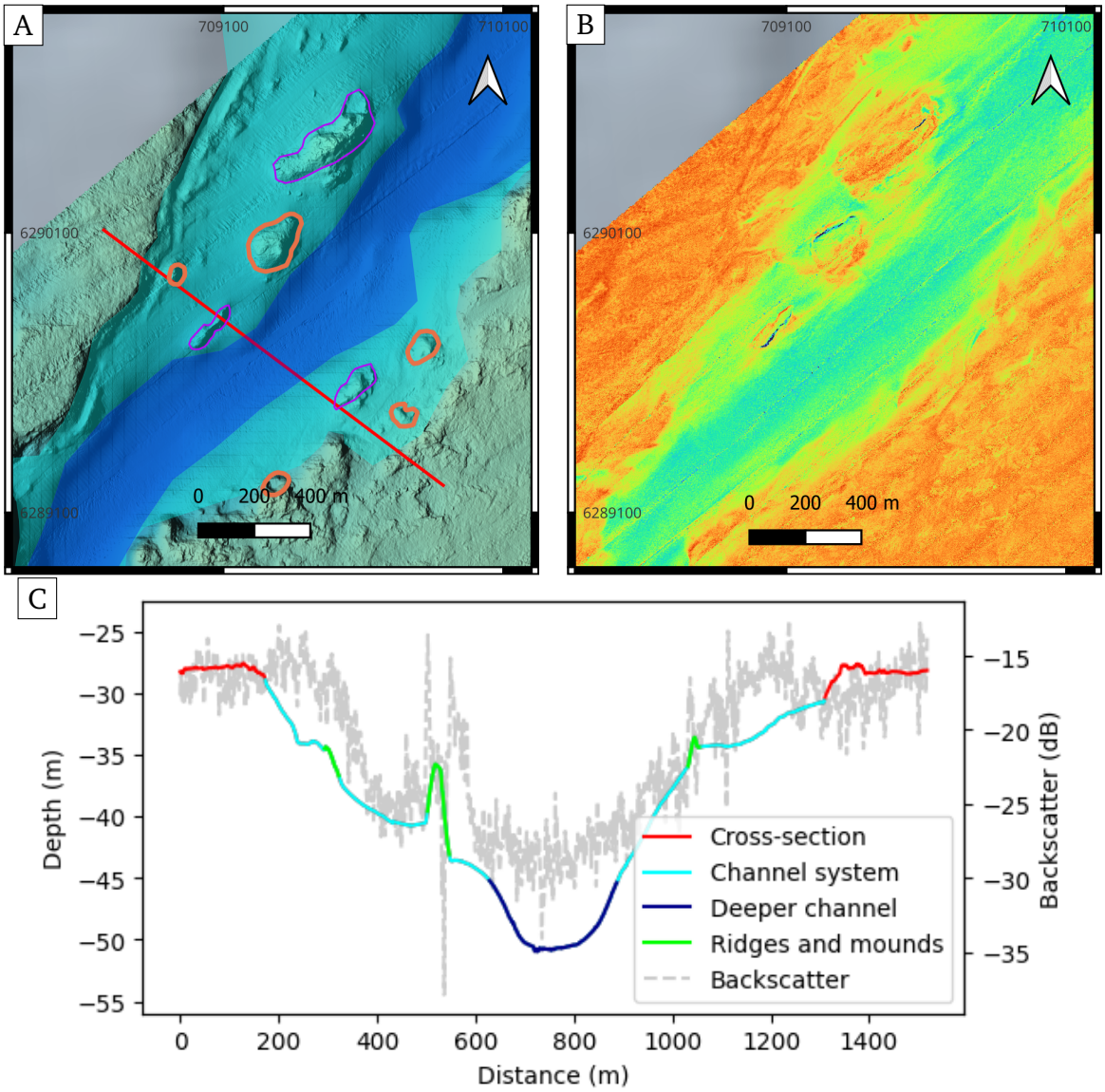

Figure 4.23: The deepening of the channel on the northern edge of the HMSB data is shown with interpretations in A and on a backscatter map in B. C shows a cross-section of the channel of both bathymetry and backscatter and the profile is coloured according to mapped features. The location of the figure can be found in Figure 4.22.

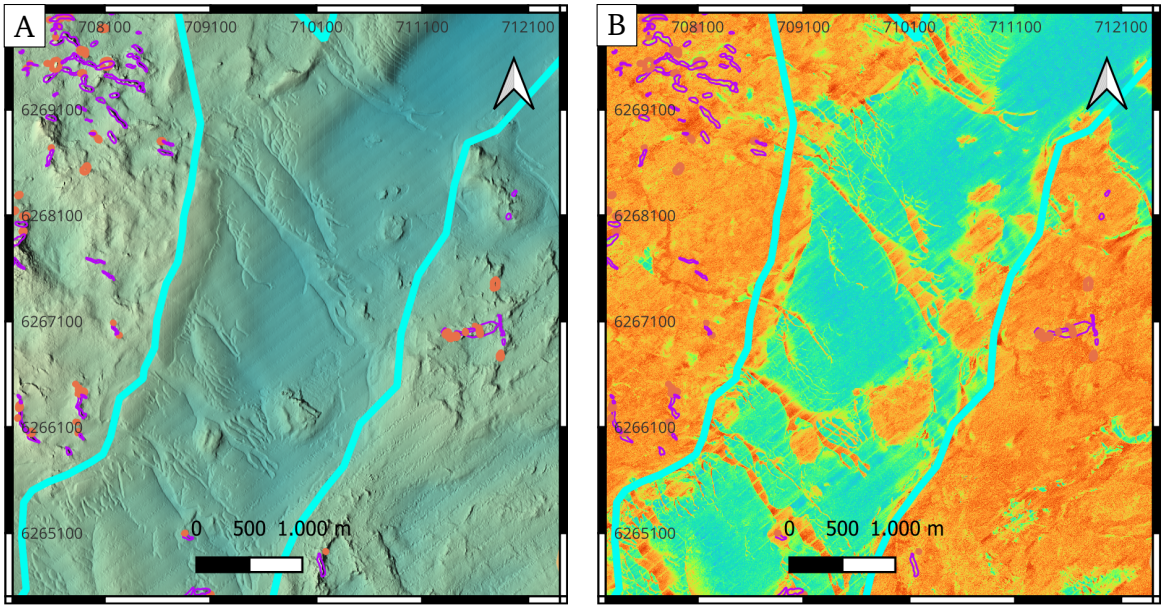

Figure 4.24: Example of fingers extending into a channel on Hoburgs Bank. A: Bathymetry, B: Backscatter map. The location of the figure can be found in Figure 4.22.

4.2.3 Positive landforms that are not potential eskers on Hoburgs Bank

Several quasi-linear features that resemble ridges occur on the Hoburgs Bank (Figure 4.25, A). They differ from other linear features because they are skewed, with one side of the crest having a low-angle relief and the other having a steep slope (Figure 4.25, C). They vary in length and orientation. A total of 91 individual lineations were mapped with a cumulative length of 143 km, thus, averaging 1.6 kilometers per mapped lineation. The lineations are primarily orientated in a north-south direction (Figure 4.25, B). An interpretation of the skewed linear features is not included in this study, they are only mentioned to justify their exclusion as mapped ridges in the following subsection.

4.2.4 Classifying positive landforms in the Hoburgs Bank

Other than the skewed lineations mentioned in the previous section, positive landforms are generally small. 90% have a length shorter than 132 meters, although the longest continuous segment reaches a length of 1182 meters (Figure 4.26, A). The height (maximum height of cross-sections) ranges between 0.2 and up to 11 meters, where 90% of mapped features are lower than 3.9 meters high (Figure 4.26, B). The width (width of maximum height cross-section) ranges between 3 and 159 meters, where 90% of mapped features are narrower than 38.5 meters (Figure 4.26, C).

A primary distinction is made between positive features based on their elongation ratio. 43% (2250) have an elongation ratio of less than or equal to two and are classified as

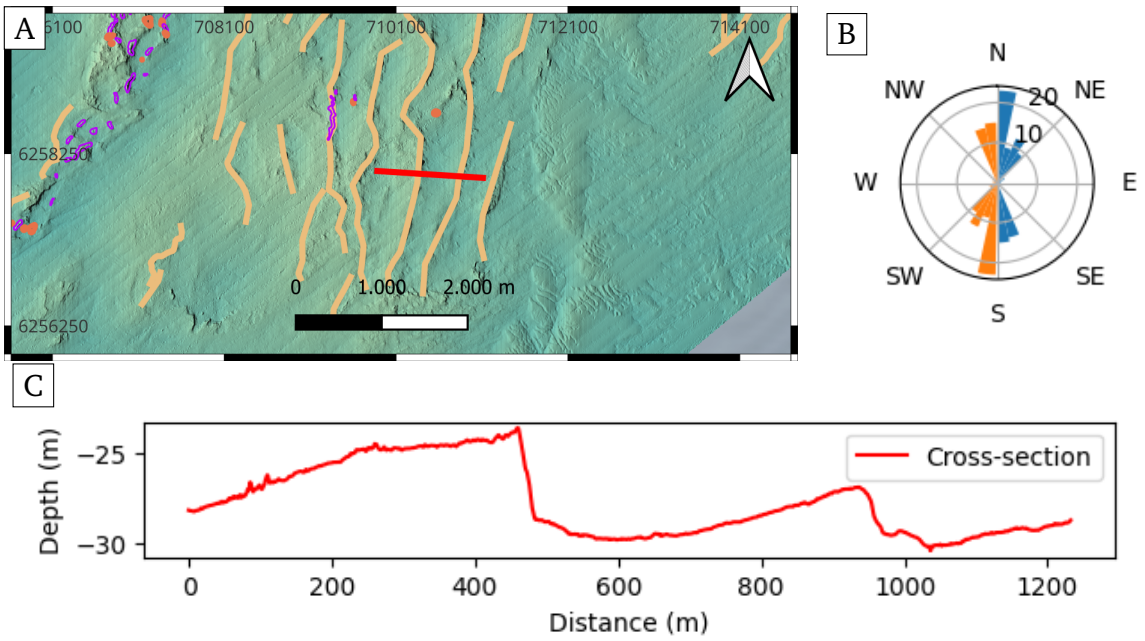

Figure 4.25: A) Example of lineations. B) The frequency distribution of their orientation. C) Cross-section of the example, location of the cross-section is shown in A). The location of the figure can be found in Figure 4.22.

Table 4.3: General attribute statistics of 5257 mounds and ridges on Hoburgs Bank.

Attribute	Minimum	Maximum	Average	Standard deviation
Length (m)	5	1182	68	65
Area (m^2)	26	49,310	1555	2322
Height (max.)	0.2	11.1	2.1	1.3
Height (avg.)	0.1	7.6	1.3	0.8
Height (std.)	0.0	3.1	0.6	0.4
Width (max. height)	3.1	158.8	24.0	12.2
Width (avg.)	2.9	110.8	19.1	9.0
Width (std.)	0.0	39.8	6.1	3.5
Sinuosity (of ridges)	1.00	1.47	1.05	0.05

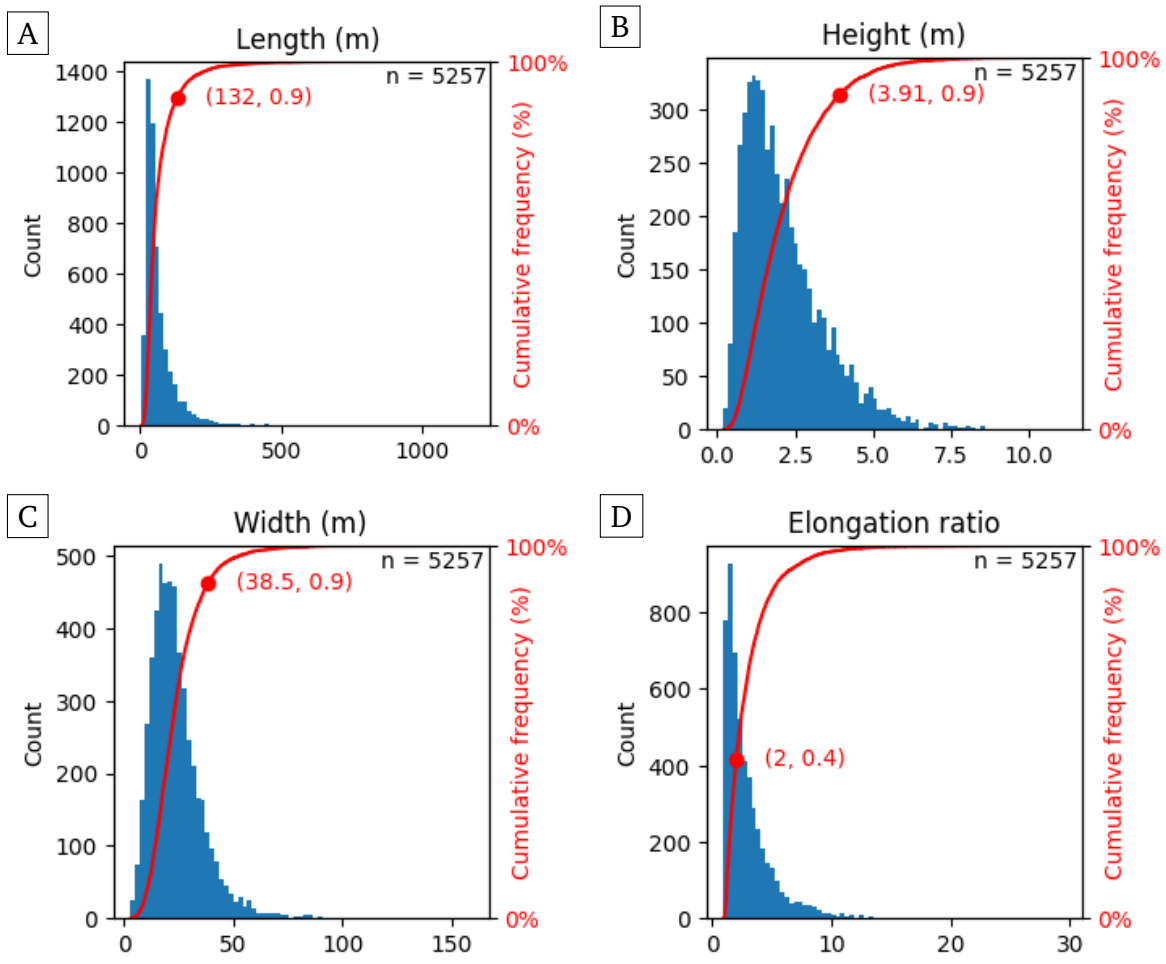

Figure 4.26: Statistical attribute distribution for ridges and mounds in the Hoburgs Bank. The four graphs all have 5257 observations each and the histograms are split into 72 bins.

mounds. 57% (3007 positive features) of ridges and mounds have an elongation ratio greater than two and are classified as ridges (Figure 4.26, D). The ratio of height versus (vs.) width differs slightly between ridges and mounds, where ridges tend to have a higher height vs. width ratio than mounds (Figure 4.27). Ridges are roughly 10.8 times wider than they are high but values range as low as 2.8 and up to 62.9. Mounds are roughly 13.5 times wider than they are high but values range between 2.6 and 72.0.

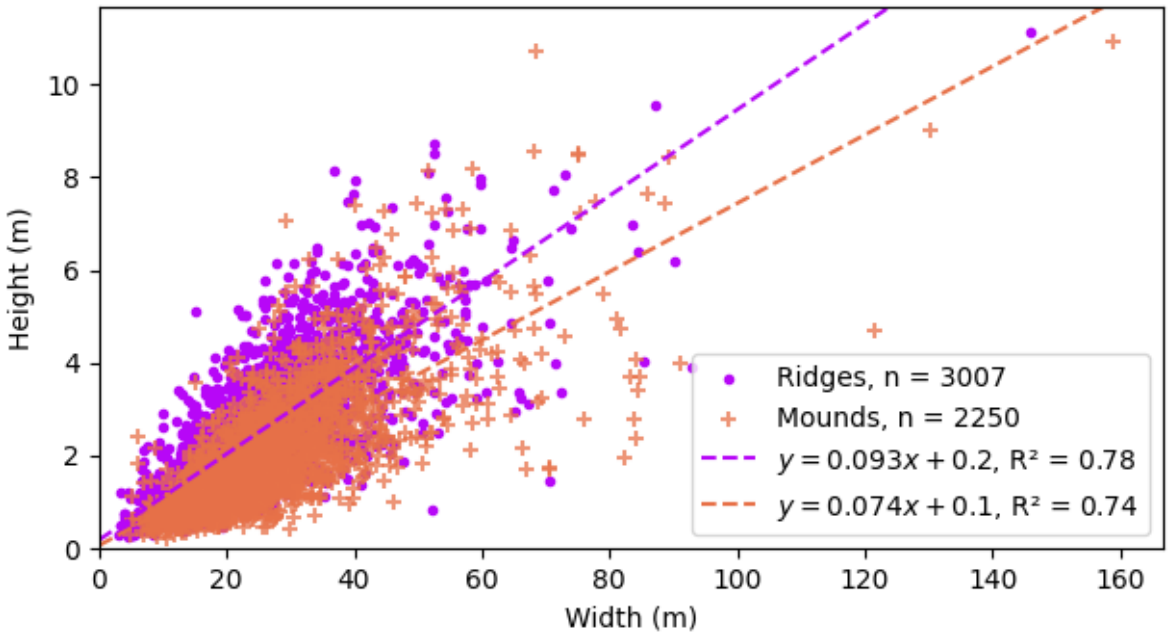

Figure 4.27: Height vs. width of ridges (magenta dots) and mounds (orange plus signs) on Hoburgs Bank and best linear fit (dashed lines) for the two landforms.

Ridges and mounds are distributed throughout Hoburgs Bank but are scarce in areas identified as channels. Figure 4.28 shows that ridges and mounds are not evenly distributed on the bank but occur in three near continuous east-west parallel bands. The bands are stretched in a north-south orientation and the density of ridges and mounds increases towards the east. In total 5257 ridges and mounds were mapped, 90% of which occur in the shallowest 15 meters of the HMSB.

4.2.5 Hoburgs Bank mounds

The mounds are subclassified into four groups based on two characteristics. Mounds that intersect another landform are said to be conjoined, whereas mounds that do not intersect another landform are said to be isolated. The morphology of mounds is distinctly round-topped, flat-topped, or crater-like in cross-section (Figure 4.30).

Conjoined mounds are most commonly overprinting underlying ridge structures and lin-

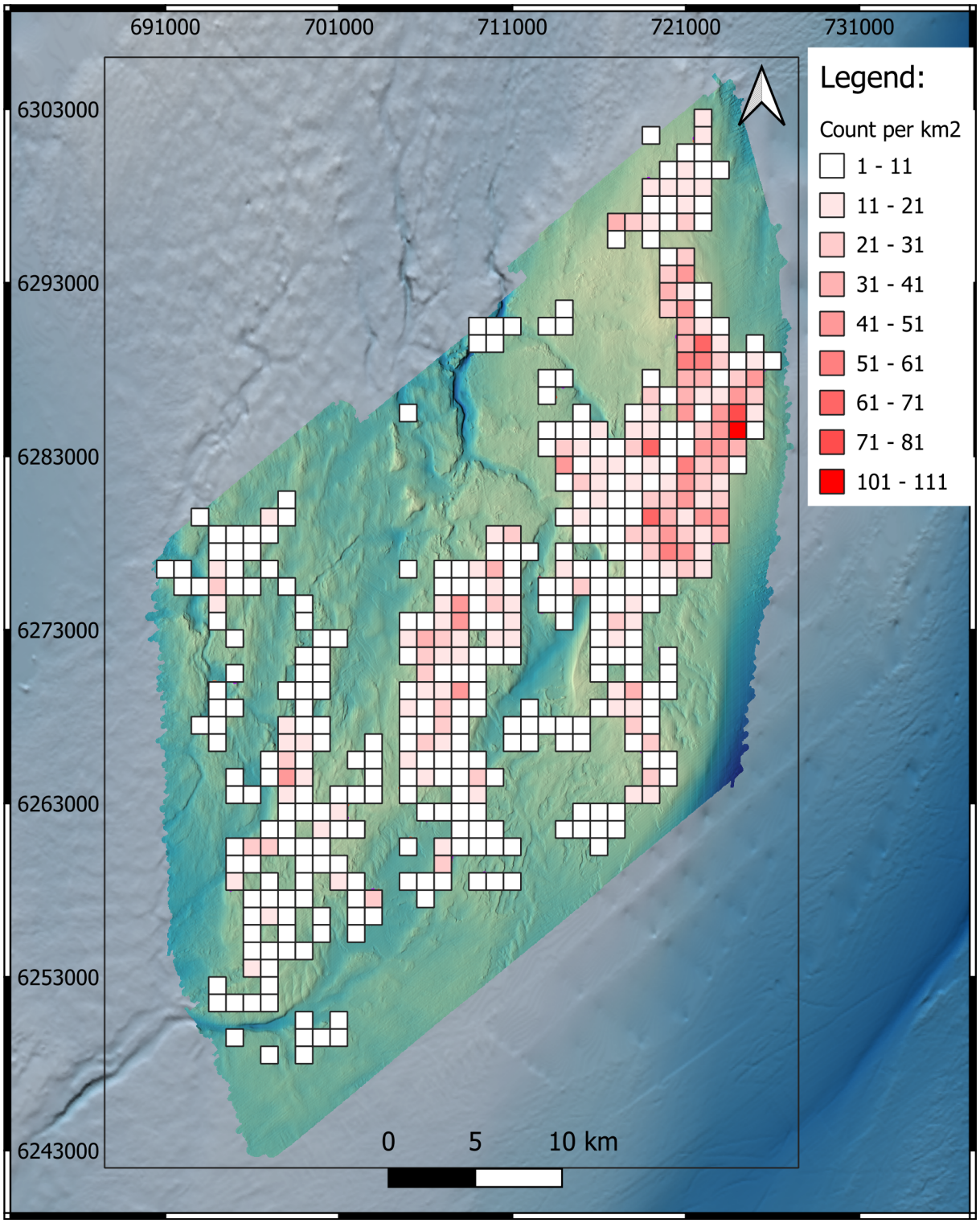

Figure 4.28: The density distribution of mapped ridges and mounds on Hoburgs Bank. Each pixel is one square kilometer and reflects the number of mapped features that intersect it. In the case where no feature intersects a pixel that pixel is omitted.

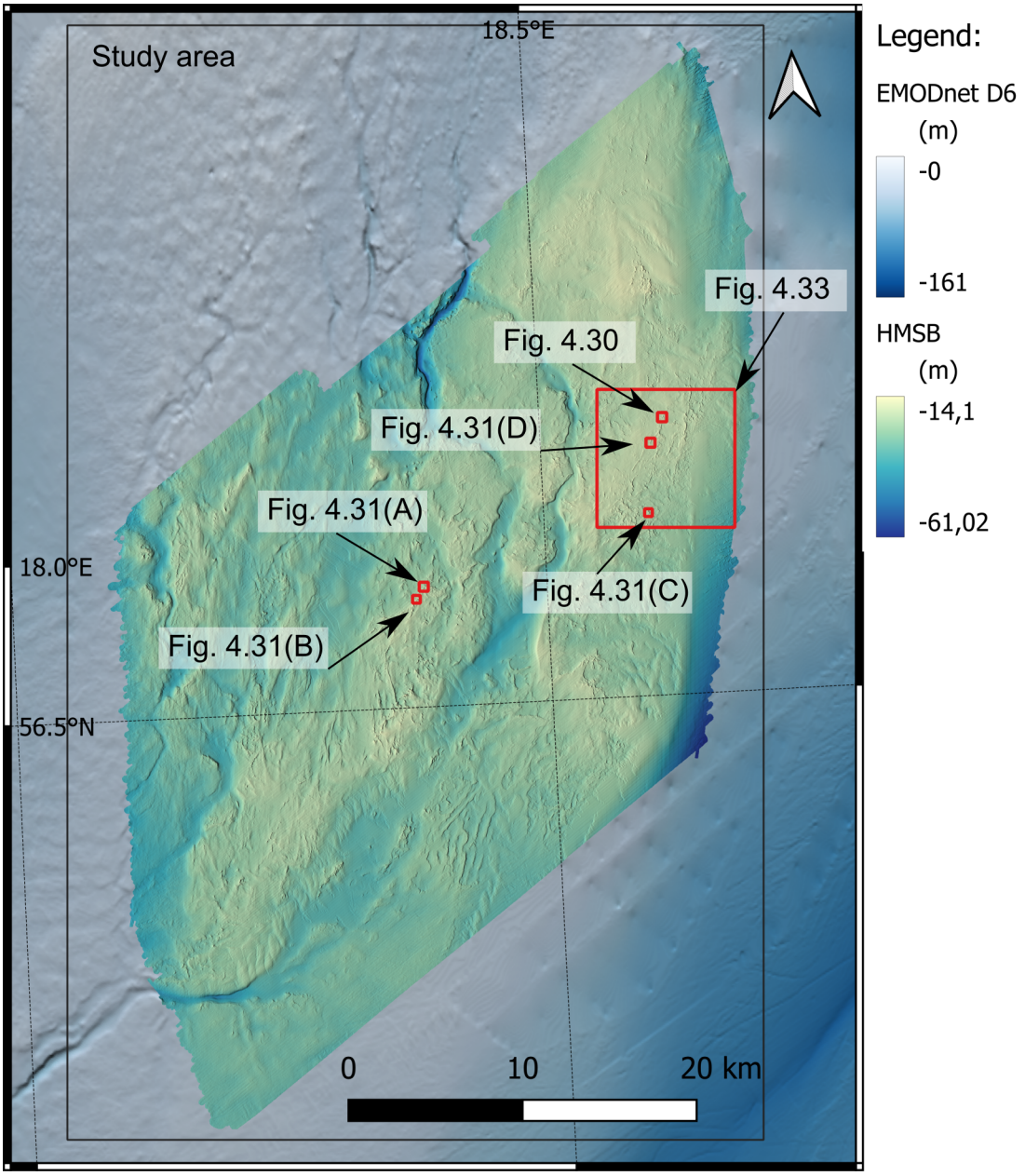

Figure 4.29: Overview of figures relating to potential esker type landforms on Hoburgs Bank.

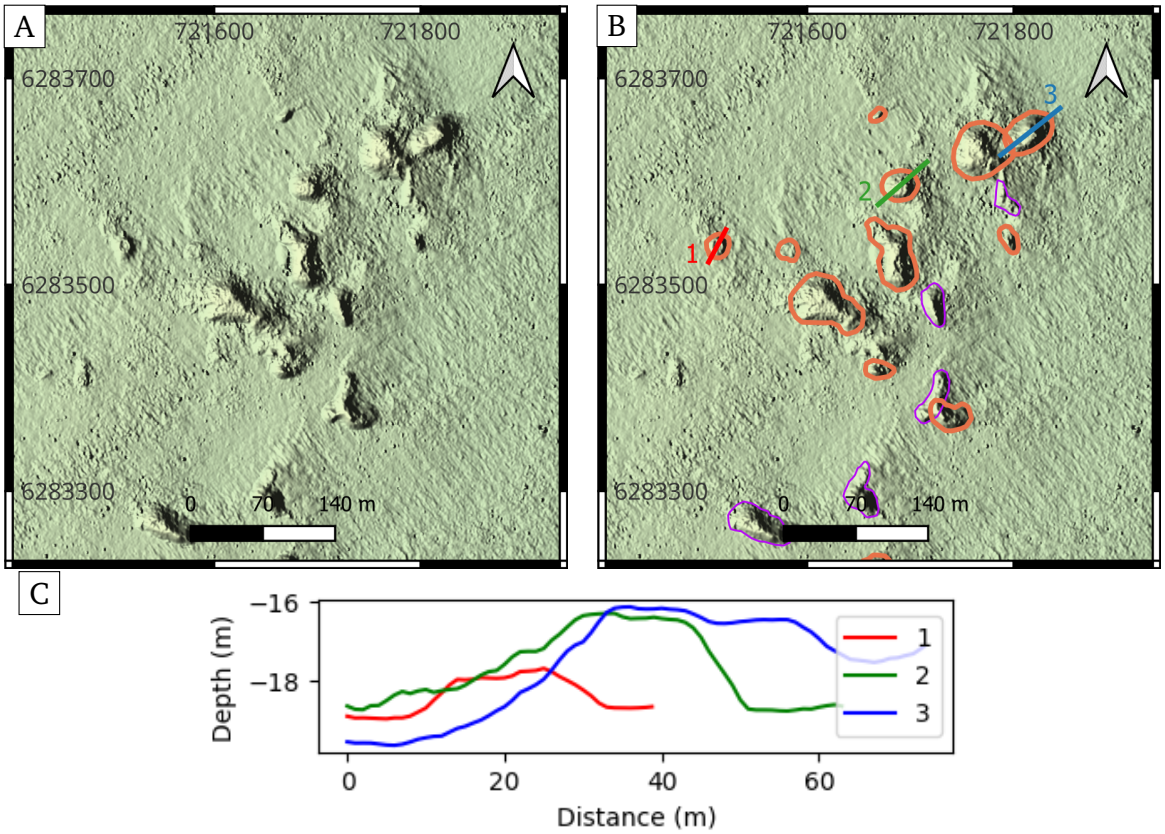

Figure 4.30: Example of different mound morphologies on Hoburgs Bank. A: HMSB with hillshade showing a collection of mounds and ridges. B: Mapping interpretation of A and the location of cross-sections one, two, and three (red, green, and blue respectively). C: Cross-sections one, two, and three show crater-like, round-topped, and flat-topped mounds. The crater-like depression in mound one is more apparent on the hillshade map in A than it is in the cross-section as the depression is minimal. The location of the figure can be found in Figure 4.29.

eations. The superposition of mounds over ridges is marked by the peak of a mound taking precedence over the crest of a ridge. There are three modes by which mounds intersect ridges. Firstly, mounds occur on the central part of a ridge section where the peak of a mound roughly coincides with the crest of a ridge (Figure 4.31, A). Secondly, mounds occur at an offset of a ridge crest, where both the peak of the mound and the crest of the ridge are distinguishable but the extent of the features overlap (Figure 4.31, B). Thirdly, mounds occur on the edge of a ridge but in line with the ridge crest (Figure 4.31, C). In the first case, the mounds are round-topped, whereas in the second and third cases, the mounds can be round-topped, flat-topped, or crater-like. Isolated mounds can form mound chains that follow a path similar to nearby ridges, or as a couple of mounds that occur in line with a general ridge path, seemingly filling a gap between ridge segments (Figure 4.31, D). Otherwise, mounds are distributed around ridges.

4.2.6 Interpretation of mounds on Hoburgs Bank

Variations in mound morphology can not be explained solely from bathymetric observations but would require a full sedimentological investigation. Note however that the occurrence of crater-like mounds is not simply a "normal" morphological feature. As sediments accumulate to form a mound the maximum possible steepness of the slope depends on the nature of accumulating sediment. A depression at the centre of a mound does not occur during formation unless the rate at which sediment accumulates is non-uniform over the mound area. Post-formation, round- or flat-topped, mounds can be altered to crater-like mounds by erosional processes, although the consistency of true central depression conflicts with any physical erosional processes. Erosion by fluid flow could explain crater-like mounds, whereby the sediments constituting a mound would act as a conduit for fluid flow, concentrating the flow in the central part of the mound. Finally, crater-like mounds can form if their centre collapses, this can occur if the mound forms with an ice core, thus building a typical round-topped mound that is altered to a crater-like mound as the ice core melts. The theory of ice-cored mounds on Hoburgs Bank would be an indicator of there having been dead ice incorporated in the landforms during their formation.

The overprinting nature of conjoined mounds on ridges and lineations reveals that the mounds must have formed at the same time or after the features which they overlap. Mounds occur almost exclusively in and around ridges, suggesting that the formation of mounds and ridges is controlled by similar factors. This is further evidenced by mound chains bridging the gap between ridge segments or acting as continuations of aligned ridge segments.

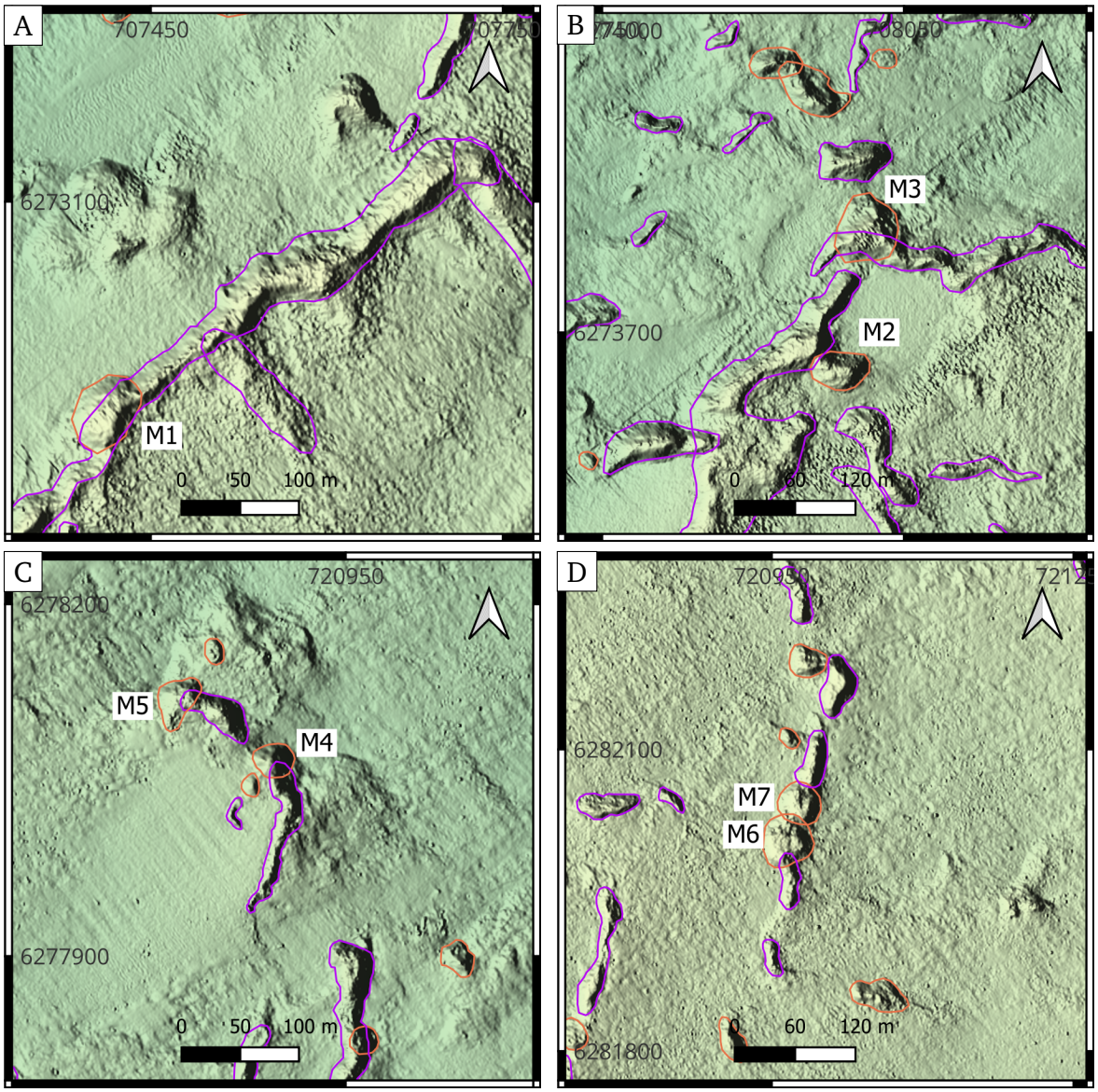

Figure 4.31: Spatial relation of mounds to ridges. A: M1 occurs along a ridge the crest is indistinguishable from the ridge. B: Mounds intersect ridges but the crest of the features, M2 and M3, is distinguishable from the ridge crest. C: M4 and M5 occur at the end of ridges, overlapping the extremity of the ridge. D: M6 and M7 occur as continuations of ridges, bridging the gap between ridge segments. The location of the figure can be found in Figure 4.29.

4.2.7 Hoburgs Bank ridges

Ridges on the Hoburgs Bank are straight to sinuous elongate landforms. The nature of ridges to be elongated allows for the assignment of additional descriptive parameters, sinuosity and orientation (parameters additional to those used to describe mounds). Furthermore, ridges exhibit variations in width and height along their length.

The sinuosity of ridges is used to classify segments as straight (sinuosity < 1.1), slightly sinuous (sinuosity ≥ 1.1 and < 1.2) and highly sinuous (sinuosity ≥ 1.2). Out of 3007 mapped ridge segments, 2471 are straight, 443 are slightly sinuous, and 93 are highly sinuous (Figure 4.32, A).

The orientation of ridges on Hoburgs Bank shows a primary grouping by frequency of north-south-orientated ridges, a secondary grouping of east-west-orientated ridges, and a tertiary grouping of northwest-southeast-orientated ridges (Figure 4.32, B).

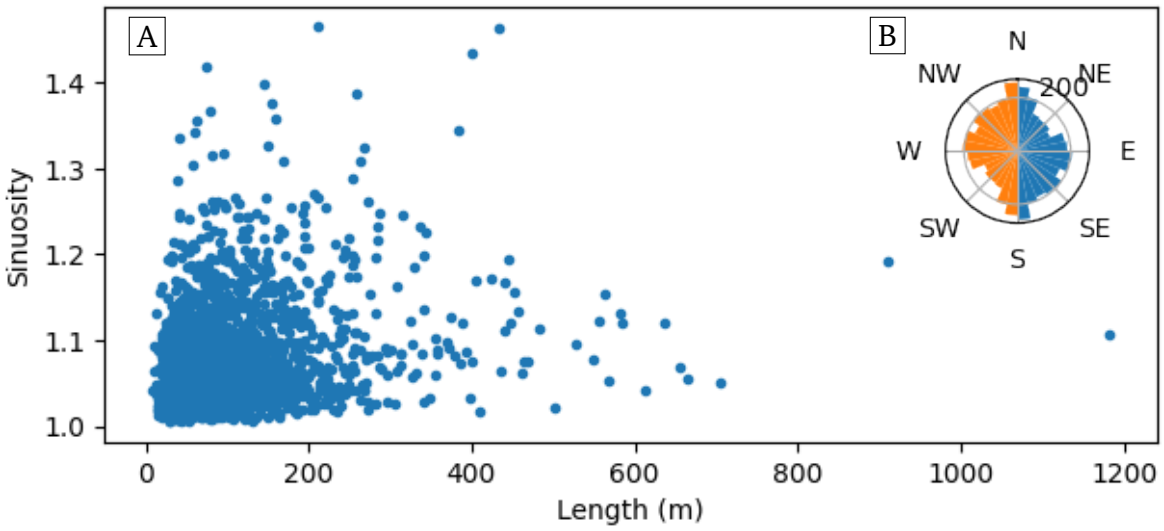

Figure 4.32: A: Length vs. sinuosity of ridges on Hoburgs Bank. B: Frequency distribution of the orientation of ridges on Hoburgs Bank.

Ridge crest morphology is flat-crested, round-crested or sharp-crested and it can vary between all three in a single ridge segment. In rare cases, crater-like depressions occur on either end of a ridge segment. The distribution of ridges is, as has been mentioned, correlated to the occurrence of mounds, primarily in shallower water depths (Figure 4.28). The three mound and ridge bands (in Figure 4.28) are marked by an alignment of ridge segments and/or mound chains. This relationship of ridge and mound alignment is most prominent in the easternmost field and less so in the westernmost field.

4.2.8 Interpretation of ridges on Hoburgs Bank

The primary and secondary orientations of ridges are consistent with the changes of orientation of channels on the bank although their occurence is nearly mutually exclusive. The few ridges and mounds that are found in channels (in the northern edge of the study area, (Figure 4.23) do share all the same characteristics as ridges and mounds found elsewhere. The absence of ridges and mounds in channels can be partially explained by the finger-like structures discussed in Subsection 4.2.2. Sediments mobilised by gravity flows could contribute to the burial of ridges and mounds that occur inside the channels. In the places where ridges and mounds are found in the tunnel valley, the channel bed is terraced (Figure 4.23) with a distinct lack of gravity flows. Alternatively, the formation of ridges and mounds might be mutually exclusive with the formation of the tunnel valley or the formation of ridges and mounds occurs before the formation of the tunnel valley.

4.2.9 Alignment of ridges and mounds

The spatial distribution of ridges and mounds on bathymetric highs is further exemplified by shallower features forming alignments, that is, individual mounds and ridge segments align to form a more spatially continuous distribution over several kilometers (Figure 4.33). Surrounding the aligned ridges and mounds are ridge segments that are primarily, but not exclusively, perpendicular or sub-perpendicular to the ridge and mound alignment. As the distance increases from ridge alignments, segment orientation becomes more chaotic and mounds become more abundant relative to ridges. Compared to the entirety of ridges and mounds, aligned ridges and mounds are longer (126 meters vs. 68 meters on average), cover more area (3471 square meters vs. 1555 square meters), are higher (average maximum height cross-section of 3.0 meters vs. 2.1 meters), are wider (average width of maximum height cross-section of 31 meters vs. 24 meters) and are slightly more sinuous (average sinuosity of 1.07 vs. 1.05).

4.2.10 Final interpretation of ridges and mounds on Hoburgs Bank

Based on the apparent sinuosity of the ridge and mound alignments and the sub-perpendicular orientation of non-aligned positive features they are interpreted as a GSRN. The alignments are interpreted as main drainage pathways. The highly fragmented nature of the GSRN suggests that ridge and mound formation did not occur synchronously along the length of an alignment. An increasingly chaotic orientation of ridges and mounds with increasing distance to alignments suggests that the main drainage pathways influence the orientation of surrounding landforms. The final interpretation is shown in Figure 4.34.

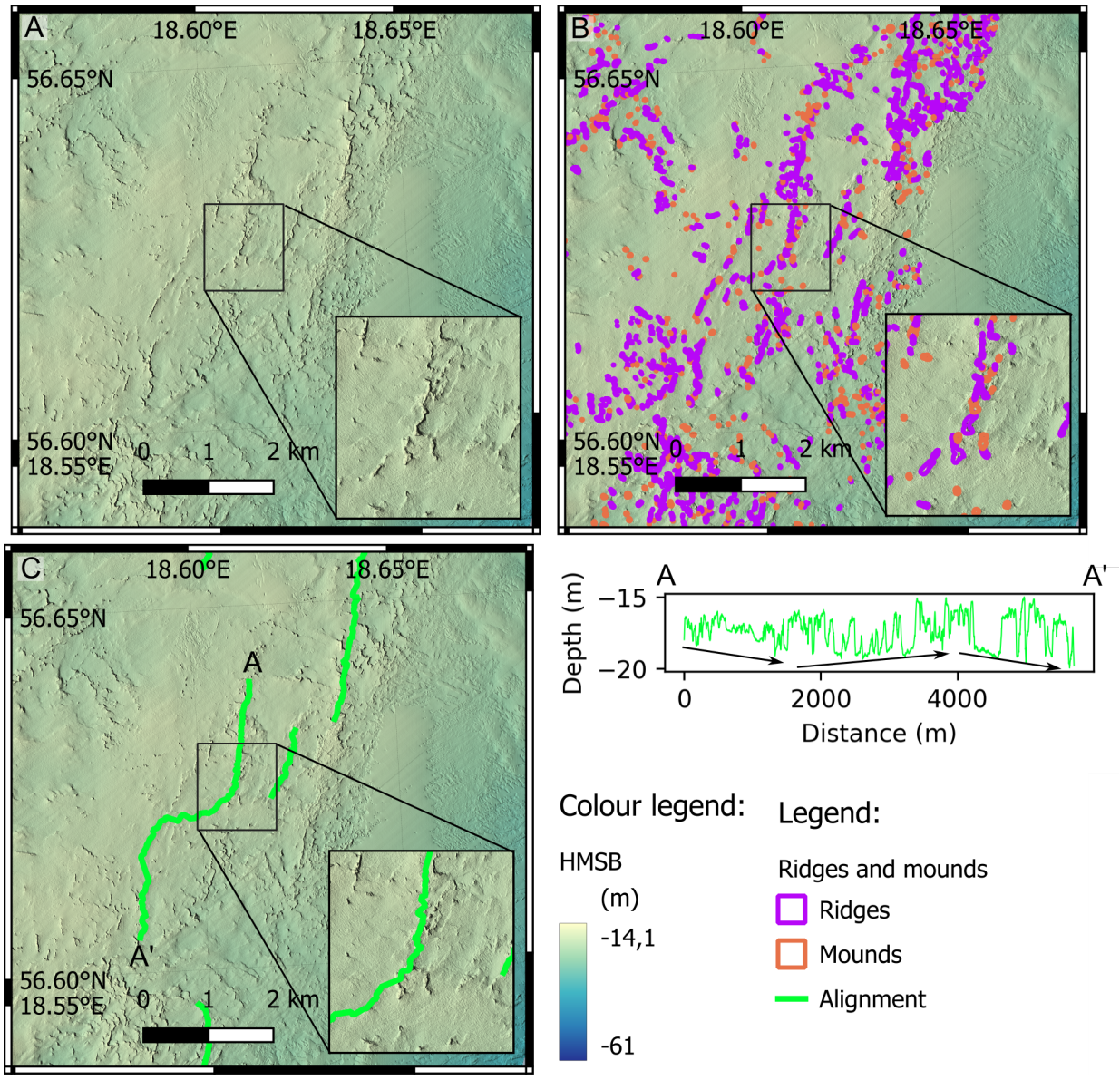

Figure 4.33: Example of interpreted ridge and mound alignments in the easternmost distribution band. A: Uninterpreted bathymetry. B: Mapped ridges and mounds. C: Interpreted alignments of ridges and mounds and a profile spanning a five-kilometer continuous alignment. All figures also include a zoomed-in section to highlight the alignment of features. The location of the figure can be found in Figure 4.29.

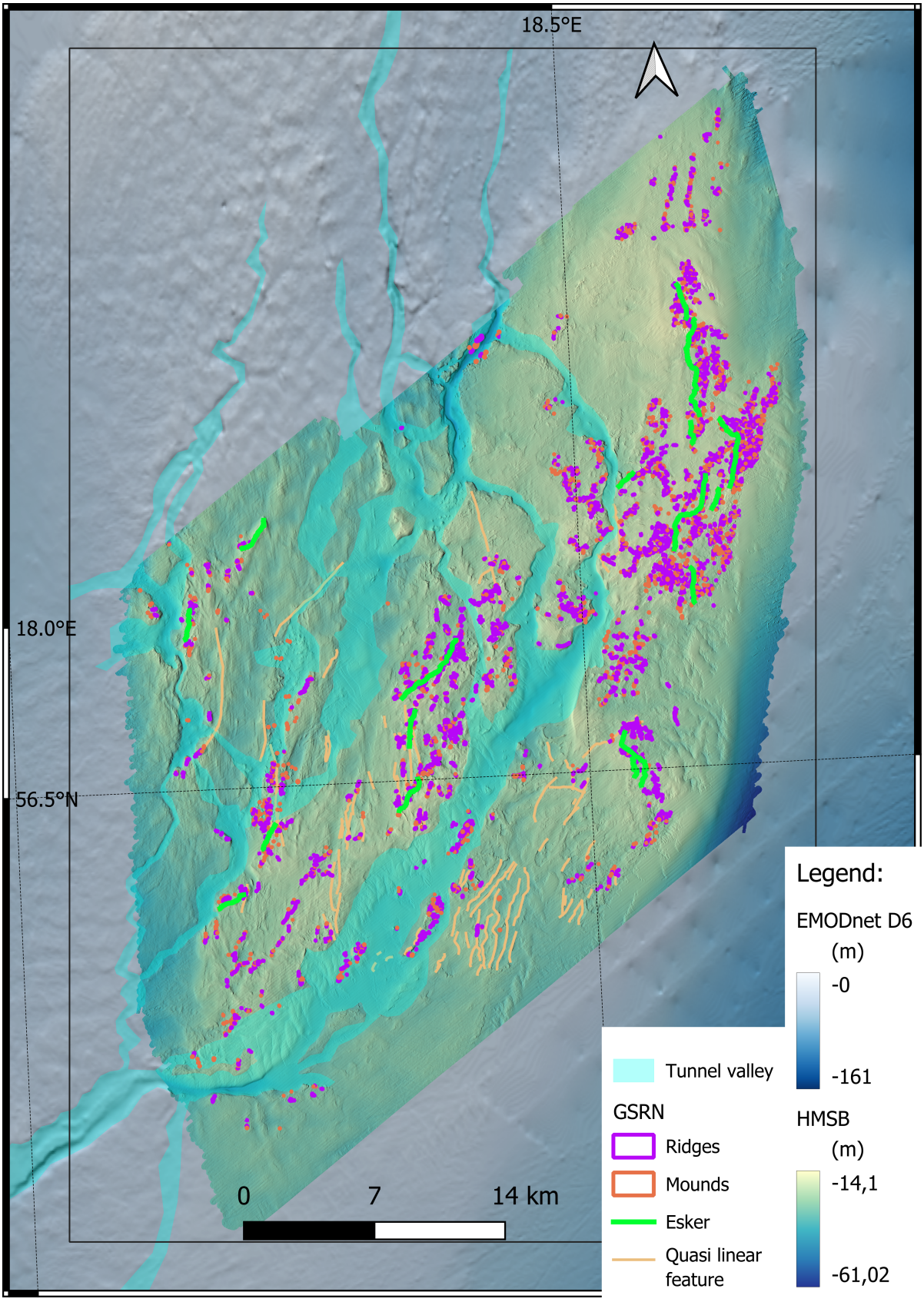

Figure 4.34: All mapped features on Hoburgs Bank and their interpretation.

Table 4.4: General attribute statistics of positive features comprising aligned ridges and mounds on Hoburgs Bank

Attribute	Minimum	Maximum	Average	Standard deviation
Length (m)	15	1182	126	130
Area (m^2)	152	35,636	3,472	4,672
Height (max.)	0.5	8.2	3.0	1.4
Height (avg.)	0.3	5.8	1.9	0.9
Height (std.)	0.1	2.4	0.8	0.4
Width (max. height)	7.1	85.4	31.4	13.6
Width (avg.)	6.7	66.8	24.1	9.4
Width (std.)	1.4	27.0	7.7	3.9
Sinuosity	1.01	1.47	1.07	0.06

4.3 Modelling the subglacial hydrology

In an attempt to better understand the subglacial meltwater system of the EISC around the two study areas of Hoburgs Bank and Hopendjupet (Figure 4.35) a simple hydrological model was created. The model includes an assessment of flow accumulation for three time-slices, 14.75 ka BP, 15.5 ka BP and 16.0 ka BP (Figure 4.36). These time slices are chosen as they correspond with the simulated deglaciation of the study areas. The 14.75 ka BP time-slice captures the deglaciation of Hoburgs Bank (Figure 4.36, E), whereas the 16.0 and 15.5 ka BP time-slices capture the deglaciation of Hopendjupet (Figure 4.36, B and D). Note that between 16.0 ka BP and 14.75 ka BP, the ice sheet model shows rapid deglaciation of the BSIS but a local advance of the Baltic sector of the FIS reaching a maximum extent just south of the Hoburgs Bank study area (Figure 4.36, E).

The model is run for a range of floatation factors, F in Equation 3.1, including scenarios where drainage is completely topography controlled, F = 0, and where drainage is completely independent of topography, F = inf (Figure 4.37, Figure 4.38 and Figure 4.39). Note that in the margins of the ice thickness map (<10 km for the edge) all flow appears to be topographically controlled due to the resolution of the input data (10 by 10 kilometres) as there is no gradient change in ice thickness. This means that the model does not capture the area where eskers are suspected to form, however, the location of modelled drainage pathways and density can be used to infer whether the subglacial meltwater system was under low or high water pressures.

4.3.1 Hopendjupet, 16.0 ka BP

Figure 4.38 shows that a modelled drainage pathway that coincides with mapped meltwater landforms persists in the north-eastern quadrant (ca. 70 km from the model edge) of the

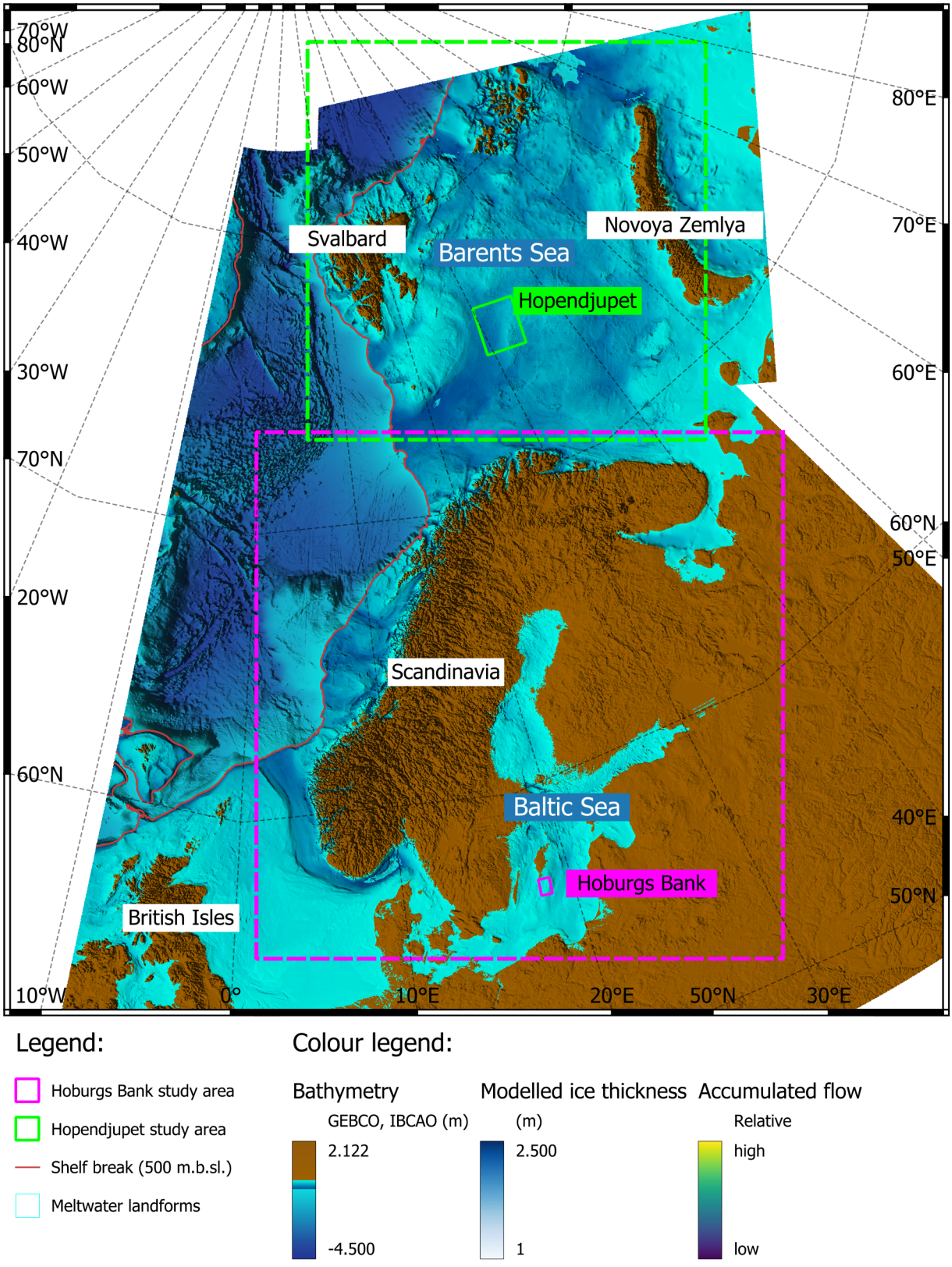

Figure 4.35: Overview of the modern topography for the area that was covered by the EISC. Note that the colour scale repeats at the slope break (500 m.b.sl.) to highlight the shelf bathymetry. The two study areas, Hopendjupet (green) and Hoburgs Bank (pink) are shown as solid rectangles whereas the extent of figures relating to the extent of the BSIS (green) and the FIS (pink) are shown as dashed rectangles. Coordinates are in CRS EPSG:4326.

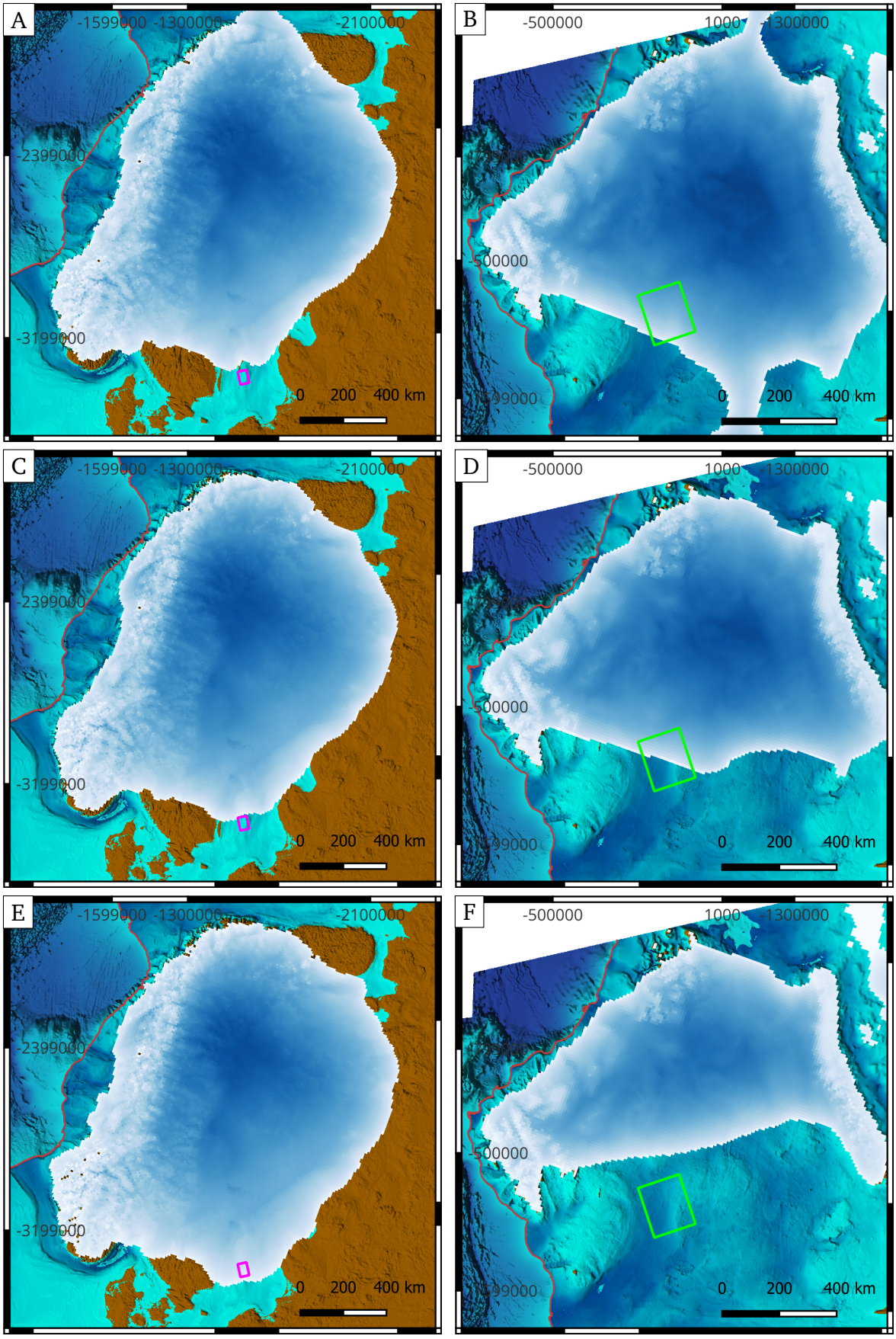

Figure 4.36: Ice thickness of the EISC used in hydrological modelling for three timeslices, 16.0 ka BP (A, B), 15.5 ka BP (C, D) and 14.75 ka BP. Left side figures centre on the FIS (A, C, E) and right side figures centre on the BSIS (B, D, F). The colour legend can be found in Figure 4.35.

figures for all modelled F-values (excluding F = inf). The downstream part (closer than ca. 70 km from the model edge) has a better fit with F-values of 0.925 and below.

4.3.2 Hopendjupet, 15.5 ka BP

Figure 4.39 shows that a drainage pathway is modelled coinciding with the mapped meltwater landforms for all F-values, excluding F = 0 and F= inf.

4.3.3 Hoburgs Bank, 14.75 ka BP

Figure 4.37 shows that modelled drainage pathways are relatively stable for a range of F-values outside of the bank. On the bank, channel density increases with increasing subglacial water pressure, failing to capture the true width of the meltwater system until an F-value of 1.1 is reached.

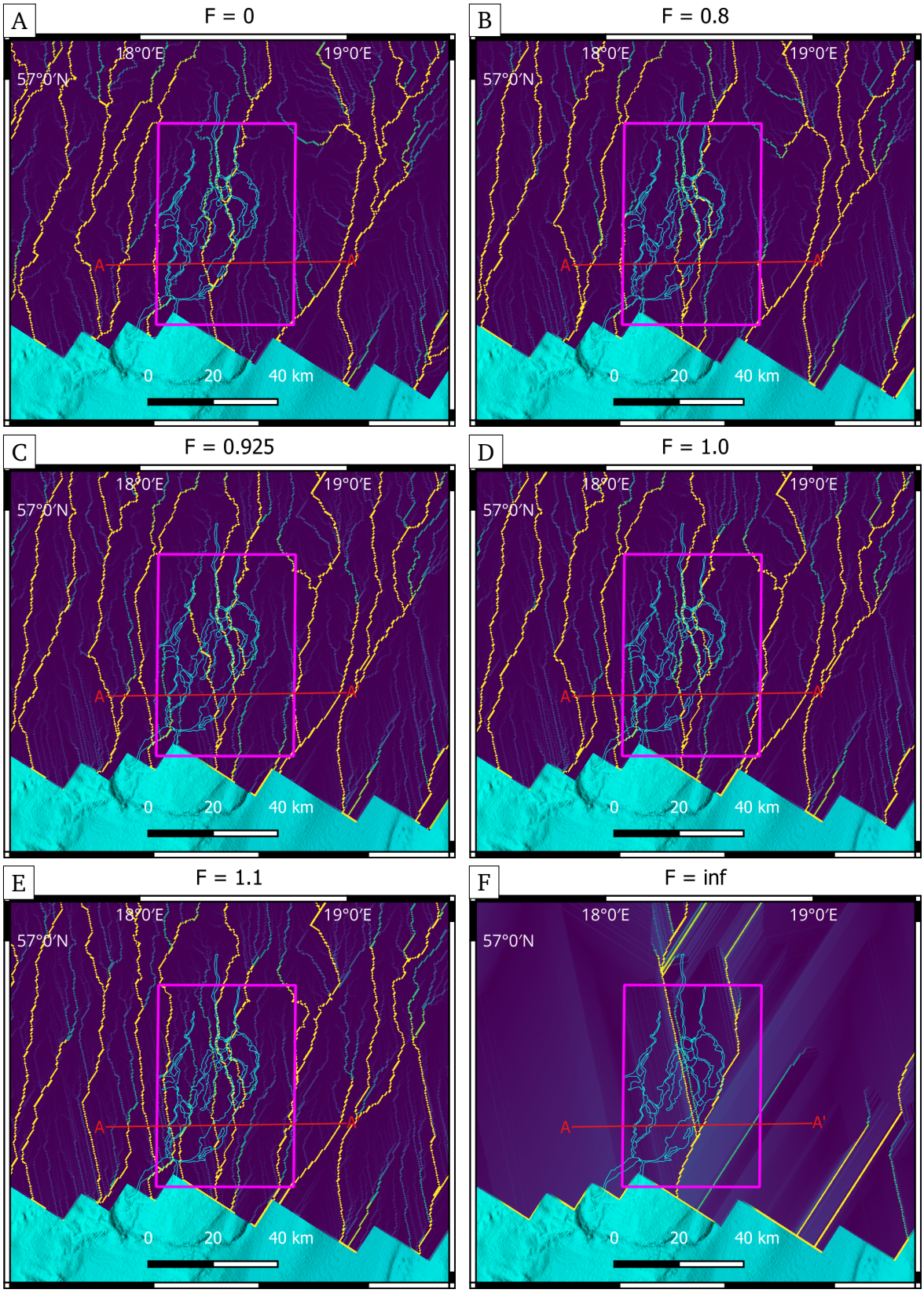

Figure 4.37: Modelled relative accumulated flow in the ice-marginal area of time-slice 14.75 ka BP on Hoburgs Bank for a range of F-values. High accumulated flow is shown in lighter colours and low accumulated flow in darker colours.

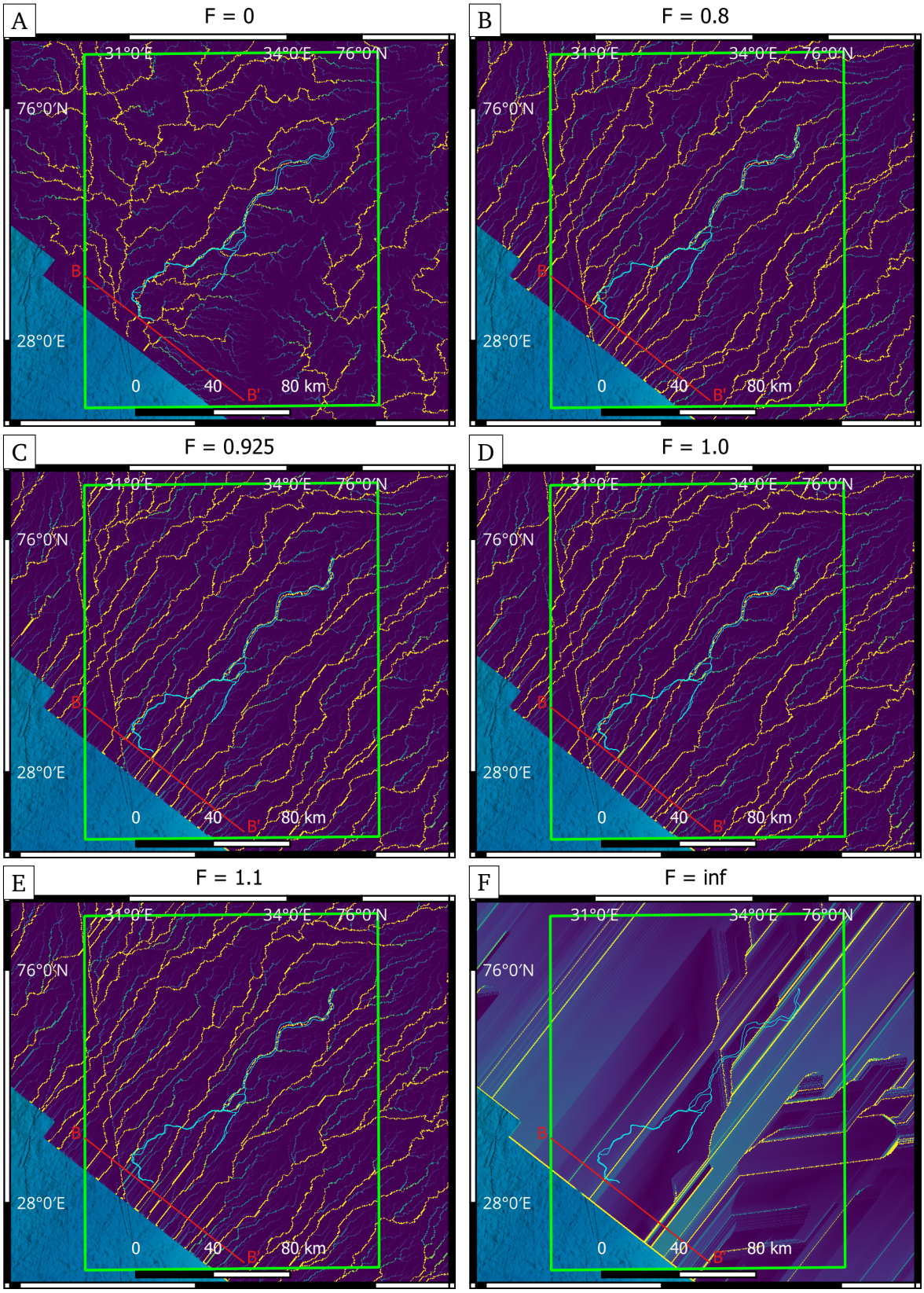

Figure 4.38: Modelled accumulated flow in the ice-marginal area of time-slice 16.0 ka BP in Hopendjupet for a range of F-values. High accumulated flow is shown in lighter colours and low accumulated flow in darker colours.

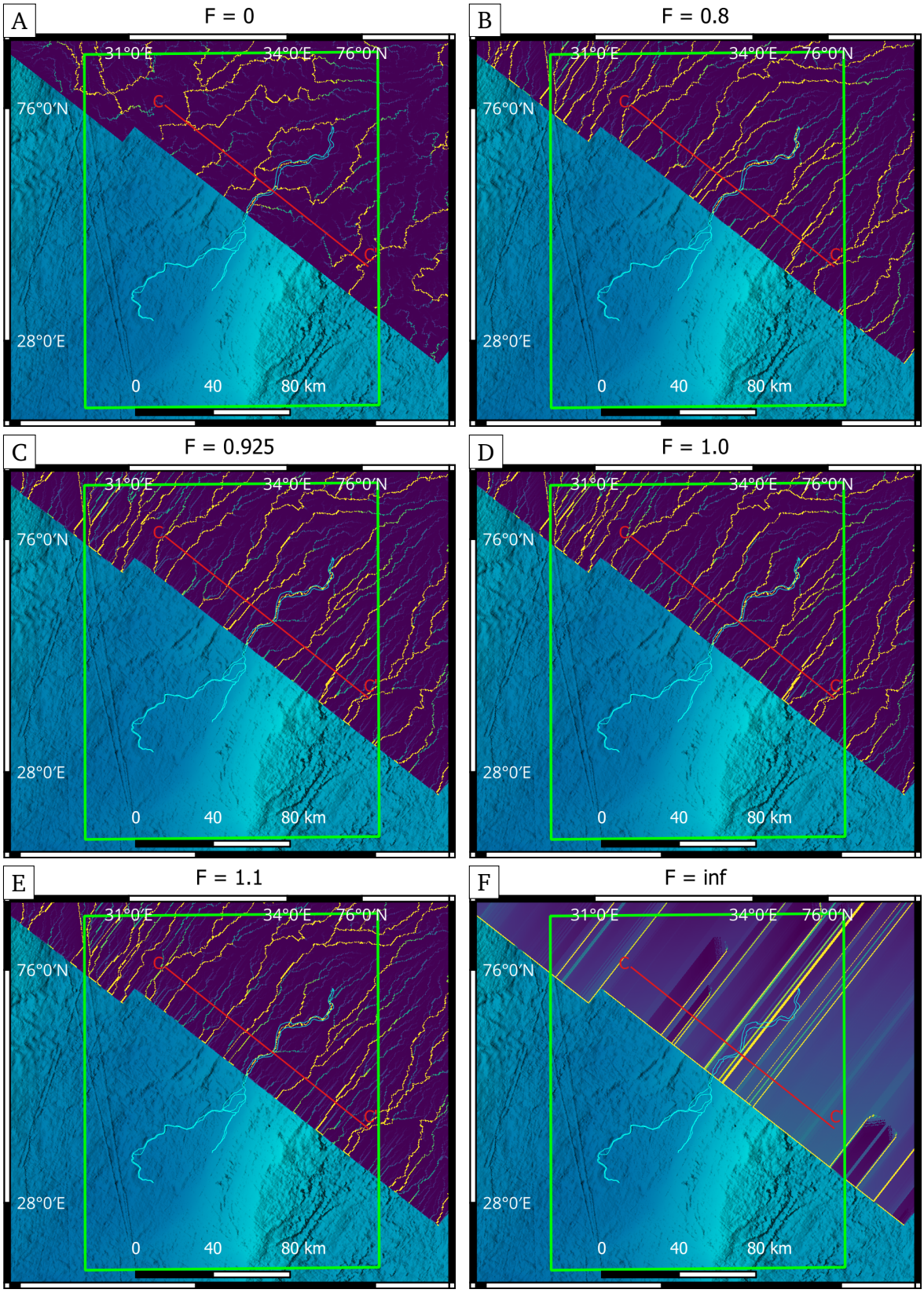

Figure 4.39: Modelled accumulated flow in the ice-marginal area of time-slice 16.0 ka BP in Hopendjupet for a range of F-values. High accumulated flow is shown in lighter colours and low accumulated flow in darker colours.

5

Discussion

The primary aim of this study was to investigate the morphological expression of channelised meltwater routing in marine- and lacustrine-terminating ice streams. The two study areas represent a variety of esker depositional systems, from the complex esker system on Hoburgs Bank to the relatively simple ERS in Hopendjupet. The following discussion aims to elicit the similarities and differences between eskers formed in marine- or lacustrine-terminating ice sheets and those formed in a terrestrial setting.

5.1 Hopendjupet EB

In the northeastern section of the Hopendjupet study area, a series of disconnected ridges and mounds align to form the Hopendjupet EB. The EB is fully located in a meandering channel, as evidenced by numerous cross-cutting channels within the channel system, where the position of esker beads potentially marks the final channel location before deglaciation (Figure 5.1). The southernmost part of the EB exhibits downstream ascending topography, even though a more favorable descending topography is evident to the west and also marked by an erosional channel. Individual beads exhibit a round or flat-topped morphology. The entire system coincides with unit pockmarks on the seafloor which suggest a relatively soft seafloor. Numerical modelling shows that drainage in this area is possible for all modelled flotation factors except a purely topographically controlled system (Figure 4.39).

The Hopendjupet EB has been thoroughly described and analysed in Shackleton et al. (2023). Shackleton et al. (2023) noted that the EB represents a quasi-annual record of a retreating ice margin as has been described in Livingstone et al. (2020) for esker beads in Nunavut, Canada. The results of this study are in accordance with the interpretation of Shackleton et al. (2023) of inferred retreat rates derived from bead spacing along the

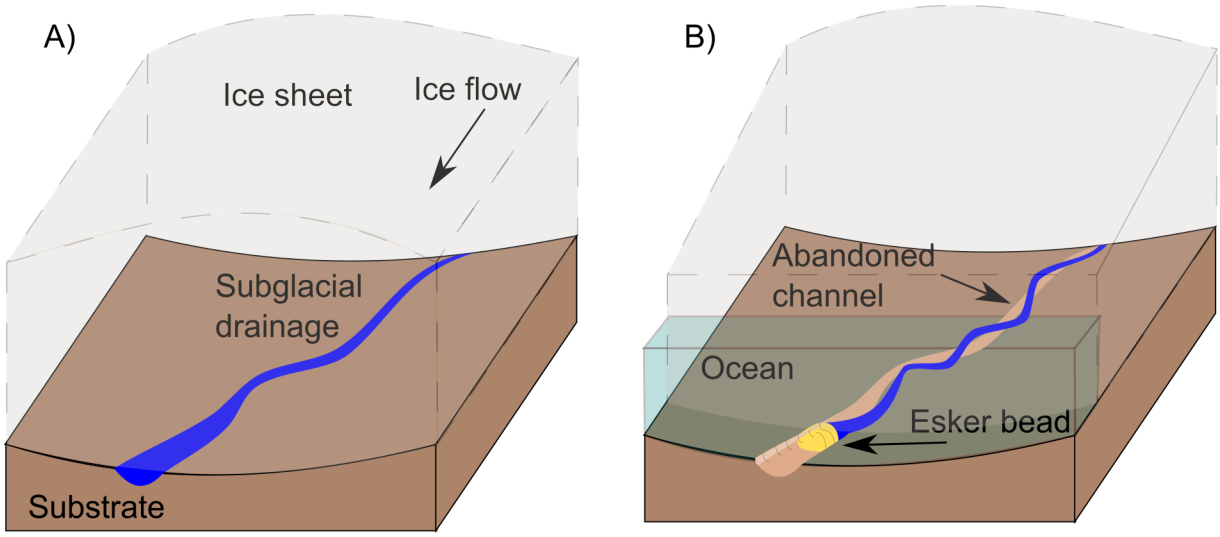

Figure 5.1: A sketch of the depositional setting for the beaded esker system in Hopendjupet. A: Erosive subglacial drainage beneath the ice sheet. B: Esker beads are deposited at the margin of the ice sheet.

axis of the system (Figure 4.14, rolling average). The occurrence of flat-topped beads has been attributed to a limited accommodation space, specifically the water level at the ice margin (Livingstone et al., 2020). In the case of the Hopendjupet EB, this cannot be the case where flat-topped beads are found at more than 190 m.b.sl. today (although there is a lack of HMSB coverage in shallower regions) and the modelled relative sea level change for Hopendjupet at 15 ka BP adds another 248.5 meters of water (Gowan et al., 2021). As such, an alternative explanation has to be found for flat-topped beads in Hopendjupet.

5.2 Hopendjupet WRS and DRN

The largest eskers discussed in this study are the WRS comprised of three mostly single-crested flat- to round-topped eskers (WRS, 1-3), interpreted as esker enlargements and a distributary segment (DRN), interpreted as a complex esker. The esker system follows an erosional channel, exhibiting a gradual change from channel to esker and completely replacing the morphological expression of a channel. The width of the esker enlargement exceeds that of the channel that it overprints which suggests that its formation was not confined by a subglacial tunnel. In cross-section, the esker enlargement appears flat-topped. Retreat ridges and geometric ridge networks abruptly disappear at the edges of the esker enlargement which indicates that they were formed at the front of the ice margin. The esker enlargement gradually narrows towards the north from approximately 352 meters (average width of the southernmost section) to 218 meters (average width of the northernmost section).

The complex esker exhibits an overall anabranching distribution, however, where branches converge, they abruptly change to an erosional channel. The location of the complex esker coincides with retreat ridges which are both superimposed on and covered by the complex esker system.

The morphology of the WRS eskers conforms with the description of esker enlargements in Fennoscandia and Canada (Dewald et al., 2021; Lindström, 1993). The measured width of the WRS esker enlargements (averaging around 350 meters) matches well with those described by Dewald et al. (2021) (median width of 327 meters) and the height (between 6 and 7 meters on average, reaching a maximum of 23.9 meters) is in the same order of magnitude (height ranging between 10 and 40 meters) as described by Lindström (1993). Dewald et al. (2021) propose a model for esker enlargement formation in which the main cause for the formation of an esker enlargement is the collapse of the meltwater conduit, either by a sudden decrease in hydraulic pressure or by decreased stability of the conduit roof. As mentioned in their paper (Dewald et al., 2021), the model does not fit well with marine-terminating ice sheets due to the relatively thick ice at water-terminating margins contributing to higher conduit roof stability. I also suggest that the gradual change from an esker enlargement to a channel and vice versa does not fit the conduit collapse model. Stoker et al. (2021) propose a model for esker enlargement deposition based on their studies on the Evishanoran Esker system in Northern Ireland. In their study, Stoker et al. (2021) conclude that deposition of the esker enlargement took place as a time-transgressive formation of an outwash fan delta during ice margin retreat into a lacustrine environment.

A complex esker system of similar morphometry to the one in Hopendjupet has been described from Breiðamerkurjökull in Iceland (Storrar et al., 2015, 2020). Storrar et al. (2015) claim that ridge divergence is unlikely to occur under high hydraulic pressure conditions, because subglacial channels under high hydraulic pressure tend to capture drainage rather than distribute it (Röthlisberger, 1972), and they conclude that the distributary ridge pattern is the result of drainage entering ice-walled supra-glacial channels under atmospheric pressure which is not conceivable in a marine-terminating ice sheet. It is further implied that the distributary nature is the result of conduit blockage forcing meltwater to find new pathways. Dewald et al. (2021) discuss eskers of similar distributary morphology including features that exhibit a re-convergence. The model proposed for the formation of complex eskers in Dewald et al. (2021) is the same as the conduit collapse model mentioned for esker enlargements but with the addition that flow is diverted around collapsed blocks of ice. As with the esker enlargements, the model is unlikely in marine-terminating ice sheets due to the relatively thick ice at the margins and corresponding high conduit roof stability. Furthermore, the model also fails to explain the abrupt switch between esker deposition in the diverging part of the complex esker system to channel incision in the converging

part.

The results in this study are in line with a depositional model similar to that by Stoker et al. (2021), where esker deposition occurs at the ice margin when subglacial water exits the drainage conduit and enters the ocean. At the ice margin, the capacity of the meltwater to carry sediments is greatly reduced by flow dispersion and sediments are deposited radially from the mouth of the tunnel. The narrowing of the esker enlargement towards the north is consistent with an increase in the spacing of retreat ridges, suggesting that meltwater and/or sediment flux remained relatively constant while the ice sheet retreated at an increasing rate (Figure 5.2).

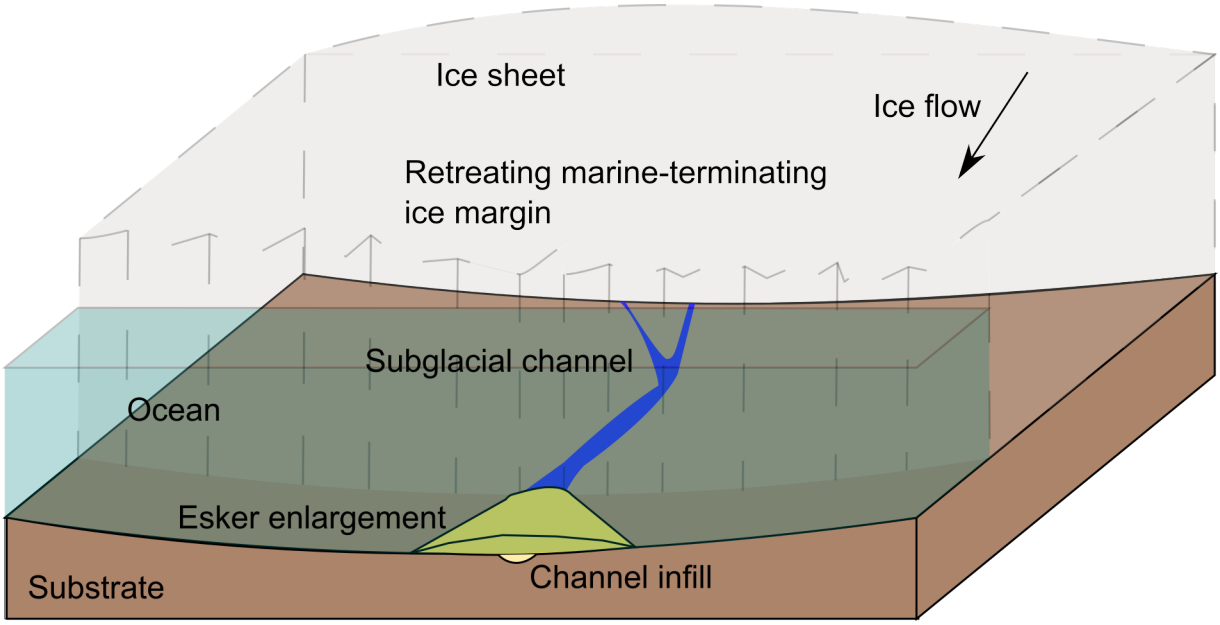

Figure 5.2: Conceptual model for the formation of an esker enlargement. Sediments are deposited at the mouth of a subglacial tunnel as meltwater enters a standing body of water.

As the existing models (Dewald et al., 2021; Storrar et al., 2020) for complex esker deposition do not fully apply to the system described in this study, I propose an alternative depositional model. Hydrofracturing caused by high hydraulic pressure results in flow diverting out of the main drainage conduit into the crevasse network. Over time, flow concentrates into a few channels and abandons the crevasses. Sediment transport is halted in the crevasse network, allowing only sediment-poor water to reach the ice margin (Figure 5.3). Once the margin retreats beyond the crevasse network, deltaic deposition of esker enlargements is resumed. Assuming that prominent parallel linear ridges in the vicinity of the complex esker system are quasi-annual retreat ridges, an estimation of the duration of formation for the complex esker system can be made. The retreat ridges occur at a spacing of 300 (± 100) meters and the start of the divergence to the end of the converge covers a distance of approximately 5300 meters. As such, the complex esker system was formed over 18 (± 6) years.

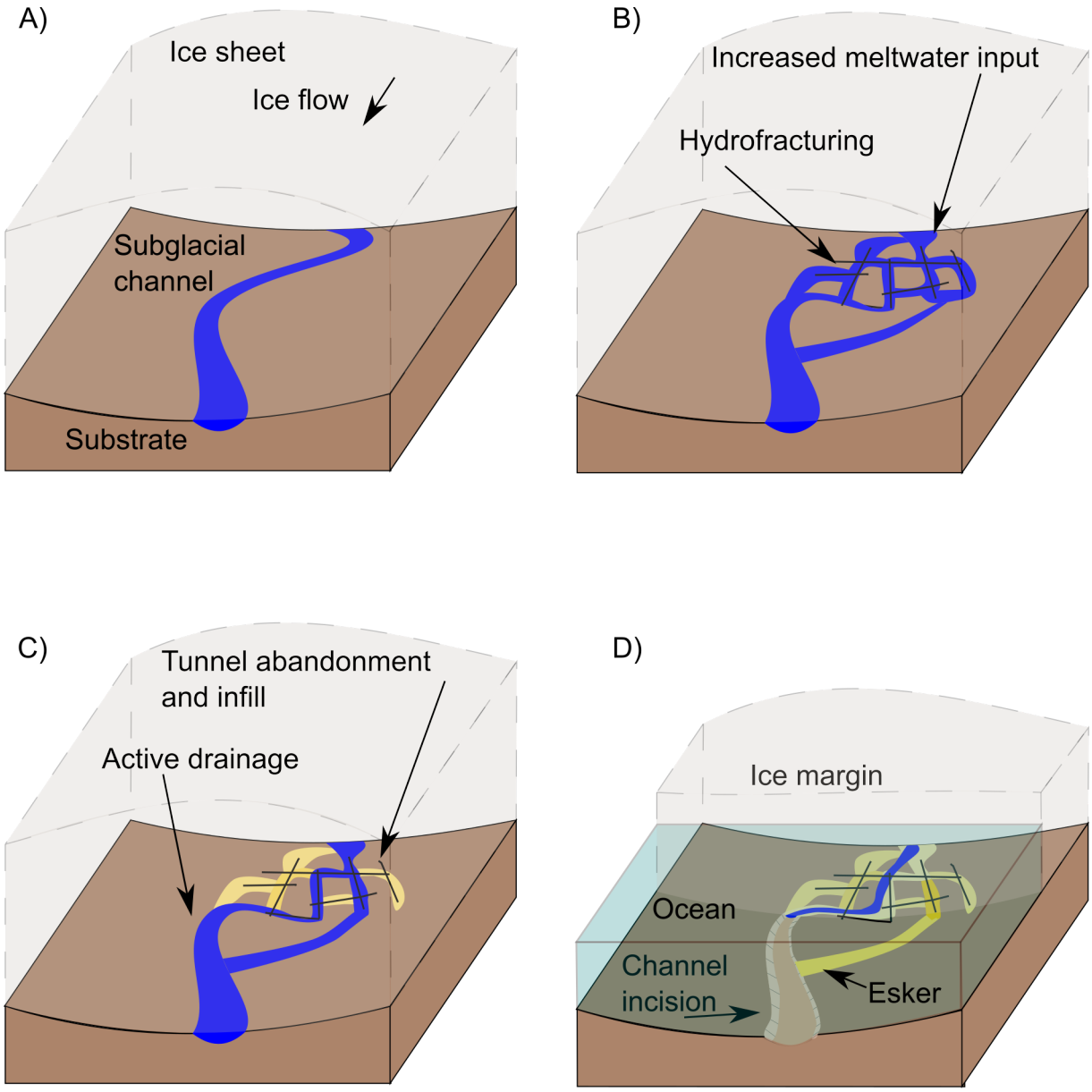

Figure 5.3: Conceptual model for the deposition of the complex esker in Hopendjupet. A) Prior to the deposition of a complex esker, subglacial drainage is confined to a single erosional channel. B) Increased hydraulic pressure causes hydrofracturing of the ice surrounding the meltwater channel, fractures and crevasses are immediately filled with water. C) Gradually, flow concentrates into a few channels, thus abandoning fractures and crevasses and leaving esker sediment deposits. D) The end product. A distributed network of eskers in abandoned channels and deltaic deposition at the mouth of an active channel.

5.3 Hopendjupet ERS

The relatively narrow (30 to 60 meters) but continuous (over 18 kilometers) ERS consists of single-sharp-crested low relief (up to 7.2 meters) eskers. The ERS are fully distributed inside of an erosional channel and, other than the roughly 5-kilometer long channel section immediately following the Central Channel Anabranch. As such, the ERS is interpreted as an esker corridor as described by Cummings et al. (2011).

The esker corridor occurs on the slope break of a topographic high, Sentralbanken. to the east, migrating down the slope from the north towards the south. Superposition of the esker within the erosional channel indicates a time-transgressive formation of a Nye-channel to an R-channel. If the esker formed time-transgressively near the ice margin as the ice sheet retreated, the relatively uniform morphology of the esker corridor can only be explained by steady retreat over a distance of at least 18 kilometers with constant meltwater discharge and sediment flux. This seems unlikely for at least three reasons: 1. The width of the esker is less than the meltwater channel, meaning that the accommodation space for esker deposition was less than the width of the erosive discharge. If esker deposition took place near the margin, the meltwater conduit would exhibit widening, due to lowering ice overburden pressure toward the margin (Röthlisberger, 1972), and thus an increase in accommodation space for esker deposition resulting in an esker that at least covers the width of the channel and potentially exceeds it. 2. The sinuosity of the conduit increases toward the south. A straight subglacial tunnel is expected in a system dominated by ice overburden pressure and the sinuosity is expected to increase toward the margin as the ice sheet thins and the effect of ice overburden pressure decreases (Storrar et al., 2014). Thus, the meltwater channel would meander near the ice margin as is noted in sections of the tunnel valley hosting both the esker enlargement and the esker bead system. 3. Assuming an ice margin retreat rate of 1600 meters per year (upper limit as per Shackleton et al. (2023) and this study), the meltwater and sediment fluxes would need to remain stable for at least 11 years, which even at a time-scale of one year seems problematic due to seasonal fluxes in meltwater discharge (Hewitt, 2013). For the above reasons, the most probable scenario would be a synchronous formation of the esker ridge along the length of the erosional corridor. Numerical modelling of the drainage pathways shows that drainage in this area is conceivable for a range of floatation factors, although, more so in higher pressure systems (Figure 4.38).

Esker corridors have previously been described in Cummings et al. (2011) where they are said to be formed in either short conduits or long conduits depending on the size of the ablation zone and the relief of the ice surface. In a short conduit system, the ablation zone is narrow and the ice surface has a steep profile relative to a long conduit system. A short

conduit system is characterised by sequences of short esker corridors that terminate in fan-shaped segments that form time-transgressively. The long conduit system is composed of a single or dendritic continuous conduit that may end in a fan-shaped segment (Cummings et al., 2011). Eskers found in combinations of Nye- and R-channels are common in Poland (e.g., Frydrych, 2021, 2022) but less so in Fennoscandia and Canada (Frydrych, 2021). High continuity in eskers has been attributed to deposition in supraglacial or open-crevasse settings (Perkins et al., 2016), while that may be the case, Frydrych (2022) notes that esker deposition in Nye- and R-channels may appear similar to esker deposited under atmospheric pressure.

I suggest a depositional model in which the channel offshoot that formed the ERS was relatively short-lived. Formation of the esker corridor is initiated by a phase of high discharge carving out a Nye-channel (Figure 5.4, A). The Nye-channel formation was potentially predated by a sheet flow flooding event which carved out the suspected glacial curvilineations (Lesemann et al., 2010), although this hypothesis warrants further investigation. After an initial high discharge and high hydraulic pressure phase, the discharge gradually decreased with an accompanying drop in hydraulic pressure. The tunnel geometry responded to the lower hydraulic pressure by closing and switching to an ice-incising R-channel. During the waning discharge, the erosive capabilities of the flow decreased until sediments fell out of suspension, building up an esker (Figure 5.4, B). The esker deposition occurred synchronously along the entire length of the system. The proposed depositional model was derived independently of but is in accordance with a model termed the "variable pressure model of corridor formation" (Sharpe et al., 2021). Observations on meltwater corridor widths (0.05 to 3.3 kilometers) made by Lewington et al. (2020) are similar to those observed in the Eastern Channel Branch (0.05 to 1 kilometer), which are said to represent a single maximum flow event (Lewington et al., 2020).

5.4 Hoburgs Bank GSRN

Ridges and mounds on Hoburgs Bank are interpreted as a GSRN, as described in Evans et al. (2022), where geometric ridges branch out from a sinuous ridge. The morphology of the GSRN is highly complex and without further sedimentological studies interpretations of their formation can not be confirmed. For any further discussion on the Hoburgs Bank, it is assumed that a sedimentological study supports the hypothesis of crevasse, hydrofracture, or tunnel infill as the mode of formation for all features comprising the GSRN.

The closest analog to the Hoburgs Bank GSRN in literature can be found in multiple publications on Hørbyebreen, Svalbard (Evans et al., 2012, 2022; Ewertowski et al., 2019;

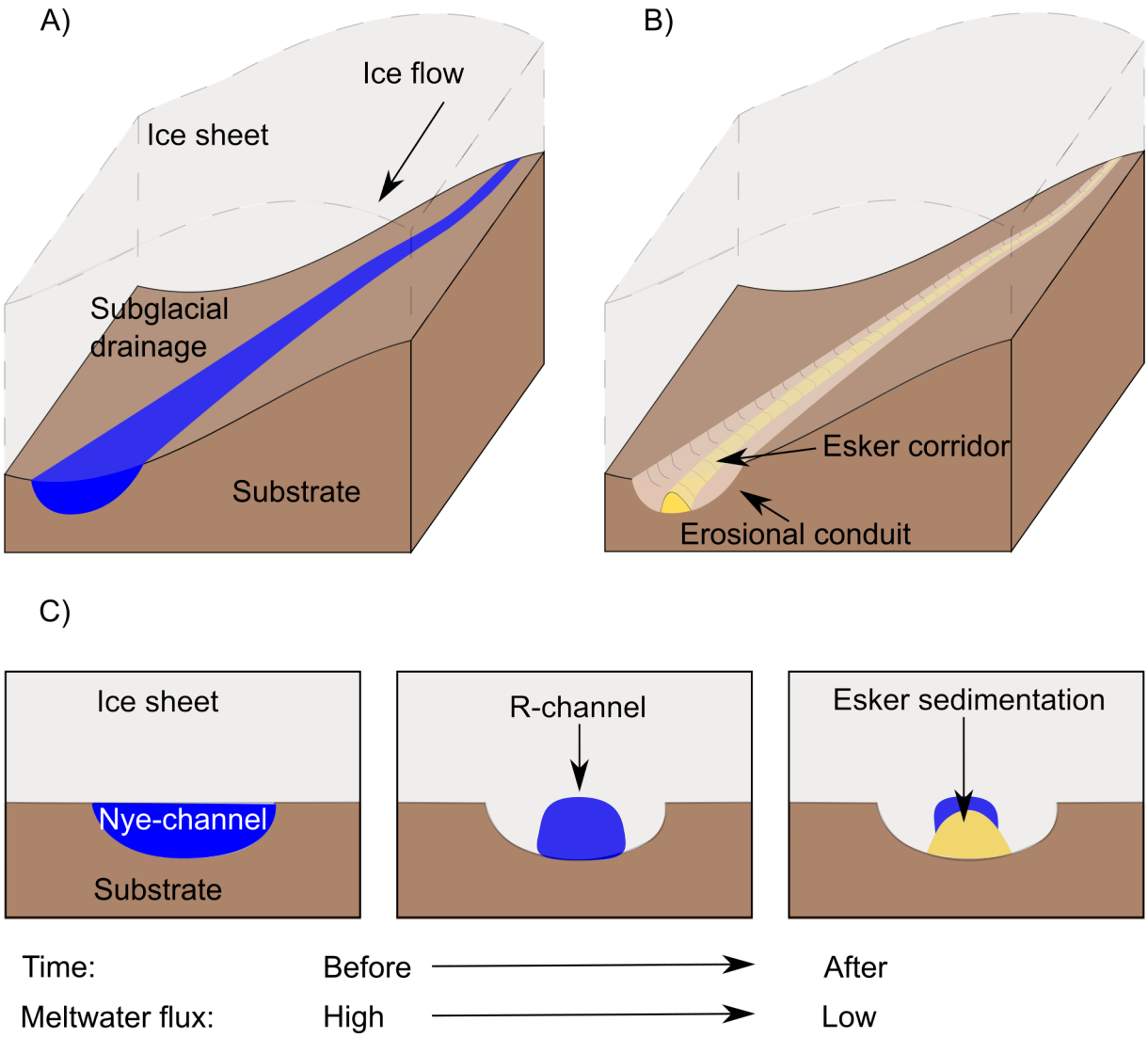

Figure 5.4: Conceptual model of the deposition of the esker corridor in Hopendjupet. A: Initial phase of high meltwater discharge, formation of an erosional channel. B: The drainage pathway has been abandoned, leaving a continuous esker ridge deposited fully subglacially. C: Change from a channel incising into the substrate (Nye-channel) to an R-channel due to a decrease in the erosive capacity of the drainage pathway. As the meltwater flux decreases, the width of the drainage conduit decreases as ice overburden pressure overcomes the hydraulic pressure in the conduit. Waining water discharge leads to a decrease in sediment carrying capacity and thus an esker is formed.

Storrar et al., 2020). The studies on the Hørbyebreen GSRN were conducted at an actively retreating margin. The morphology of the Hørbyebreen GSRN is not discussed in detail in any of the four studies mentioned above. Evans et al. (2022) note that the length of individual landforms comprising the GSRN is between 19 and 34 meters (values vary by year of measurement) which is considerably shorter than the average of 68 meters found in the Hoburgs Bank GSRN, although it should be noted that their mapping was performed on higher resolution topographic and photometric data (Ewertowski et al., 2019), allowing for a higher inclusion of smaller features. Many of the smaller ridges and mounds on Hoburgs Bank were ignored in this study, especially if the features were isolated from other landforms. Storrar et al. (2020) classified eskers in the Hørbyebreen foreland as having a sharp-crested cross-section. Storrar et al. (2020) further note that larger ridges in the Hørbyebreen foreland have relief of up to 10 meters and a width of 15 meters. While this deviates significantly from observations of ridge height and width on Hoburgs Bank, cross-sections shown in Storrar et al. (2020) for three ridges in Hørbyebreen show a height of 2, 4, and 12 meters with widths of 10, 15, and over 50 meters respectively (roughly estimated from Figure 14 in Storrar et al. (2020)). This would give ridges in the Hørbyebreen foreland a width vs. height ratio of between 3 and 5 which is still only half as much as calculated values for Hoburgs Bank ridges and mounds. It should be mentioned that eskers in the Hørbyebreen foreland contain ice cores and they will lower as the ice melts (Price, 1969). All aforementioned studies agree that the GSRN in Hørbyebreen represents sediment infill of supra-, en- and subglacial tunnels and crevasses. The formation of tunnels and crevasses was related to elevated hydraulic pressures potentially induced by surging or jökulhlaup events. Ewertowski et al. (2019) goes as far as to say that the Hørbyebreen GSRN indicates rapid release of pressurised meltwater from temperate to cold-based parts of the glacier snout. A study on the thermal regime of Hørbyebreen found that the glacier is polythermal and contains a 40-meter thick temperate layer beneath 100 to 130 meters of cold ice (Małecki et al., 2013).

Strong topographic control on GSRN distribution is suggested by the observation that 90% of all mapped features occupy the shallowest 15 meters of the study area. The collapsed crest morphology of both ridges and mounds surrounding the interpreted alignment is best explained by the theory of an ice-core melt-out introduced in Subsection 4.2.6. The high fragmentation of GSRN is likely the result of a cut-and-closure mechanism of englacial conduits (Gulley et al., 2009). The distribution of meltwater channels coupled with the results of numerical modelling (Section 3.6) is indicative of a change between a low basal water pressure system and a high basal water pressure system. During periods of low basal water pressure (Figure 4.37, B), meltwater drains subglacially through the deepest channel section (Figure 4.23) towards the south into the widest part of the channel where it deviates to the southwest. During periods of high basal water pressure ($F > 1.0$), drainage

is distributed across the bank (Figure 4.37, E). The meltwater channel correlating to lower basal water pressures is both deeper and the extent is clearer, indicating that it represents the "steady state" of the drainage system (Figure 5.5,). The complete lack of any noticeable connectivity between the GSRN and the erosional meltwater channels suggests that the source of the meltwater originated from two separate melt systems (Figure 5.5, B). In more persistent conduits or on topographic highs, the englacial incision reached the base of the ice (Figure 5.5, C). Results of numerical modelling and the hypothesis that the GSRN consists of sediments filling not only subglacial channels but en- and supraglacial channels suggest that the source of meltwater was supraglacial. Erosion of the tunnel valley into the substrate is a clear indicator of subglacial drainage and therefore meltwater is to a large degree sourced from basal melting of the ice sheet.

Applying the interpretations of the Hørbyebreen GSRN to the Hoburgs Bank GSRN helps clarify the complex nature of the palaeo-drainage system. A till esker (tunnel infill) genesis of sinuous ridges explains why they do not significantly differ in size and morphology from cross-cutting crevasse-infill ridges. Rapid release of pressurised meltwater from temperate to cold-based parts of the ice margin might explain the distribution of the Hoburgs Bank GSRN in the shallowest parts of the study area. The shallow distribution of the Hoburgs Bank GSRN could be limited by the thermal condition at the base of a polythermal ice sheet. In that case, tunnel and crevasse infill would be driven by freeze and thaw at a fluctuating basal thermal transition, fluctuations that could be induced by hydraulic pressure changes (Fowler et al., 2001).

5.5 Comparison of palaeo-drainage systems in Hopendjupet and on Hoburgs Bank

Between the two study areas, Hopendjupet and Hoburgs Bank, eskers are found to represent a variety of hydraulic drainage regimes in rapidly retreating ice streams. Although nearly all types of eskers are found in this study, there is a notable lack of long, dendritic eskers (Brennand, 2000) commonly described on the former bed of the Laurentide Ice Sheet (e.g., Storrar et al., 2014). Long, dendritic eskers are said to form in extensive R-channels draining meltwater through regionally stagnant ice (Brennand, 2000) (note that by regionally stagnant ice Brennand (2000) is referring to a relatively flat ice surface). The more common expression of meltwater drainage in the two study areas is that of erosional channels where esker deposition occurs at the ice margin where the flow enters a standing body of water (deltaic deposition). The exception to this is the esker conduit in Hopendjupet which likely became inactive subglacially. The GSRN on Hoburgs Bank does not exhibit deltaic esker

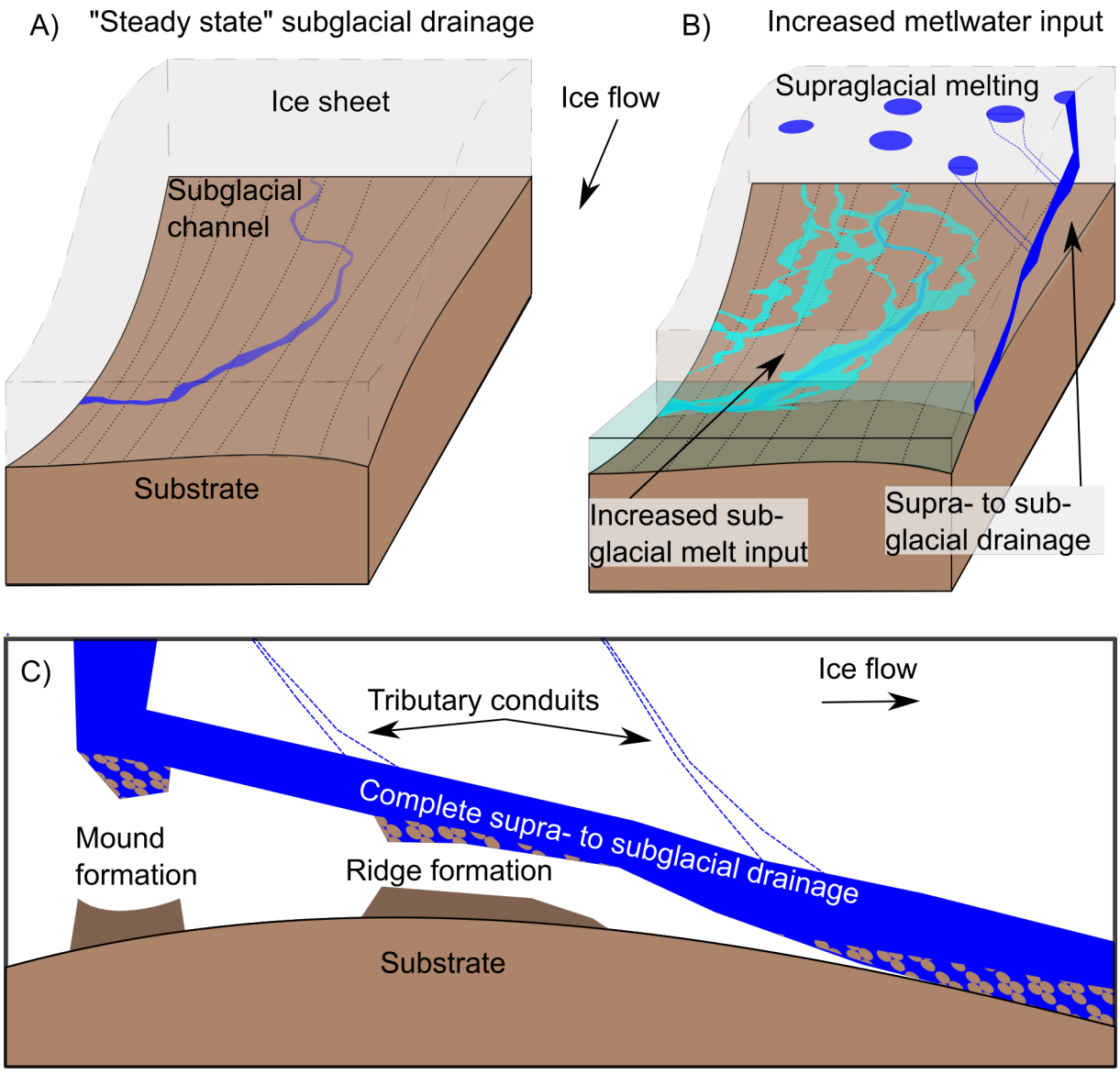

Figure 5.5: Conceptual model of meltwater drainage in Hoburgs Bank. A) "Steady state" primarily subglacial drainage. B) Increased meltwater input into the subglacial system and increased supraglacial melting. C) Hypothetical drainage of supraglacial meltwater into the subglacial system, a part of the sediments are deposited englacially.

deposition or outwash fan deposits, which suggests that either, the tunnel valley system was inactive during the final deglaciation of Hoburgs Bank or the meltwater drainage system was sediment deprived at the margin.

Deltaic esker deposition occurred at the mouth of subglacial tunnels entering a standing body of water where meltwater discharge was high enough to prevent subglacial sediment deposition (Stoker et al., 2021). Two esker systems, mapped in this study, are of deltaic origin, the esker enlargement and the beaded esker system, both in Hopendjupet. The complex esker system in Hopendjupet represents both deltaic and non-deltaic (subglacial) deposition, i.e. deposition started subglacially and continued in place during the retreat of the ice margin until the area became deglaciated. There is an argument to be made that the deposition of the complex esker system is correlated to the deposition of the esker conduit as the potential outwash fan, south of the esker corridor, is roughly on a line parallel to the main orientation of retreat ridges. Both the complex esker system and the esker corridor exhibit characteristics indicative of high hydraulic pressures. The nature of the potential correlation will not be determined here as it would require a more detailed study. Deposition in the ice-marginal zone (non-deltaic deposition) of the ice sheet is observed in the two remaining esker systems, the esker conduit in Hopendjupet and the GSRN on Hoburgs Bank.

Calculated height vs. width ratios show a correlation between the Hopendjupet esker bead system and ridges in the Hoburgs Bank GSRN, with both systems exhibiting a best linear fit of a width roughly 10 times that of the height. Other esker types are even wider compared to their height. The esker corridor is about 17 times wider than it is high. A complete analysis of width and height was not conducted for the complex esker system due to its complex morphology but rough estimates of individual eskers in the system resulted in a width 30 times that of the height. The esker enlargement was measured to be 125 times wider than it was high. Literature on height and width relation of eskers is scarce. Eskers in the complex esker system of Breiðamerkurjökull are roughly 6 times wider than they are high (Storrar et al., 2015). Similarly, observations of tunnel valleys in Kirkham et al. (2024) show that tunnel valleys are generally between 5 and 10 times wider than they are deep. Observations made in this study estimate tunnel valleys as much shallower features, in the region of more than 30 times wider than they are deep. Even the steepest part of the tunnel valley on Hoburgs Bank is 17 times wider than it is deep. This disparity could be explained by sediment filling of the tunnel valley. Well-preserved iceberg scours in Hopendjupet suggest that post-glacial sediments are thin in Hopendjupet (an estimation is not included as it is deemed too unreliable). Kågesten et al. (2020) estimate post-glacial sediment thickness on Hoburgs Bank to be as much as 7.8 meters on the southwestern flank of the bank but generally close to no deposition on elevated topography (Figure 43(A) in

Kågesten et al., 2020).

Both tunnel valley systems exhibit anabranching behavior and their size and scale are of similar magnitude. In contrast to Hoburgs Bank, eskers in Hopendjupet occur within or overprinting erosional channels. The lack of eskers in the tunnel valley system of Hoburgs Bank is consistent with the theory that esker deposition is favoured in low hydraulic pressure gradients (Shreve, 1972), as the whole study area is elevated thus resulting in large hydraulic pressure gradients toward the surrounding troughs. Figure 5.6 combines the models from previous sections and shows that eskers formed from subglacial drainage preferentially occur in, or at the slope break of, a trough. Shreve's theorem further explains the diminishing volume of esker beads upstream, noted in Shackleton et al. (2023), as the Hopendjupet esker bead system progresses upslope.

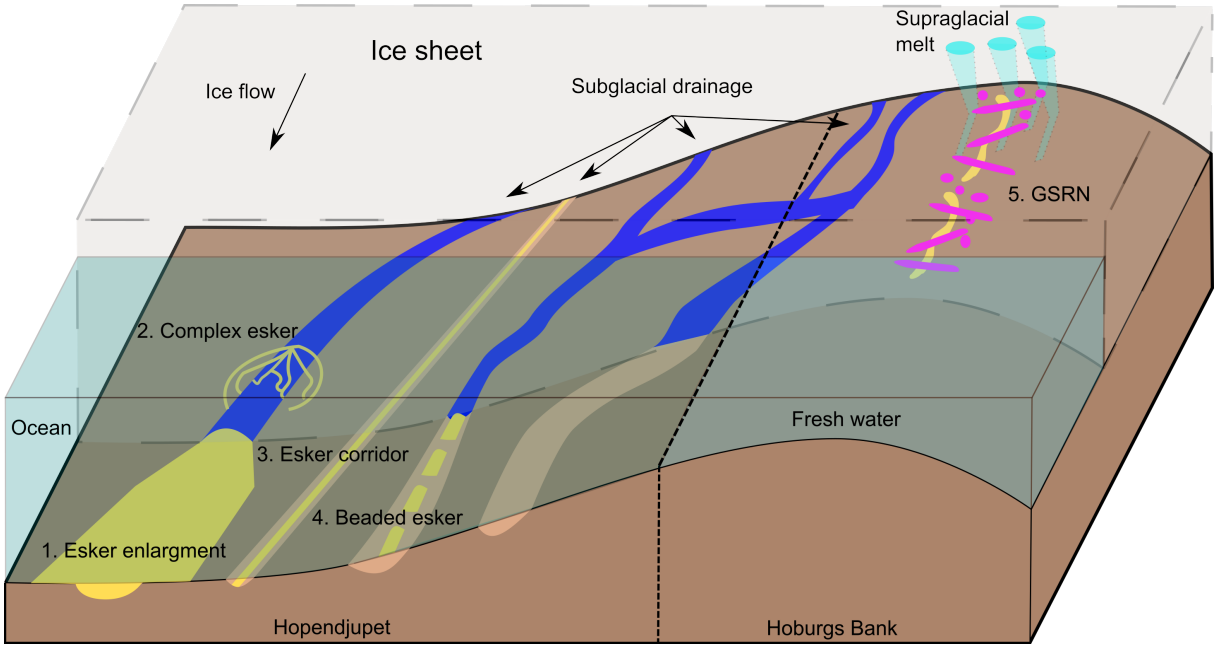

Figure 5.6: A composite of all esker depositional models presented in this study.

6

Conclusion

Two esker systems, one in Hopendjupet and the other on Hoburgs Bank, formed during the deglaciation of the EISC in water-terminating margins were studied based on their morphological character and distribution. Until recently, eskers had rarely been described on former margins of marine-based ice sheets, a fact that is attributed to unfavourable formation in such settings. This study finds that eskers can form at the margin of water-terminating ice sheets. The morphological expression of eskers described in this study is not limited to one esker type but rather exhibits nearly all configurations that have been noted of eskers in other settings. Below is an itemized summary of insights gained from each esker type.

- An esker bead system, assumed to have formed quasi-annually, recorded an overall slowing retreat of the ice margin as the system migrated into shallower water depths on the flanks of Sentralbanken.

- An esker enlargement in Hopendjupet formed as deltaic deposits at the mouth of subglacial erosional tunnels. The esker enlargement represents time-transgressive formation at a retreating ice margin. Meltwater and sediment fluxes were relatively high.

- A complex esker system in the same drainage system as the esker enlargement in Hopendjupet started forming subglacially under high hydraulic pressures. The deposition was time-transgressive but "in-place", meaning that the location of sedimentation did not significantly change during the retreat of the ice margin. Meltwater flux was high but exceeded the discharge capacity of the drainage tunnel, ultimately leading to hydrofracturing.

- An esker conduit formed subglacially and synchronously in Hopendjupet on the slope break of Sentralbanken following a phase of high meltwater discharge and potential

sheet flow.

- A GSRN formed on Hoburgs Bank as supraglacial melt percolated into the cold-based part of a polythermal ice margin. Sediments were squeezed into basal crevasses and short-lived subglacial tunnels.

Further incorporation of sedimentological and subsurface studies should help to clarify the precise nature of esker sedimentation in the two areas. The distribution of sediment grain sizes of the esker enlargement in Hopendjupet can be used to quantify meltwater fluxes through the drainage system. Sub-bottom profiling of eskers and tunnel valleys is needed to assess the true cross-sectional size of the drainage pathways in Hopendjupet. To fill in the knowledge gap regarding the beaded esker system and the esker corridor in Hopendjupet, gaps in the HMSB need to be mapped focusing on the extremities of the landforms.

Bibliography

Andrews, L. C., Catania, G. A., Hoffman, M. J., Gulley, J. D., Lüthi, M. P., Ryser, C., Hawley, R. L., & Neumann, T. A. (2014). Direct observations of evolving subglacial drainage beneath the Greenland Ice Sheet. *Nature*, *514*(7520), 80–83. https://doi.org/10.1038/nature13796

Bamber, J. L., Vaughan, D. G., & Joughin, I. (2000). Widespread Complex Flow in the Interior of the Antarctic Ice Sheet. *Science*, *287*(5456), 1248–1250. https://doi.org/10.1126/science.287.5456.1248

Banerjee, I., & McDonald, B. C. (1975). Nature of Esker Sedimentation. In A. V. Jopling & B. C. McDonald (Eds.), *Glaciofluvial and Glaciolacustrine Sedimentation* (pp. 132–154, Vol. 23). SEPM Society for Sedimentary Geology.

Bennett, M. R., Hambrey, M. J., Huddart, D., & Ghienne, J. F. (1996). The formation of a geometrical ridge network by the surge-type glacier Kongsvegen, Svalbard. *Journal of Quaternary Science*, *11*(6), 437–449. https://doi.org/10.1002/(SICI)1099-1417(199611/12)11:6<437::AID-JQS269>3.0.CO;2-J

Brendryen, J., Haflidason, H., Yokoyama, Y., Haaga, K. A., & Hannisdal, B. (2020). Eurasian Ice Sheet collapse was a major source of Meltwater Pulse 1A 14,600 years ago. *Nature Geoscience*, *13*(5), 363–368. https://doi.org/10.1038/s41561-020-0567-4

Brennand, T. A. (2000). Deglacial meltwater drainage and glaciodynamics: Inferences from Laurentide eskers, Canada. *Geomorphology*, *32*(3), 263–293. https://doi.org/10.1016/S0169-555X(99)00100-2

Christoffersen, P., Piotrowski, J. A., & Larsen, N. K. (2005). Basal processes beneath an Arctic glacier and their geomorphic imprint after a surge, Elisebreen, Svalbard. *Quaternary Research*, *64*(2), 125–137. https://doi.org/10.1016/j.yqres.2005.05.009

Clark, C. D., Evans, D. J. A., Khatwa, A., Bradwell, T., Jordan, C. J., Marsh, S. H., Mitchell, W. A., & Bateman, M. D. (2004). Map and GIS database of glacial landforms and features related to the last British Ice Sheet. *Boreas*, *33*(4), 359–375. https://doi.org/10.1111/j.1502-3885.2004.tb01246.x

Clark, C. D., & Livingstone, S. J. (2018). Glacial curvilineations found along the southern sector of the Laurentide Ice sheet and a hypothesis of formation involving subglacial slope failure in tunnel valleys and subglacial lakes. *Earth Surface Processes and Landforms*, *43*(7), 1518–1528. https://doi.org/10.1002/esp.4324

Close, R. M. H. (1867). Notes on the General Glaciation of Ireland. In *Journal of the Royal Geological Society of Ireland, Vol. I* (pp. 207–246).

Constable, A. J., Harper, S., Dawson, J., Holsman, K., Mustonen, T., Piepenburg, D., & Rost, B. (2022). Cross-Chapter Paper 6: Polar Regions [H.-O. Pörtner, D.C. Roberts, M. Tignor, E.S. Poloczanska, K. Mintenbeck, A. Alegría, M. Craig, S. Langsdorf, S. Löschke, V. Möller, A. Okem, B. Rama (eds.)]. In *Climate Change 2022 – Impacts, Adaptation and Vulnerability: Working Group II Contribution to the Sixth Assessment*

Report of the Intergovernmental Panel on Climate Change (pp. 2319–2368). Cambrigde University Press.

Cummings, D. I., Kjarsgaard, B. A., Russell, H. A. J., & Sharpe, D. R. (2011). Eskers as mineral exploration tools. *Earth-Science Reviews*, *109*(1), 32–43. https://doi.org/10.1016/j.earscirev.2011.08.001

Depoorter, M. A., Bamber, J. L., Griggs, J. A., Lenaerts, J. T. M., Ligtenberg, S. R. M., van den Broeke, M. R., & Moholdt, G. (2013). Calving fluxes and basal melt rates of Antarctic ice shelves. *Nature*, *502*(7469), 89–92. https://doi.org/10.1038/nature12567

Dewald, N., Lewington, E. L. M., Livingstone, S. J., Clark, C. D., & Storrar, R. D. (2021). Distribution, characteristics and formation of esker enlargements. *Geomorphology*, *392*, 107919. https://doi.org/10.1016/j.geomorph.2021.107919

Evans, D. J. A., Ewertowski, M., Roberts, D. H., & Tomczyk, A. M. (2022). The historical emergence of a geometric and sinuous ridge network at the Hørbyebreen polythermal glacier snout, Svalbard and its use in the interpretation of ancient glacial landforms. *Geomorphology*, *406*. https://doi.org/10.1016/j.geomorph.2022.108213

Evans, D. J. A., Nelson, C. D., & Webb, C. (2010). An assessment of fluting and "till esker" formation on the foreland of Sandfellsjökull, Iceland. *Geomorphology*, *114*(3), 453–465. https://doi.org/10.1016/j.geomorph.2009.08.016

Evans, D. J. A., Storrar, R. D., & Rea, B. R. (2016). Crevasse-squeeze ridge corridors: Diagnostic features of late-stage palaeo-ice stream activity. *Geomorphology*, *258*, 40–50. https://doi.org/10.1016/j.geomorph.2016.01.017

Evans, D. J. A., Strzelecki, M., Milledge, D. G., & Orton, C. (2012). Hørbyebreen polythermal glacial landsystem, Svalbard. *Journal of Maps*.

Ewertowski, M. W., Evans, D. J. A., Roberts, D. H., Tomczyk, A. M., Ewertowski, W., & Pleksot, K. (2019). Quantification of historical landscape change on the foreland of a receding polythermal glacier, Hørbyebreen, Svalbard. *Geomorphology*, *325*, 40–54. https://doi.org/10.1016/j.geomorph.2018.09.027

Fowler, A. C., Murray, T., & Ng, F. S. L. (2001). Thermally controlled glacier surging. *Journal of Glaciology*, *47*(159), 527–538. https://doi.org/10.3189/172756501781831792

Frydrych, M. (2021). Complex genesis of N-channel eskers illustrated with the example of an esker near Tosie (east-central Poland). *Acta Universitatis Lodziensis. Folia Geographica Physica*, *20*(20), 13–25.

Frydrych, M. (2022). Classification of esker morphology on soft beds in the area of the Saalian and Elsterian Glaciations in Poland. *Acta Geographica Lodziensia*, *112*, 45–60. https://doi.org/10.26485/AGL/2022/112/4

GEBCO Compilation Group. (2023). GEBCO 2023 Grid. https://doi.org/10.1016/j.quascirev.2023.108136

Germain, S. L. S., & Moorman, B. J. (2019). Long-term observations of supraglacial streams on an Arctic glacier. *Journal of Glaciology*, *65*(254), 900–911. https://doi.org/10.1017/jog.2019.60

Gowan, E. J., Zhang, X., Khosravi, S., Rovere, A., Stocchi, P., Hughes, A. L. C., Gyllencreutz, R., Mangerud, J., Svendsen, J.-I., & Lohmann, G. (2021). A new global ice sheet reconstruction for the past 80 000 years. *Nature Communications*, *12*(1), 1199. https://doi.org/10.1038/s41467-021-21469-w

Greenwood, S. L., Avery, R. S., Gyllencreutz, R., Regnéll, C., & Tylmann, K. (2024). Footprint of the Baltic Ice Stream: Geomorphic evidence for shifting ice stream pathways. *Boreas*, *53*(1), 4–26. https://doi.org/10.1111/bor.12634

Greenwood, S. L., Clason, C. C., Helanow, C., & Margold, M. (2016). Theoretical, contemporary observational and palaeo-perspectives on ice sheet hydrology: Processes and products. *Earth-Science Reviews*, *155*, 10–14. https://doi.org/10.1016/j.earscirev.2016.01.010

Gulley, J. D., Benn, D. I., Müller, D., & Luckman, A. (2009). A cut-and-closure origin for englacial conduits in uncrevassed regions of polythermal glaciers. *Journal of Glaciology*, *55*(189), 66–80. https://doi.org/10.3189/002214309788608930

Hans van der Kwast. (2021, October). Complete Updated Workflow Stream and Catchment Delineation in QGIS. Retrieved March 2, 2024, from https://www.youtube.com/watch?v=C3AMh3sZzJQ

Hättestrand, C., & Clark, C. D. (2006). The glacial geomorphology of Kola Peninsula and adjacent areas in the Murmansk Region, Russia. *Journal of Maps*, *2*(1), 30–42. https://doi.org/10.4113/jom.2006.41

Hewitt, I. J. (2013). Seasonal changes in ice sheet motion due to melt water lubrication. *Earth and Planetary Science Letters*, *371-372*, 16–25. https://doi.org/10.1016/j.epsl.2013.04.022

Hooke, R. L. (1984). On the Role of Mechanical Energy in Maintaining Subglacial Water Conduits at Atmospheric Pressure. *Journal of Glaciology*, *30*(105), 180–187. https://doi.org/10.3189/S0022143000005918

Jakobsson, M., Mayer, L. A., Bringensparr, C., Castro, C. F., Mohammad, R., Johnson, P., Ketter, T., Accettella, D., Amblas, D., An, L., Arndt, J. E., Canals, M., Casamor, J. L., Chauché, N., Coakley, B., Danielson, S., Demarte, M., Dickson, M.-L., Dorschel, B., . . . Zinglersen, K. B. (2020). The International Bathymetric Chart of the Arctic Ocean Version 4.0. *Scientific Data*, *7*(1), 176. https://doi.org/10.1038/s41597-020-0520-9

Kågesten, G., Baumgartner, F., & Freire, F. (2020). *High-resolution benthic habitat mapping of Hoburgs bank, Baltic Sea* (tech. rep. No. SGU-rapport 2020:34). SGU Geological Survey of Sweden. Uppsala, Sweden.

Karssenberg, D., Schmitz, O., Salamon, P., de Jong, K., & Bierkens, M. F. P. (2010). A software framework for construction of process-based stochastic spatio-temporal models and data assimilation. *Environmental Modelling & Software*, *25*(4), 489–502. https://doi.org/10.1016/j.envsoft.2009.10.004

Kirkham, J. D., Hogan, K. A., Larter, R. D., Arnold, N. S., Ely, J. C., Clark, C. D., Self, E., Games, K., Huuse, M., Stewart, M. A., Ottesen, D., & Dowdeswell, J. A. (2024). Tunnel valley formation beneath deglaciating mid-latitude ice sheets: Observations and modelling. *Quaternary Science Reviews*, *323*, 107680. https://doi.org/10.1016/j.quascirev.2022.107680

Lesemann, J.-E., Piotrowski, J. A., & Wysota, W. (2010). "Glacial curvilineations": New glacial landforms produced by longitudinal vortices in subglacial meltwater flows. *Geomorphology*, *120*(3), 153–161. https://doi.org/10.1016/j.geomorph.2010.03.020

Lewington, E. L. M., Livingstone, S. J., Clark, C. D., Sole, A. J., & Storrar, R. D. (2020). A model for interaction between conduits and surrounding hydraulically connected distributed drainage based on geomorphological evidence from Keewatin, Canada. *The Cryosphere*, *14*(9), 2949–2976. https://doi.org/10.5194/tc-14-2949-2020

Lindström, E. (1993). Esker Enlargements in Northern Sweden. *Geografiska Annaler. Series A, Physical Geography*, *75*(3), 95–110. https://doi.org/10.2307/521028

Livingstone, S. J., Lewington, E. L. M., Clark, C. D., Storrar, R. D., Sole, A. J., Mcmartin, I., Dewald, N., & Ng, F. (2020). A quasi-annual record of time-transgressive esker

formation: Implications for ice-sheet reconstruction and subglacial hydrology. *The Cryosphere*, *14*(6), 1989–2004. https://doi.org/10.5194/tc-14-1989-2020

Lurton, X. (2002). *An Introduction to Underwater Acoustics: Principles and Applications*. Springer Science & Business Media.

Mäkinen, J. (2003). Time-transgressive deposits of repeated depositional sequences within interlobate glaciofluvial (esker) sediments in Köyliö, SW Finland. *Sedimentology*, *50*(2), 327–360. https://doi.org/10.1046/j.1365-3091.2003.00557.x

Małecki, J., Faucherre, S., & Strzelecki, M. (2013). Post surge geometry and thermal structure of Hørbyebreen, central Spitsbergen.

Ogniewicz, R. L., & Ilg, M. (1992). Voronoi skeletons: Theory and applications. *92*, 63–69.

Patton, H., Hubbard, A., Andreassen, K., Auriac, A., Whitehouse, P. L., Stroeven, A. P., Shackleton, C., Winsborrow, M., Heyman, J., & Hall, A. M. (2017). Deglaciation of the Eurasian ice sheet complex. *Quaternary Science Reviews*, *169*, 148–172. https://doi.org/10.1016/j.quascirev.2017.05.019

Patton, H., Hubbard, A., Andreassen, K., Winsborrow, M., & Stroeven, A. P. (2016). The build-up, configuration, and dynamical sensitivity of the Eurasian ice-sheet complex to Late Weichselian climatic and oceanic forcing. *Quaternary Science Reviews*, *153*, 97–121. https://doi.org/10.1016/j.quascirev.2016.10.009

Patton, H., Mattingsdal, R., Pavel, S., Cooke, F. A., & Alexandropoulou, N. (2020). CAGE20-2 Cruise Report: Hunting flares in Hopendjupet and glacigenic sediments in Sentralbankrenna. *CAGE – Centre for Arctic Gas Hydrate, Environment and Climate Report Series*, *8*. https://doi.org/10.7557/cage.6745

Perkins, A. J., Brennand, T. A., & Burke, M. J. (2016). Towards a morphogenetic classification of eskers: Implications for modelling ice sheet hydrology. *Quaternary Science Reviews*, *134*, 19–38. https://doi.org/10.1016/j.quascirev.2015.12.015

Pitcher, L. H., & Smith, L. C. (2019). Supraglacial Streams and Rivers. *Annual Review of Earth and Planetary Sciences*, *47*, 421–452. https://doi.org/10.1146/annurev-earth-053018-060212

Price, R. J. (1969). Moraines, Sandar, Kames and Eskers near Breidamerkurjökull, Iceland. *Transactions of the Institute of British Geographers*, (46), 17–43. https://doi.org/10.2307/621406

Röthlisberger, H. (1972). Water Pressure in Intra- and Subglacial Channels. *Journal of Glaciology*, *11*(62), 177–203. https://doi.org/10.3189/S0022143000022188

Sandwell, D., Gille, S., & Smith, W. (Eds.). (2002, June). *Bathymetry from Space: Oceanography, Geophysics, and Climate* (tech. rep.). Geoscience Professional Services. Bethesda, Maryland. www.igpp.ucsd.edu/bathymetry_workshop

Schoof, C. (2007). Ice sheet grounding line dynamics: Steady states, stability, and hysteresis. *Journal of Geophysical Research: Earth Surface*, *112*(F3). https://doi.org/10.1029/2006JF000664

Serov, P., Patton, H., Mazzini, A., Mattingsdal, R., Shephard, G., Cooke, F. A., Aguiar, V. C. M. d., Holm, V. D., Alessandrini, G., Cala, J. C. M., & Luerssen, P. (2022). CAGE22-6 cruise report: GEO-3144/8144 Teaching Cruise: Geologically controlled hydrocarbon seepage in Hopendjupet and the wider Barents Sea. *CAGE – Centre for Arctic Gas Hydrate, Environment and Climate Report Series*, *10*. https://doi.org/10.7557/cage.6769

Shackleton, C., Patton, H., Winsborrow, M., Esteves, M., Bjarnadóttir, L., & Andreassen, K. (2023). Distinct modes of meltwater drainage and landform development beneath

the last Barents Sea ice sheet. *Frontiers in Earth Science*, *11*. Retrieved December 15, 2023, from https://www.frontiersin.org/articles/10.3389/feart.2023.1111396

Sharpe, D., Lesemann, J.-E., Knight, R., & Kjarsgaard, B. (2021). Regional stagnation of the western Keewatin ice sheet and the significance of meltwater corridors and eskers, northern Canada. *Canadian Journal of Earth Sciences*, *58*(10), 1005–1026. https://doi.org/10.1139/cjes-2020-0136

Shepherd, A., Ivins, E., Rignot, E., Smith, B., van den Broeke, M., Velicogna, I., Whitehouse, P., Briggs, K., Joughin, I., Krinner, G., Nowicki, S., Payne, T., Scambos, T., Schlegel, N., A, G., Agosta, C., Ahlstrøm, A., Babonis, G., Barletta, V. R., . . . The IMBIE Team. (2020). Mass balance of the Greenland Ice Sheet from 1992 to 2018. *Nature*, *579*(7798), 233–239. https://doi.org/10.1038/s41586-019-1855-2

Shepherd, A., & Wingham, D. (2007). Recent Sea-Level Contributions of the Antarctic and Greenland Ice Sheets. *Science*, *315*(5818), 1529–1532. https://doi.org/10.1126/science.1136776

Shreve, R. L. (1972). Movement of Water in Glaciers. *Journal of Glaciology*, *11*(62), 205–214. https://doi.org/10.3189/S002214300002219X

Stoker, B. J., Livingstone, S. J., Barr, I. D., Ruffell, A., Storrar, R. D., & Roberson, S. (2021). Variations in esker morphology and internal architecture record time-transgressive deposition during ice margin retreat in Northern Ireland. *Proceedings of the Geologists' Association*, *132*(4), 409–425. https://doi.org/10.1016/j.pgeola.2021.03.002

Storrar, R. D., Evans, D. J. A., Stokes, C. R., & Ewertowski, M. (2015). Controls on the location, morphology and evolution of complex esker systems at decadal timescales, Breiðamerkurjökull, southeast Iceland. *Earth Surface Processes and Landforms*, *40*(11), 1421–1438. https://doi.org/10.1002/esp.3725

Storrar, R. D., Ewertowski, M., Tomczyk, A. M., Barr, I. D., Livingstone, S. J., Ruffell, A., Stoker, B. J., & Evans, D. J. A. (2020). Equifinality and preservation potential of complex eskers. *Boreas*, *49*(1), 211–231. https://doi.org/10.1111/bor.12414

Storrar, R. D., Stokes, C. R., & Evans, D. J. A. (2014). Morphometry and pattern of a large sample (>20,000) of Canadian eskers and implications for subglacial drainage beneath ice sheets. *Quaternary Science Reviews*, *105*, 1–25. https://doi.org/10.1016/j.quascirev.2014.09.013

Swithinbank, C. W. M. (1954). "Ice streams". *Polar Record*, *7*(48), 185–186. https://doi.org/10.1017/S0032247400043746

Uścinowicz, S., Zachowicz, J., & Sokołowski, K. (2003). The southern baltic relative sea level changes, glacio-isostatic rebound and shoreline displacement. *Polish Geological Institute Special Papers*, *10*, 1–79.

Vatne, G., & Irvine-Fynn, T. D. L. (2016). Morphological dynamics of an englacial channel. *Hydrology and Earth System Sciences*, *20*(7), 2947–2964. https://doi.org/10.5194/hess-20-2947-2016

Weertman, J. (1972). General theory of water flow at the base of a glacier or ice sheet. *Reviews of Geophysics*, *10*(1), 287–333. https://doi.org/10.1029/RG010i001p00287

Winsborrow, M., Andreassen, K., Corner, G. D., & Laberg, J. S. (2010). Deglaciation of a marine-based ice sheet: Late Weichselian palaeo-ice dynamics and retreat in the southern Barents Sea reconstructed from onshore and offshore glacial geomorphology. *Quaternary Science Reviews*, *29*(3), 424–442. https://doi.org/10.1016/j.quascirev.2009.10.001

Winsborrow, M., & Knies, J. (2021). CAGE21-6 Cruise Report: Hydrocarbon leakage in Hopendjupet, central Barents Sea. *CAGE – Centre for Arctic Gas Hydrate, Environment and Climate Report Series*, *9*. https://doi.org/10.7557/cage.6675

Winsborrow, M., Patton, H., Jakobsen, F., Pau, M., Akinselure, A., & Jensen, A. (2021). CAGE21-4 Cruise Report: Oil slicks, gas flares and glacial landforms in Hopendjupet and Sentralbanken. *CAGE – Centre for Arctic Gas Hydrate, Environment and Climate Report Series*, *9*. https://doi.org/10.7557/cage.6703

Zwally, H. J., Abdalati, W., Herring, T., Larson, K., Saba, J., & Steffen, K. (2002). Surface Melt-Induced Acceleration of Greenland Ice-Sheet Flow. *Science*, *297*(5579), 218–222. https://doi.org/10.1126/science.1072708